Molecular and Spin Dynamics in Solid State Nuclear Magnetic Resonance Spectroscopy

by

Douglas C. Maus

B.A., Chemistry and Mathematics (1991)

Washington University

Submitted to the Department of Chemistry
in Partial Fulfillment of the Requirements for the Degree of
Doctor of Philosophy in Physical Chemistry

at the

Massachusetts Institute of Technology

September 1996

Signature of Author .....
Department of Chemistry
August 2, 1996

Certified by .....
Robert G Griffin
Professor of Chemistry
Thesis Supervisor

Accepted by .....
Dietmar Seyferth
Professor of Chemistry
Chairman, Departmental Committee on Graduate Students

This Doctoral thesis has been examined by a Committee of the Department of Chemistry as follows:

Professor James R. Williamson.....
Chairman

Professor Robert G. Griffin.....
Thesis Supervisor

Professor Richard R. Schrock .....

Molecular and Spin Dynamics in Solid State
Nuclear Magnetic Resonance Spectroscopy

by

Douglas C Maus

Submitted to the Department of Chemistry
on August 7, 1996 in Partial Fulfillment of the Requirements
for the Degree of Doctor of Philosophy
in Physical Chemistry

ABSTRACT

Nuclear Magnetic Resonance (NMR) spectroscopic data often involve spatial and spin dynamics and interference phenomena between the two. Experimental results are presented which demonstrate several of these phenomena and exploitation of these anomalies to acquire and improve knowledge regarding relevant chemistry. In some cases numerical analysis of such data are illustrated for obtaining quantitative rates of molecular dynamics.

First, the dynamics of methyls bonded to the metals Tungsten and Tantalum are examined. In the case of Tungsten, an interference between methyl dynamics and proton decoupling is studied, whereas in the Tantalum instance, interference between molecular dynamics and Magic Angle Spinning (MAS) is examined. Agostic interactions had been hypothesized to exist in both compounds, but the unusual molecular dynamics are explainable without invoking a relation to such interactions. Further, no evidence is found to support the existence agostic bonds from examination of X-ray crystal data.

Next, the spin dynamics in high resolution solid state proton systems diluted by deuterium is examined. In this case techniques such as Rotational Resonance and Radio-Frequency driven Dipolar Recoupling (RFDR) are employed to counteract the averaging of dipole couplings induced by MAS. The numerical analysis of such data in systems in which internuclear distances of interest are not identical but rather statistically distributed is discussed.

Finally, a technique which may improve the sensitivity of NMR experiments is demonstrated. Dynamic Nuclear Polarization (DNP) is adapted to solid state MAS experiments and shown to enhance the signal intensity of a biomolecule, T4-lysozyme, by a factor of ~50. The necessary conditions for application of this technique to solid state NMR is discussed.

Thesis Supervisor: Robert G Griffin

Title: Professor of Chemistry

Table of Contents

Acknowledgments

I am indebted to many people for assistance during my graduate studies. I would like to thank first, my advisor, Professor Robert Griffin, for his direction and guidance, without which my work may well have been quite rudderless. I thank also my many coworkers in the Griffin research group, especially: Boqin Sun for guidance and generous permission to use programs of his design, Janet Griffiths for collaboration in the Tungsten projects, Joanna Long for experimental ^{2}H advice, Ling Zheng and Andrew Bennett for collaboration on the ^{1}H work, Dennis Hall, Souheil Inati, Gary Gerfen, and Lino Becerra for tutelage in the DNP work, and Ajay Thakkar, Peter Allen, and Jeff Bryant for much appreciated technical assistance.

I would like to thank Professor Richard Schrock for his kind assistance and patience in the organometallic work as well as the members of his research group: Andreas Grohmann, Shifang Luo, Scott Seidel, and William Davis.

I am also indebted to David Ruben for invaluable advice in computer matters.

1. Introduction to Solid State Magnetic Resonance

1.1 Classical Principles

Torque and Angular Momentum

An understanding of the basis of Magnetic Resonance Spectroscopy relies upon the principles of torque and angular momentum. A simple example illustrating some of the classical basics of torque and angular momentum is the pendulum.[1]

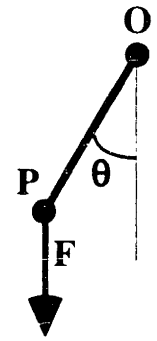

Consider a pendulum, assumed to have mass m, displaced from origin $\mathbf{O}$ by fixed length $r = \overline{\mathbf{OP}}$. Gravity then directly exerts a force $\mathbf{F}$ and consequently a torque $\boldsymbol{\tau} = \mathbf{R} \times \mathbf{F}$ where

$$\mathbf{R} = -r\sin(\theta)\hat{\mathbf{x}} - r\cos(\theta)\hat{\mathbf{y}}$$

and

$$\mathbf{F} = -mg\hat{\mathbf{y}}$$

thus,

$$\boldsymbol{\tau} = mgr\sin(\theta)\hat{\mathbf{z}}$$

The torque equals the time derivative of the spatial angular momentum:

$$\boldsymbol{\tau} = \frac{d\mathbf{L}}{dt}$$

where $\mathbf{L} = \mathbf{R} \times \mathbf{P}$ and the momentum, $\mathbf{P} = m\frac{d\mathbf{R}}{dt}$.

The spatial angular momentum in this instance follows

$$\mathbf{L} = -mr^2\frac{d\theta}{dt}\hat{\mathbf{z}}$$

Substituting the result for the torque and differentiating the angular momentum with respect to time results in

$$mgr\sin(\theta)\hat{\mathbf{z}} = -mr^2\frac{d^2\theta}{dt^2}\hat{\mathbf{z}}$$

$$-\frac{g}{r}\sin(\theta) = \frac{d^2\theta}{dt^2}$$

If the angular displacements are small, the sine term may be approximated by the angle. This leads to a simple solution, namely

$$\theta(t) = \theta|_{t=0}\cos\left(\sqrt{\frac{g}{r}}t\right) + \dot{\theta}|_{t=0}\left(\sqrt{\frac{r}{g}}\right)\sin\left(\sqrt{\frac{g}{r}}t\right)$$

In the absence of friction the pendulum swings back and forth with period $2\pi\sqrt{\frac{r}{g}}$.

Next consider an object possessing an intrinsic angular momentum, as in a gyroscope or a spinning top, with angular momentum axis parallel to $\mathbf{R}$ and of magnitude s.

$$\frac{d\mathbf{L}}{dt} = \boldsymbol{\tau}$$

$$\frac{d}{dt}(s\mathbf{R} + \mathbf{R}\times\mathbf{P}) = \mathbf{R}\times\mathbf{F}$$

If the problem is simplified by considering only the $s\mathbf{R}$ term in the time derivative of the angular momentum, then

$$s\frac{d\mathbf{R}}{dt} = \mathbf{R}\times\mathbf{F}$$

that is, at any instant the direction of change in $\mathbf{R}$ is perpendicular to its current direction as well as the direction of gravity. This results in a motion commonly known as precession, in which there is rotation about both an internal axis (the director $\mathbf{R}$) as well as rotation about the axis of the applied force, in this case the gravitational field which lies along the $\hat{\mathbf{y}}$ axis.

Spins and Magnetic Fields

The classical treatment of nuclei or electrons possessing both intrinsic spin angular momentum and magnetic dipole moments in a strong magnetic field is completely analogous to that described above for a gyroscope. The magnetic field $\mathbf{B}$ is to the

magnetic dipole moment $\boldsymbol{\mu}$ as the field of gravity is to the mass. That is, the magnetic field exerts a torque:

$$\boldsymbol{\tau} = \boldsymbol{\mu} \times \mathbf{B}$$

Were there no intrinsic spin angular momentum (or were it not collinear with the magnetic dipole moment) then the magnetic moment would swing like a pendulum. Since the spin angular momentum $\mathbf{J}$ is collinear with the magnetic dipole with proportionality γ, the gyromagnetic ratio (i.e. $\boldsymbol{\mu} = \gamma\mathbf{J}$), the spins precess, following

$$\frac{d\mathbf{J}}{dt} = \frac{1}{\gamma}\frac{d\boldsymbol{\mu}}{dt} = \boldsymbol{\tau}$$

$$\frac{d\boldsymbol{\mu}}{dt} = \boldsymbol{\mu} \times \gamma\mathbf{B}$$

Again, the direction of change in $\boldsymbol{\mu}$ is perpendicular to its current direction as well as the direction of the magnetic field, thus resulting in precession of the magnetic/spin moment about the axis of the magnetic field.

The Rotating Frame

A convenient frame of reference for consideration of such precessional motion is the rotating frame.[2] Consider a change of axes such that

$$\begin{pmatrix} \hat{\mathbf{i}} \\ \hat{\mathbf{j}} \\ \hat{\mathbf{k}} \end{pmatrix} = \begin{pmatrix} \cos(\omega t) & \sin(\omega t) & 0 \\ -\sin(\omega t) & \cos(\omega t) & 0 \\ 0 & 0 & 1 \end{pmatrix} \begin{pmatrix} \hat{\mathbf{x}} \\ \hat{\mathbf{y}} \\ \hat{\mathbf{z}} \end{pmatrix}$$

The $\begin{pmatrix} \hat{\mathbf{i}} & \hat{\mathbf{j}} & \hat{\mathbf{k}} \end{pmatrix}$ represent a rotating reference frame around the $\hat{\mathbf{z}}$ axis with angular frequency ω(rad/s). Letting $\Omega \equiv \omega\hat{\mathbf{z}}$ represent this frame, then

$$\frac{d\hat{\mathbf{i}}}{dt} = -\omega\sin(\omega t)\hat{\mathbf{x}} + \omega\cos(\omega t)\hat{\mathbf{y}}$$

$$= \omega\hat{\mathbf{j}} = \omega(\hat{\mathbf{k}} \times \hat{\mathbf{i}})$$

$$= \Omega \times \hat{\mathbf{i}}$$

likewise

$$\frac{d\hat{\mathbf{j}}}{dt} = \Omega \times \hat{\mathbf{j}}$$

$$\frac{d\hat{\mathbf{k}}}{dt} = \Omega \times \hat{\mathbf{k}}$$

Then expressing the magnetic moment in this frame

$$\boldsymbol{\mu} = \mu_i \hat{\mathbf{i}} + \mu_j \hat{\mathbf{j}} + \mu_k \hat{\mathbf{k}}$$

$$\frac{d\boldsymbol{\mu}}{dt} = \frac{d\mu_i}{dt}\hat{\mathbf{i}} + \frac{d\mu_j}{dt}\hat{\mathbf{j}} + \frac{d\mu_k}{dt}\hat{\mathbf{k}} + \mu_i \frac{d\hat{\mathbf{i}}}{dt} + \mu_j \frac{d\hat{\mathbf{j}}}{dt} + \mu_k \frac{d\hat{\mathbf{k}}}{dt}$$

$$\frac{d\boldsymbol{\mu}}{dt} = \frac{\partial \boldsymbol{\mu}}{\partial t} + \Omega \times \boldsymbol{\mu} = \boldsymbol{\mu} \times (\gamma \mathbf{B})$$

$$\frac{\partial \boldsymbol{\mu}}{\partial t} = \boldsymbol{\mu} \times (\gamma \mathbf{B} + \Omega)$$

That is, the motion of the magnetic moment in the rotating frame follows the same form as in the static Cartesian frame, except that the magnetic field must be replaced by an effective field which is the sum of the Cartesian field and the rotating frame. If we choose a rotating frame $\Omega = -\gamma \mathbf{B}$, then the time derivative of the magnetic moment in this rotating frame is zero - the magnetic moment is stationary in this frame of reference. Viewed in the static, or lab, frame the magnetic moment precesses about the $\hat{\mathbf{z}} = \hat{\mathbf{k}}$ with frequency $-\gamma \mathbf{B}$, known as the Larmor frequency. An applied magnetic field oscillating at the same frequency would drive this precession into resonance, a classical interpretation of continuous wave (CW) magnetic resonance, whereas the net magnetic moment of a collection of spins beginning in the transverse plane would precess and thus create an electromotive force(voltage) oscillating at the Larmor Frequency in a transverse inductor, the classical interpretation of pulsed/Fourier Transform magnetic resonance.

1.2 Quantum Principles

A quantum mechanical treatment of spins with magnetic dipole moments begins from the perspective of energy rather than torque.[3] The energy, represented by the Hamiltonian, of a magnetic dipole moment in a strong magnetic field is

$$H = -\boldsymbol{\mu} \bullet \mathbf{B}$$

Since $\boldsymbol{\mu} = \gamma \mathbf{J}$, where $\mathbf{J}$ represents the intrinsic spin angular momentum (which is a purely quantum mechanical feature of atomic particles[4]),

$$H = -\gamma \mathbf{J} \bullet \mathbf{B}$$

In quantum theory, $\mathbf{J}$ is treated as a vector operator representing spin angular momentum. $\mathbf{J}$ operates on the quantum eigen states as

$$\mathbf{J}^2 |\psi\rangle = J(J+1)\hbar^2 |\psi\rangle$$

$$\mathbf{J}_z |\psi\rangle = m\hbar |\psi\rangle$$

where J is either integral or half-integral and m is one of the $2J+1$ values $J, J-1, \ldots -J$. In a strong uniaxial field $\mathbf{B} = B\hat{\mathbf{z}}$, so

$$H = -\gamma B \mathbf{J}_z$$

(where $\mathbf{J}_z$ is still emphasized to signify its quantum mechanical operator nature). This interaction is called the Zeeman interaction. The diagram shown below illustrates the energy levels for a J=1/2 spin in a magnetic field.

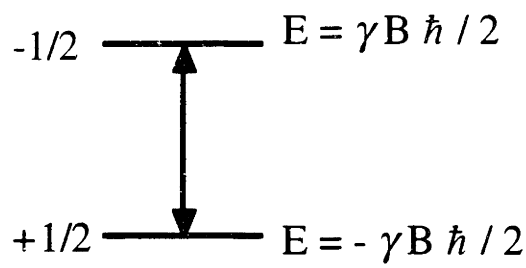

The difference in energy between the spin states is $\Delta E = \gamma B \hbar$ so spins may be induced to switch states by absorption of emission of quanta possessing this energy, namely

$$\hbar\omega = \gamma B \hbar$$

That is, quantum magnetic resonance requires application of electromagnetic radiation of frequency $\omega = \gamma B$. Thus, the classical observational interpretation flows seamlessly into the quantum mechanical.

1.3 Internal Fields

The frequency of precession of spins and their magnetic moments is predominantly due to the strong magnetic field, but fine structure in solid state magnetic resonance spectra can result from many effects[5, 6]. In nuclei, examples include differences in electronic shielding (the chemical shift), the magnetic field produced by nearby spins and their magnetic moments (the dipole coupling), and the interaction of electric quadrupole moments with electric field gradients (quadrupole coupling).

1.3.1 Chemical Shift

Empirically, nuclei experience small shifts from the Larmor frequency that depend linearly on the strength of the applied magnetic field. The magnetic field induces electronic currents and consequently small magnetic fields which shield nuclei from the large field, more or less strongly depending on the electronic density near that nucleus. This interaction is direction dependent, or anisotropic, and while unapparent in rapidly reorienting solutes, is very important in the solid state. The chemical shift anisotropy is represented as a second rank tensor, such that the anisotropic chemical shift interaction in the rotating frame is

$$H_{CSA} = -\gamma \mathbf{J} \bullet (\boldsymbol{\sigma} \bullet \mathbf{B})$$

where $\boldsymbol{\sigma}$ is the chemical shift tensor and $(\boldsymbol{\sigma} \bullet \mathbf{B})$ represents the anisotropic and field dependent electronic shielding contribution to the effective magnetic field which interacts with the magnetic moment $\gamma \mathbf{J}$. In the high field limit,

$$H_{CSA} = -\gamma B(\sigma_{xx} \sin^2\theta \cos^2\phi + \sigma_{yy} \sin^2\theta \sin^2\phi + \sigma_{zz} \cos^2\theta)\mathbf{J}_z$$

where $\sigma_{xx}, \sigma_{yy}, \sigma_{zz}$ are the diagonal values of the tensor in its principal axis system and θ, ϕ are the polar angles of the magnetic field in this axis system. In a powder, where the distribution of θ follows $\sin(\theta)$, the anisotropic chemical shift lineshape follows the shape diagrammed below:

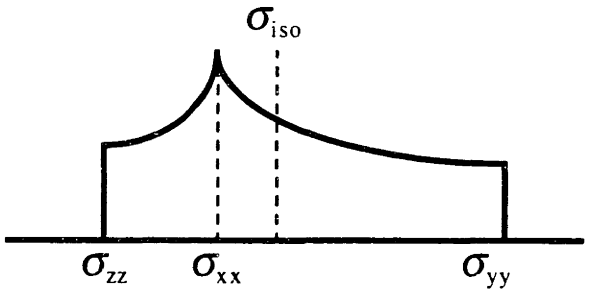

1.3.2 Dipole Coupling

Just as two toy magnets exert a force on each other, so too, do the magnetic dipole moments of spins. In classical terms, the magnetic field at the point $\mathbf{r}$ produced by a magnetic dipole at the origin is[7]

$$\mathbf{B}_{dipole} = \frac{1}{r^3}\left(3(\boldsymbol{\mu} \bullet \mathbf{r}_0)\mathbf{r}_0 - \boldsymbol{\mu}\right)$$

where $\mathbf{r}_0 = \frac{\mathbf{r}}{r}$. Then,

$$H_{dipole} = -\boldsymbol{\mu}_i \bullet \mathbf{B}_{dipole,j} = \frac{\boldsymbol{\mu}_i \bullet \boldsymbol{\mu}_j}{r^3} - \frac{3(\boldsymbol{\mu}_i \bullet \mathbf{r})(\boldsymbol{\mu}_j \bullet \mathbf{r})}{r^5}$$

Substituting $\gamma\mathbf{J}$ for $\boldsymbol{\mu}$, using polar coordinates for $\mathbf{r}$ in the reference frame defined by the magnetic field, and using the high field approximation yields[2]

$$H_{dipole} = -\frac{\gamma_i \gamma_j}{r^3}(3\cos^2\theta - 1)\left[\mathbf{J}_{zi}\mathbf{J}_{zj} - \frac{1}{4}(\mathbf{J}_{+i}\mathbf{J}_{-j} + \mathbf{J}_{-i}\mathbf{J}_{+j})\right]$$

The second term in the bracket, $(\mathbf{J}_{+i}\mathbf{J}_{-j} + \mathbf{J}_{-i}\mathbf{J}_{+j})$, is the so called flip-flop term. While it consists of off-diagonal elements when expressed in matrix mechanics, normally ignored in the high field approximation, it is retained for like-spins where the operation (for which it is aptly named) is energy conserving. In the expression for unlike-spins, for example between different nuclei or between nuclei and electrons, the flip-flop term is ignored as the operation is no longer energy conserving. Using the substitution $b_d = \frac{\gamma_i \gamma_j \hbar^2}{r^3}\frac{(3\cos^2\theta - 1)}{2}$, the energy level diagram of the Zeeman states interacting via the dipole coupling is given below:

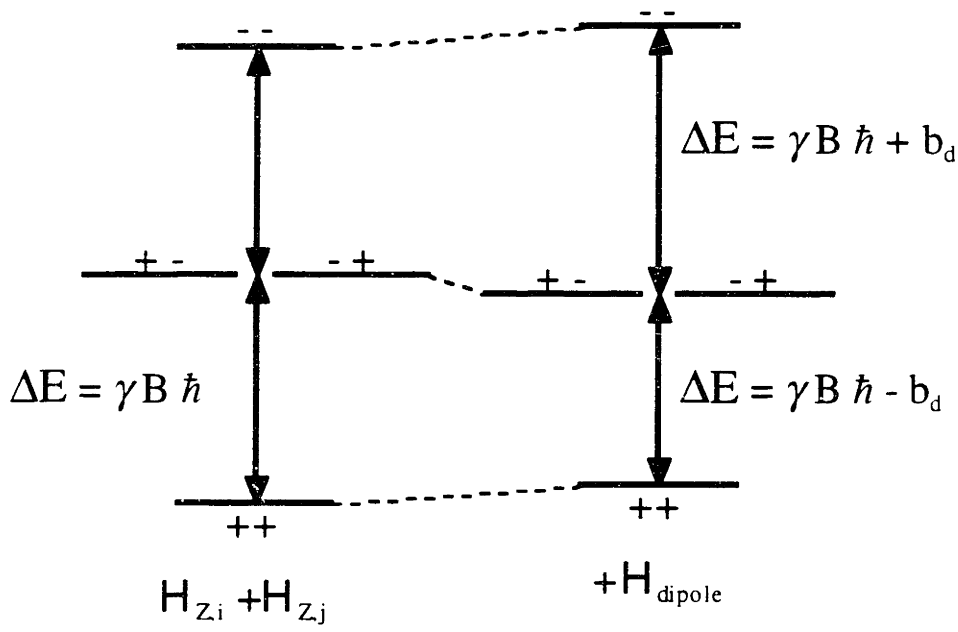

For a powder, the lineshape of two isolated dipole coupled spins (known as a Pake pattern)[8] follows the form diagrammed below:

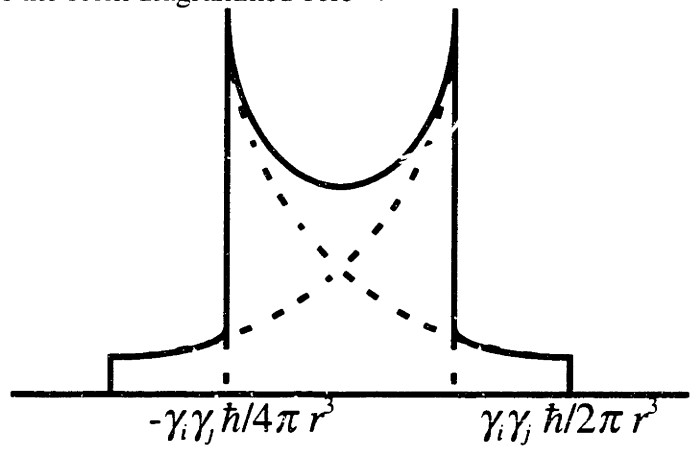

1.3.3 Quadrupole Interaction

The effects of quadrupole moments in magnetic resonance spectra results from the interaction of the nuclear charge distribution $\rho(\mathbf{r})$ with the electronic electric field $V(\mathbf{r})$[2]

$$E = \int d\mathbf{r}\rho(\mathbf{r})V(\mathbf{r})$$

Expanding the potential in a Taylor series

$$V(\mathbf{r}) = V|_{\mathbf{r}=0} + \sum_i x_i \left.\frac{\partial V}{\partial x_i}\right|_{\mathbf{r}=0} + \frac{1}{2}\sum_{ij} x_i x_j \left.\frac{\partial^2 V}{\partial x_i \partial x_j}\right|_{\mathbf{r}=0}$$

$$E = V|_{\mathbf{r}=0}\int d\mathbf{r}\rho(\mathbf{r}) + \sum_i \left.\frac{\partial V}{\partial x_i}\right|_{\mathbf{r}=0}\int d\mathbf{r}x_i\rho(\mathbf{r}) + \frac{1}{2}\sum_{ij}\left.\frac{\partial^2 V}{\partial x_i \partial x_j}\right|_{\mathbf{r}=0}\int d\mathbf{r}x_i x_j\rho(\mathbf{r})$$

The first term represents the interaction of the nuclear charge with the electronic potential at the nucleus. The second term represents the vector dot product of the nuclear electric dipole with the electronic electric field. Since the nuclear states have parity, $\rho(\mathbf{r})$ is either an even or odd function, so the nuclear electric dipole $\int d\mathbf{r}x_i\rho(\mathbf{r})$ is zero, and thus the second term vanishes. The third term represents the scalar contraction of two second rank tensors, the second partial derivative of the electric potential, commonly known as the electric field gradient, $V_{\alpha\alpha}$, and the nuclear electric quadrupole moment, commonly denoted $Q_{\alpha\alpha}$. This quadrupole term can be rewritten as

$$\frac{1}{2}\sum_{ij}\left.\frac{\partial^2 V}{\partial x_i \partial x_j}\right|_{\mathbf{r}=0}\int d\mathbf{r}x_i x_j\rho(\mathbf{r})$$

$$= \frac{1}{6}\sum_{ij} V_{ij}\int d\mathbf{r}\rho(\mathbf{r})(3x_i x_j - \delta_{ij}r^2)$$

The conventional quantum analogy of this analysis proceeds by using quantum position operators $\hat{\mathbf{x}}_i$ in place of the nuclear position variables x_i. The Wigner-Eckart theorem then relates those position operators in the quadrupole moment to the nuclear spin angular momentum operators. The result, including proportionality constants and using irreducible spherical tensor representation, is

$$H_Q = \frac{eQ}{4I(2I-1)}\left[\left(3\mathbf{I}_z^2 - I(I+1)\right)V_0 + (\mathbf{I}_\pm\mathbf{I}_z + \mathbf{I}_z\mathbf{I}_\pm)V_{\pm 1} + \mathbf{I}_\pm^2 V_{\pm 2}\right]$$

(Note that the dipole moment that is related to angular momentum in the Zeeman interaction is magnetic, while the quadrupole moment which is related to angular momentum in the quadrupole interaction is electric.) In the high field truncation, terms involving $\mathbf{I}_\pm$ are ignored, resulting in

$$H_Q = \frac{eQ}{4I(2I-1)}\left[\left(3\mathbf{I}_z^2 - I(I+1)\right)V_0\right]$$

Thus, only nuclei with spin greater that 1/2 exhibit a first order quadrupole effect. The resulting energy level diagram for a spin 1 nucleus, such as a deuteron, is shown below:

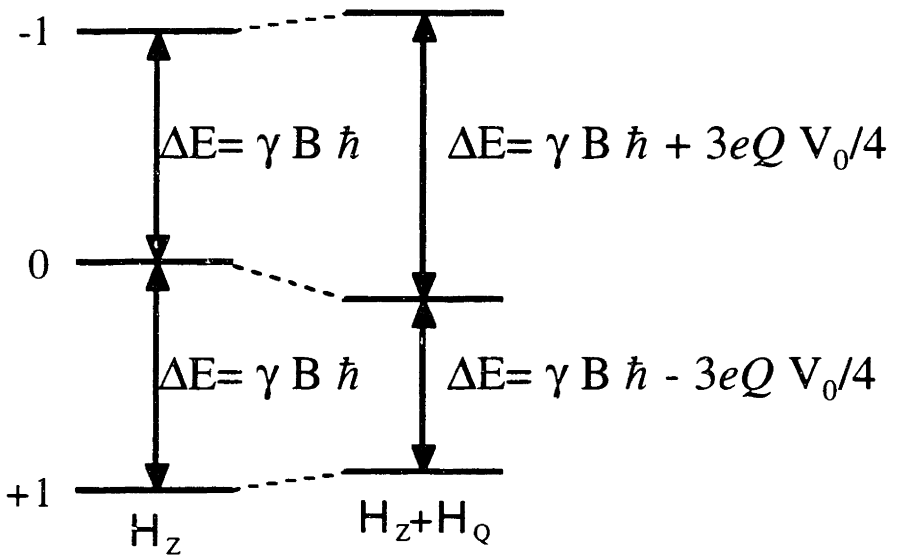

The quadrupole interaction shifts the energy levels such that there are two resonance frequencies, symmetrically displaced above and below the Larmor frequency by the amount $\frac{3eQV_0}{4h}$. For an arbitrary orientation of the molecule and thus the electronic electric field gradient, V_0 is expressed as

$$V_0 = \tfrac{1}{2} V_{zz}\left[(3\cos^2\theta - 1) + \eta \sin^2\theta \cos 2\phi\right]$$

where $\eta = \frac{V_{xx} - V_{yy}}{V_{zz}}$, the $V_{\alpha\alpha}$ are the diagonal tensor elements in the principal axis system, and θ, ϕ are the polar angles of the magnetic field axis in this PAS. For deuterium in organic/alkyl compounds, η is typically near zero. Then for a powder deuterium sample, the observed spectrum is schematically represented below

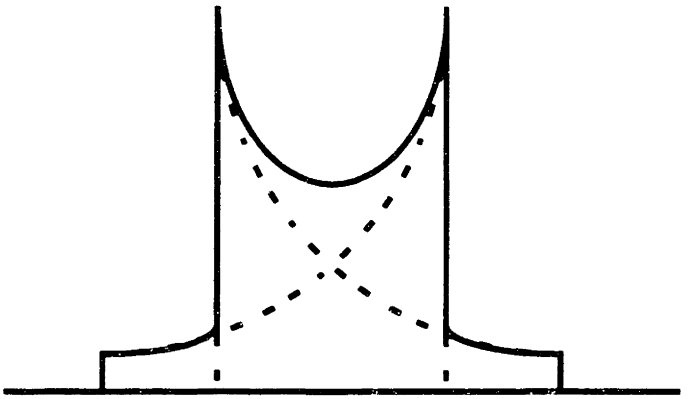

General Characteristics of Internal Fields

The size of these interactions, as described by the amount they contribute to the linewidth in magnetic resonance spectra depends on the types of spins being examined as well as the static field strength. For example, in conventional fields, the isotropic chemical shifts range over ~10 kHz in both ^{1}H and ^{13}C spectra. Between nuclei the dipole coupling amounts to ~2 kHz between bonded ^{13}C, or ~25 kHz between ^{1}H on methyl groups. The dipole coupling between electrons separated by 10Å is on the order of tens of MHz, while the coupling between nuclei and electrons, known as the hyperfine coupling, amounts to several Mhz in the case of ^{1}H. In nuclei, again, the quadrupole interaction dwarfs the chemical shift and dipole coupling, amounting to ~170 kHz in ^{2}H and on the order of MHz in halide nuclei.

All these internal fields as well as others may be represented using a formalism described by Spiess[9]. In this formalism the Hamiltonian for a given interaction, λ, is the sum of contractions of two tensors up to the second rank.

$$H_{\lambda} = C^{\lambda} \sum_{l=0}^{2} \sum_{m=-l}^{l} (-1)^{m} T^{\lambda}_{l,m} R^{\lambda}_{l,-m}$$

One set of tensors, $\boldsymbol{R}$, represents the spatial dependence and the other, $\boldsymbol{T}$, represents the spin operator dependence. This formalism is particularly convenient both for the abstract consideration of separate spatial and spin dynamics, as well calculation of the effects from these dynamics.

1.4 Dynamics

1.4.1 Spatial Dynamics

Spatial motion of magnetically resonant spins can have a dramatic effect on the resonance lineshape. A simple analysis is as follows. Periodic signals may be quite close to each other in frequency. Over a single period then, the signals may nearly overlap and be indistinguishable. Two signals differing in frequency by $\Delta\nu$ become exactly one period out of synchronization with each other (and thus easily distinguishable) at a time $\tau = 1/\Delta\nu$. For spins in different environments, internal fields create different resonant frequencies. If spatial motion exchanges spins in these different environments back and forth on a time scale much faster than τ, then the two different resonant frequencies become blurred and only a single average resonant signal is observed. If the motion is slow compared to τ, then both individual signals are still observed. Molecular motion, as in the atomic hopping of protons on methyl groups or the molecular isotropic reorientation of solutes in solution, can produce drastic averaging of resonant lineshapes, sometimes narrowing the widths of lineshapes ten- or hundred-fold.

Taking such clues from nature provides the basis for the resolution improvement solid state NMR technique known as magic angle spinning. Magic angle spinning represents a coarse method of imitating the isotropic reorientation typical of solutes in solution. The sample is rotated rapidly (1-20 kHz) about an axis angled 54.7° with respect to the magnetic field axis. This "magic" angle is the diagonal of a cube, and in a sense MAS represents a cubic approximation to the perfectly isotropic sphere.

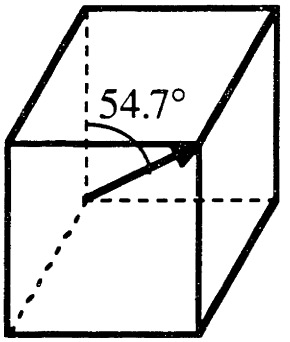

The effect of magic angle spinning, on both lineshape narrowing and internal fields, will be discussed later.

1.4.2 Spin Dynamics

The discussion thus far has covered signals from magnetic spin systems mainly in terms of frequencies. The signal frequencies were described in the quantum interpretation as being directly related to the differences in energy levels between spin states. In fact, observation of magnetic resonance signals entails the concomitant absorption/emission of photons and transitions between quantum states whose energy difference matches that of the photon, thus conserving energy. This evolution, thought of as spins flipping from an up to a down state or vice-versa, is known as spin dynamics. A discussion of spin dynamics must first begin with a description of the spin system in equilibrium.[2] A collection of like spins in thermal equilibrium follows Boltzmann statistics. That is, the number of spins N_E in a state of energy E is proportional to

$$N_E = e^{-E/kT}$$

Then, for a collection of spin 1/2 particles, the ratio of number of spins in the lower energy state compared to the higher energy state is

$$\frac{N_+}{N_-} = e^{\frac{-(E_+ - E_-)}{kT}} = e^{\frac{\gamma B \hbar}{kT}}$$

For the typical field strengths used in today's nuclear magnetic resonance spectrometers, at room temperature this ratio for ^{1}H spins is nearly 1, differing only by some parts per

million. There are nearly as many spins in the higher energy state as the lower. The difference in populations, the polarization (α), is what accounts for the macroscopic observable net magnetic moment, and since it is so small, the much lamented poor sensitivity of NMR experiments. When the populations are perturbed from this thermal equilibrium polarization value, the system relaxes to equilibrium exponentially with a time constant, T_1

$$\alpha(t) = \alpha|_{equil} + \left(\alpha|_{t=0} - \alpha|_{equil}\right)e^{-t/T_1}$$

The process by which the polarization returns to thermal equilibrium, spin-lattice relaxation, is actually driven by spatial dynamics.[9] Molecular motion on time scales, τ near the inverse of the Larmor precession frequency $1/\gamma B$, provides the coupling between the spin system and the other thermal baths (known as the lattice) the brings the spin system to the same temperature as the rest of the material. Another important form of spin-dynamics is that which occurs when two types of spins are strongly coupled and the populations of one of these types is perturbed from equilibrium. If the coupling of the perturbed spin to the lattice is weak compared to than the coupling between the two spins, then the two spin systems may exchange polarization. In effect, this process acts to equalize the temperatures corresponding to the populations of their spin states. The rate at which the two spin polarizations equalize is related to the dipole coupling between the two spins. Measurement of the polarization exchange rate can be used to infer the dipole coupling which may then be used to infer the distance between the two spins in the material. This general idea is the basis for a great many techniques used in magnetic resonance to provide molecular structure information. A third type of spin dynamics involves interaction not between spins and the lattice, nor between two different types of spins, but among spins of the same type. The small number of excess spins which account for the equilibrium polarization of the material are thought of as being uniformly spatially distributed throughout the material. In the situation where the polarization is its equilibrium value but these excess spins are distributed unevenly in the material, couplings between

spins of the same type acts to eliminate these spatial polarization gradients, much as diffusion acts to eliminate spatial concentration gradients of solutes. In fact, this process takes the same nomenclature, being known as spin diffusion. Spin diffusion is boon and bane to magnetic resonance spectroscopist, depending upon the application at hand, as will be discussed later.

References

1. D. Halliday, R. Resnick, *Fundamentals of Physics* (Wiley, 1988).
2. C. P. Slichter, *Principles of Magnetic Resonance*. P. Fulde, Eds., Springer Series in Solid-State Sciences (Springer-Verlag, Heidelberg, 1989), vol. 1.
3. C. Cohen-Tannoudji, B. Diu, F. Laloe, *Quantum Mechanics* (Wiley, 1977).
4. P. A. M. Dirac, *Principles of Quantum Mechanics*. J. Birman, S. F. Edwards, C. H. L. Smith, M. Rees, Eds., The International Series of Monographs on Physics (Clarendon Press, Oxford, 1958), vol. 27.
5. A. Abragam, *Principles of Nuclear Magnetism* (Oxford University Press, Oxford, 1961).
6. M. Munowitz, *Coherence and NMR* (Wiley, 1988).
7. G. Arfken, *Mathematical Methods for Physicists* (Academic Press, Inc., 1985).
8. G. E. Pake, *Journal of Chemical Physics* **16**, 327-336 (1948).
9. H. W. Spiess, in *Dynamic NMR Spectroscopy*(Springer-Verlag, 1978), vol. 15,.

2. Spatial Dynamics

2.1 Molecular Motion

As mentioned previously, molecular motion can have drastic effects in magnetic resonance spectra. One of the best stages for investigating molecular motion is through deuterium Nuclear Magnetic Resonance(NMR) spectroscopy. The method is both simple and powerful. The theoretical and practical analysis is quite straightforward, being uncomplicated by multiple interactions or involved time dependencies (as in Magic Angle Spinning). The deuterium quadrupole coupling is quite large, and in fact dwarfs the other internal fields. Thus the quadrupole coupling is the only interaction which requires consideration and the other internal fields may be safely neglected. The large size of the quadrupole coupling also permits investigation of motion over rates ranging from 10^3 s^{-1} to 10^{10} s^{-1}. It is relatively easy to incorporate ^2H as isotopic labels and the natural abundance of ^2H is low, practically eliminating background signal. In general for deuterons bonded to carbons, the electric field gradient tensor is axially symmetric and this axis is collinear with the C-D internuclear vector. Thus, the quadrupole coupling may serve as a potent probe of the geometry and orientation of deuterium nuclei. Molecular motional effects on deuterium spectra have consequently been exhaustively characterized. The next sections will cover the basics of deuterium NMR.

2.1.1 Deuterium Lineshapes

As mentioned above, the quadrupole coupling is quite large. For deuterons in alkyl compounds, $\frac{eQV_{zz}}{h} \approx 170$ kHz . For effects on lineshapes,[1] the rate constants of motions must be compared to this characteristic rate of ~170×10^3 s^{-1}. Molecular motion much slower than this (rate, $k < 10^3$ s^{-1}) produces no effect on the NMR lineshape. This motional regime is known as the rigid lattice limit. Molecular motion much faster than the characteristic rate, ($k > 10^7$ s^{-1}) produces significant averaging of the NMR lineshape, a regime known as the fast limit. An illustrative example of such motional rates is the ^2H lineshape of deuterons in a methyl group. The rigid lattice spectrum is the essentially the same as for all alkyl ^2H. For analysis of the effects of faster motion, the resonance

frequencies of the deuteron sites in a methyl group must be considered together. (Since the two resonance frequencies of a single deuteron are equally spaced about the Larmor frequency, we may consider just one while keeping in mind that the actual spectrum consists of both, calculating a band spectrum for powders by adding the reflection about zero. This simplification will be used subsequently in describing only one of the resonance frequencies for a deuteron.) For a given methyl group orientation in a powdered polycrystalline sample, each deuteron possesses its own (not necessarily different) resonance frequency. At sufficiently high temperature and corresponding motional hopping of deuterons between the three crystallographic sites on the methyl group, the three resonance frequencies are averaged and the three resonant frequencies are collapsed into one resonant frequency. The geometry of the methyl group imposes a relationship between the three resonance frequencies such that the motionally averaged powder lineshape is characteristic of that motion. For methyl group motion, the rigid lattice and fast limit lineshapes are shown schematically below:

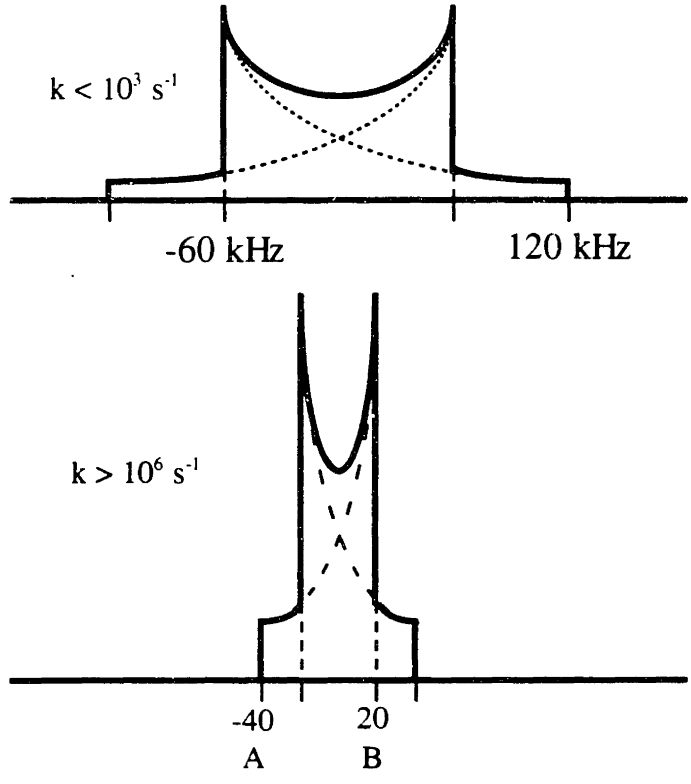

The overall Pake-style pattern is retained but the width of the lineshape is dramatically narrowed, by a factor of three. In fact, for motions with threefold symmetry (as this methyl group example) or higher symmetry, the lineshape always retains the Pake pattern (often called axial symmetry since the effective motionally averaged electric field gradient tensor has two degenerate principal values, thus the PAS has axial symmetry).[2] In common practice, motionally averaged lineshapes are calculated via the following procedure[1], using a methyl group as a specific example. The motion is assumed to occur between a small number of discrete sites, N, which for a methyl is 3. An N×N rate matrix is constructed with element ij being the rate constant for motional exchange from site i to j. For a methyl in the fast limit, for example:

$$\begin{pmatrix} -2\times10^9 & 10^9 & 10^9 \\ 10^9 & -2\times10^9 & 10^9 \\ 10^9 & 10^9 & -2\times10^9 \end{pmatrix}\left(s^{-1}\right) = \mathbf{R}$$

This exchange rate matrix, $\mathbf{R}$, must be conservative, that is, the sums of the elements in the rows must be zero, which corresponds to no net creation or destruction of deuterons. For a given crystallite orientation, the resonance frequencies of each site are then calculated. Two separate cases are examined. For the first (A), consider the methyl orientation in the lab frame corresponding to polar angles (109.5°, 0°) (109.5°, 120°) (109.5°, 240°). This corresponds to the case where the axis of motion is collinear with the magnetic field direction. The frequencies are all then all equal, $\frac{3}{4}\frac{eQV_{zz}}{h}\left(\frac{3\cos^2\theta-1}{2}\right)$ $=\frac{3}{4}\frac{eQV_{zz}}{h}\left(-\frac{1}{3}\right)$, and averaging produces no observable effect. Another instructive case (B) is that in which the polar angles are (90°, 0°) (35.26°, 125.3°) (144.74°, 125.3°). This is an instance in which the axis of methyl motion is perpendicular to the magnetic field direction. The frequencies are then $\frac{3}{4}\frac{eQV_{zz}}{h}\left(-\frac{1}{2}\quad\frac{1}{2}\quad\frac{1}{2}\right)$. A frequency matrix is then constructed with the site frequencies as the diagonal elements:

$$\begin{pmatrix} \omega_1 & & \\ & \omega_2 & \\ & & \omega_3 \end{pmatrix} = \boldsymbol{\omega} = \begin{pmatrix} -4\times10^5 & & \\ & 4\times10^5 & \\ & & 4\times10^5 \end{pmatrix} (\text{rad / s})$$

Then matrix $i\boldsymbol{\omega} + \mathbf{R}$ is constructed and its eigenvalues are determined by diagonalization.

$$\begin{pmatrix} -2\times10^9 - i4\times10^5 & 10^9 & 10^9 \\ 10^9 & -2\times10^9 + i4\times10^5 & 10^9 \\ 10^9 & 10^9 & -2\times10^9 + i4\times10^5 \end{pmatrix}$$

$$\Rightarrow \begin{pmatrix} -3\times10^9 + i4\times10^5 & -47 + i1.33\times10^5 & -3\times10^9 - i1.33\times10^5 \end{pmatrix} (\text{rad / s})$$

The imaginary component of the eigenvalues are averaged frequencies, while the real components correspond to damping coefficients. Thus in this example, the observable averaged frequency is the imaginary component of the eigenvalue with smallest real component. The motionally averaged frequency for case B is then ~20 kHz.

In this manner one may see the correspondence from the rigid lattice pattern to the one-third smaller averaged pattern. In the rigid lattice, at $\theta = 0°$, the frequency is $\frac{3}{4}\frac{eQV_{zz}}{h}$, while at $\theta = 90°$, the frequency is $\frac{3}{4}\frac{eQV_{zz}}{h}\left(-\frac{1}{2}\right)$. In the motionally averaged situation, for case (A) in which the axis of motion was parallel to the magnetic field, $\theta' = 0°$, the averaged frequency is $\frac{3}{4}\frac{eQV_{zz}}{h}\left(-\frac{1}{3}\right)$ while for case B in which the axis of motion was perpendicular to the field, $\theta' = 90°$, the averaged frequency is $\frac{3}{4}\frac{eQV_{zz}}{h}\left(\frac{1}{6}\right)$.

2.1.2 Deuterium Relaxation

As mentioned previously, spin lattice relaxation requires motion with rate constants near the Larmor precession frequency. The rate of spin lattice relaxation is also proportional to the size of the internal fields which are in involved and affected by the motion. Again, in deuterium NMR the quadrupole interaction is the only internal field which is necessary to consider. As a result, the fitting of observed relaxation rates to calculated motional rates is quantitative. Thus, deuterium NMR has served as a valuable

proving ground and powerful tool for investigating spin lattice relaxation and motional rates. This section will outline the theory and mechanisms involved.

The general formalism for spin lattice relaxation is given by Abragam[3]. In this formalism, the principal terms are the interaction representation density matrix, $\sigma^*(t)$, and the interaction representation perturbing Hamiltonian, $H_1^*(t)$. The evolution of the interaction density matrix follows the master equation,

$$\frac{d\sigma^*(t)}{dt} = -\int_0^\infty d\tau \overline{\left[H_1^*(t),\left[H_1^*(t-\tau),\sigma^*(t)\right]\right]}$$

Traditionally, one substitutes the perturbing Hamiltonian of interest and solves for the master equation in the form of the Bloch equations, i.e.,

$$\frac{d\langle \mathbf{I}_z \rangle}{dt} = -\frac{1}{T_1}\langle \mathbf{I}_z \rangle$$

$$\frac{d\langle \mathbf{I}_+ \rangle}{dt} = -\frac{1}{T_2}\langle \mathbf{I}_+ \rangle$$

The relaxation time constants are generally simplified in terms of the spectral density terms $J(\omega)$, which give the probability density at a given motional rate. These spectral densities are the Fourier transforms of the autocorrelation functions.

$$J(\omega) = \int d\tau\, e^{im\omega t}\, \langle H(t)H(t-\tau)\rangle$$

For deuterium, upon following this formalism, the spin lattice relaxation time constant T_1 is found to be:[4]

$$\frac{1}{T_1} = \frac{1}{3}\left(\frac{3eQV_{zz}}{4h}\right)^2 \left[J_1(\omega_0) + 4J_2(2\omega_0)\right]$$

where ω_0 is the Larmor frequency. In this manner, the spin-lattice relaxation may be seen to be fastest when the motional rate is nearest the Larmor frequency. The relaxation rate depends on the orientation of the dynamic group - the relaxation is anisotropic. The specific pattern is highly dependent on the details of the motion. In practice, the calculation of the relaxation rate due to motion requires both the exchange rate matrix and a geometric description of the jumps between sites, usually provided in terms of Euler Angles relating axis systems.[5, 6]

It must be emphasized that the preceding analysis results in a single relaxation rate for the entire set of sites. An unusual case in which this fact is crucial will be described in the next chapter. Analysis of this case would benefit from a prefatory introduction. Consider two methyl groups whose deuterons are hopping between their three canonical positions with two different rate constants, say 10^8 s^{-1} and 10^{11} s^{-1}, with a Larmor frequency of 3.6×10^8(rad/s). Assume that the entire methyls may exchange position (including carbons) such that the local environment forces the methyl group previously at rate 10^8 to alter its rate to 10^{11} s^{-1}. Let this exchange rate be 1 s^{-1}. A complete description of the dynamics then requires a rate matrix as follows:

$$\begin{pmatrix} -2\times10^8-1 & 10^8 & 10^8 & 1 & & \\ 10^8 & -2\times10^8-1 & 10^8 & & 1 & \\ 10^8 & 10^8 & -2\times10^8-1 & & & 1 \\ 1 & & & -2\times10^{11}-1 & 10^{11} & 10^{11} \\ & 1 & & 10^{11} & -2\times10^{11}-1 & 10^{11} \\ & & 1 & 10^{11} & 10^{11} & -2\times10^{11}-1 \end{pmatrix}$$

While this rate matrix would produce the correct result for the lineshape analysis, the result for the relaxation calculation would be grossly incorrect. Consider the limiting case where there was no exchange between methyl groups. The two methyl groups, with different motional rates would thus have two different relaxation rates, yet the preceding analysis produces a single T_1 for both. (The calculated T_1 would be essentially that of the methyl group which in isolation would have the shortest T_1 since the spectral density from the matrix as a whole consists of the sum of the contributions from each type of motion). To illustrate a more proper analysis, the analogy of treating the relaxation as a fluid dynamics problem is beneficial. The two different methyl groups may be thought of as sinks, with distinct drainage rates. These rates depend directly on the hopping rate of that methyl group. The exchange between methyls may be thought of as a connection between the two sinks with a specific flow rate. Thus, when the two sinks drain at different rates, in effect the slower bath may flow into the faster and thence apparently drain at a faster rate. The

calculation of this effect proceeds as follows. The six sites are divided into two groups corresponding to the individual methyl groups. The diagonal submatrices for each subgroup are used in the conventional analysis to produce a T_1 for that group as well as to calculate the lineshape for that group. This subgroup T_1 is then placed along the diagonal of the submatrices for calculations of the dynamics of the populations

$$\begin{pmatrix} 1/T_1^1 & & & 1 & & \\ & 1/T_1^1 & & & 1 & \\ & & 1/T_1^1 & & & 1 \\ 1 & & & 1/T_1^2 & & \\ & 1 & & & 1/T_1^2 & \\ & & 1 & & & 1/T_1^2 \end{pmatrix} = \mathbf{R}_{relax}$$

Whereas in the conventional calculations a single T_1 was generated, in this procedure an effective relaxation rate matrix is generated. The population at a given time is calculated by using the exponentiated matrix $e^{-\mathbf{R}_{relax}t}$ in place of e^{-t/T_1}. The simulated relaxation spectra in the next chapter rely on this type of calculation.

2.2 Magic Angle Spinning

Whereas the preceding discussion dealt with molecular motion as a form of spatial dynamics, this section introduces Magic Angle Spinning(MAS), also formally spatial dynamics, albeit imposed by man rather than nature. Just as molecular motion, MAS averages internal fields and produces narrowed lineshapes. This section describes the effect of MAS on two internal fields: the anisotropic chemical shift and the dipole coupling.

2.2.1 MAS and CSA Lineshapes

MAS has found great use as a tool to narrow chemical shift anisotropy, thus improving spectral resolution in dilute spins such as ^{13}C and ^{15}N. The effect of MAS is

to split what would be a broad powder lineshape into a set of narrow lines spaced at the spinning frequency. This result can be rationalized as follows. The resonance frequency of a spin with an anisotropic chemical shift depends on the orientation of the crystallite. If the sample as a whole is rotated, the resonance frequency will change as the crystallite orientation changes. When a full turn is completed, however, the crystallite orientation and thus the resonance frequency returns to the original value. If the sample is rotated continuously, the resonance frequency for a given spin traces out the same trajectory each period. When the resonance frequency is observed over many cycles, this imparts a periodicity to the signal. The Fourier transform of such a signal consists of a line at the time-average of the frequencies traced out, with additional lines spaced at the spinning frequency. In order to best average the chemical shift to produce the narrowest lines, the sample should be spun at an angle with respect to the magnetic field axis that minimizes the function $\frac{3\cos^2\theta-1}{2}$, that is, at the magic angle 54.7°. Examples of such MAS spectra will be shown in the next chapter.

2.2.2 MAS and Dipole Coupling

The technique of Magic Angle Spinning was originally proposed as a method to average the dipole coupling.[7] While the CSA may be narrowed into sidebands when the spinning frequency is smaller than the full frequency breadth imparted by the CSA, the spinning frequency must exceed the dipole coupling constant in order to fully average the dipole coupling. When this condition is met, however, the effective time average of a dipole coupling is zero, thus MAS serves as an extremely effective attenuator of small dipole couplings. Since dipole couplings are direct indicators of structural information - relating the distance between two spins - this complete averaging is inopportune in cases where measurement of dipole couplings is the goal.

2.3 Molecular Motion Combined with MAS

One peculiar situation described in the next chapter involves the interference of these two forms of spatial dynamics, molecular motion and Magic Angle Spinning. In this situation, the molecular motion spoils the narrowing induced by MAS.[8] Without molecular motion, MAS causes the resonance frequency to trace out the same path every rotor period. At each rotor period, the resonance frequency returns to the same value, a situation called refocusing. Thus, the MAS averaging is consistent and effective. When molecular motion is much faster than the spinning frequency, the possible frequency range is narrowed, and MAS still produces consistent and effective refocusing and thus averaging. If however, the molecular motion occurs on a time scale similar to the rotor period(~100 μs = 1/(10 kHz))then, a single molecular reorientation may occur during a rotor cycle. This single reorientation places the spin in a crystallite orientation that will result in a different resonance frequency when the rotor cycle is completed, and thus refocusing/averaging by MAS is ineffective. The net result in such situations is a spectrum where sidebands are present, but greatly broadened. Such an effect is shown in the next chapter along with simulations.

2.4 Molecular Motion Interference with Decoupling

A final effect of molecular motion illustrated in the next chapter is due to interference not between dynamics solely in Cartesian space, but between dynamics in Cartesian space and spin space. In this case, the molecular motion acts to spoil the narrowing produced by ^{1}H decoupling for ^{13}C or other dilute spins.[9] Again the two dynamics occur on similar time scales, namely ~10 μs = 1/(100 kHz), since standard ^{1}H decoupling corresponds to nutation at a frequency of ~100 kHz. The effect is a broadening of the lines for spins dipole coupled to ^{1}H which undergo motion at this rate. This effect may be estimated via the same formalism used for spin-lattice relaxation. In this case the

parameter of interest is not T_1 but T_2. This inverse of this parameter roughly represents the linewidth of the affected spins.

$$\frac{1}{T_2} = \frac{4\gamma_I^2\gamma_S^2\hbar^2}{15r^6} I(I+1)\frac{\tau_c}{1+\omega_I^2\tau_c^2}$$

where I corresponds to ^{1}H, S is ^{13}C, r is the internuclear distance, ω_I is the decoupling nutation frequency, and τ_C is the correlation time of the molecular motion (assumed to be random and isotropic). For the methyl motion involved in the following chapter, such a random and isotropic process would likely be a poor approximation so the simulations accompanying the next chapter are calculated using a program designed to numerically emulate the situation.

References

1. R. J. Wittebort, E. T. Olejniczak, R. G. Griffin, *J. Chem. Phys.* **86**, 5411-5420 (1987).
2. D. A. Torchia, A. Szabo, *J. Magn. Reson.* **64**, 135-141 (1985).
3. A. Abragam, *Principles of Nuclear Magnetism* (Oxford University Press, Oxford, 1961).
4. D. A. Torchia, A. Szabo, *J. Magn. Reson.* **49**, 107-121 (1982).
5. R. J. Wittebort, A. Szabo, *J. Chem. Phys.* **69**, 1722-1736 (1978).
6. R. R. Vold, R. L. Vold, in *Advances in Magnetic and Optical Resonance* W. S. Warren, Ed. (Academic Press, Inc, 1991), vol. 16, pp. 85-171.
7. E. R. Andrew, A. Bradbury, R. G. Eades, *Nature* **182**, 1659 (1958).
8. A. Schmidt, *Journal of Chemical Physics* **85**, 4248-4253 (1986).
9. W. P. Rothwell, J. S. Waugh, *J. Chem. Phys.* **74**, 2721-2732 (1981).

3. Molecular Dynamics of Methyls Bonded to W and Ta

3.1 Introduction

Organometallic bonding and structure is an area of significant interest. The chemistry of organometallics is rich, with research opening new vistas from the basic nature of bonding and reactions to applications to new materials and improved catalysis. This chapter examines one such vista, namely the unusual dynamics discovered in methyls bonded to the metals Tungsten and Tantalum in a particular class of compounds.

The origin of the interest in these compounds was evidence that they exhibit an unusual form of bonding which may be involved in the mechanism of olefinic polymerization. One proposed mechanism of polymerization involves a distortion of the canonical metal-alkyl bonding patterns to a form known as an agostic bond.[1, 2] In this bond, an electrophilic metal draws close both a hydrogen atom and the electron density of its bond to a carbon, as shown schematically below.

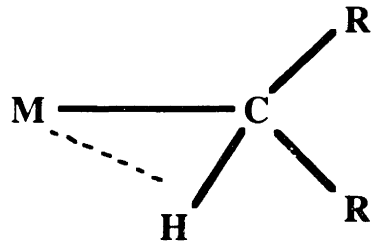

Study of a collection of Tungsten compounds provided evidence that some of these compounds were exhibiting such agostic interactions. In addition, some of these compounds exhibited unusual dynamic behavior of methyls directly bonded to the metal. An interesting NMR phenomenon was thus discovered,[3] in which a ^{13}C methyl line broadened, disappeared, and reappeared at the same chemical shift as the temperature was lowered. This behavior could not be explained via conventional motional exchange between sites. It was hoped that this behavior could be understood and perhaps found to be related to agostic interaction. This lead to the work described in the first section of this chapter which delineates the ^{2}H and ^{13}C motional studies and quantitative analysis.[4]

The second section describes further studies which were pursued to investigate the existence of agostic interactions in an analogous Tantalum compound, which unearthed a different but equally unusually motional effect on NMR spectra. These two examples illustrate some of the diverse chemistry of organometallics as well as the fascinating interplay of motion and NMR spectroscopy.

3.2 Tungsten

This section describes the results of Magic Angle Spinning (MAS) ^{13}C and static ^{2}H NMR studies of the dynamics of the methyl groups coordinated to Tungsten in $[WCp^{*}Me_4][PF_6]$ ($Cp^{*}= \eta^{5}$-C_5Me_5). Solution ^{1}H NMR studies[5] of the complex indicated that the methyls coordinated to the metal were inequivalent below ~300K and gave rise to sharp resonances in the ratio of 3:1 below 243K. (Hereafter "coordinated to the metal" will be understood.) X-ray studies confirmed that the complex has a trigonal bipyramidal structure in which three methyl groups occupy positions in an equatorial plane and the fourth occupies the axial position opposite the pentamethylcyclopentadienyl ring. $[WCp^{*}Me_4]^{+}$ readily loses a proton to yield unstable $WCp^{*}Me_3(CH_2)$ in which the two methylene protons are grossly inequivalent, presumably as a consequence of an agostic interaction of one of the methylene C-H bonds with the metal. Recently, Green and co-workers[6] have claimed, on the basis of variable-temperature studies of partially deuterated $[WCp^{*}Me_4]^{+}$, that the equatorial methyl groups in $[WCp^{*}Me_4]^{+}$ are also agostic, i.e., that at any given instant one of the nine C-H bonds is interacting weakly with the metal. Activation of an α hydrogen through an agostic interaction could conceivably be the source of the relatively high acidity of $[WCp^{*}Me_4]^{+}$ and its ready deprotonation by triethylamine. Thus, the existence of anomalous methyl dynamics was of considerable interest in the context of agostic interactions. The temperature dependent broadening of the axial methyl ^{13}C line is shown to be due to interference between ^{1}H decoupling and methyl motion when the motional rate and decoupling nutation frequency are comparable. This is

confirmed by the absence of broadening in the ^{2}H labeled compound and further ^{2}H NMR lineshape and T_1 studies. The measured barrier to methyl hopping, 26 kJ/mole, is among the highest reported to date. Despite the unusual dynamics and chemical reactivity of this complex, an X-ray crystal study reveals that there is no evidence for an agostic interaction in either the axial or equatorial methyl groups.

3.2.1 MAS ^{13}C Studies

Sample preparation. The isotopically labeled compounds used in this study were generously provided by members of Professor Richard Schrock's research group. [WCp*($^{13}CH_3$)4][PF_6] and [WCp*($^{13}CD_3$)4][PF_6] were synthesized by Shifang Luo. All compounds were prepared by methods analogous to those reported in the literature.[5]

^{13}C NMR Measurements. MAS ^{13}C spectra were obtained on a custom built spectrometer with a 7.6 T magnet, corresponding to a ^{13}C resonance frequency of 79 MHz. Typically, spectra were observed using a ^{13}C 90° pulse of length 2.5 μs and CW ^{1}H decoupling during acquisition with a field strength of 100 kHz corresponding to a ^{1}H 90° pulse length of 2.5 μs. All spectra shown were taken without cross polarization, although spectra obtained with cross polarization (not shown) were essentially identical. Spinning speeds were 4.0 kHz. Recycle times varied from 5 s at high temperature to 120 s at low temperature. Selective inversion-recovery was performed with a rotor-synchronized DANTE sequence with 4 cycles to selectively invert a single line, followed by a recovery delay (without ^{1}H decoupling), then a ^{13}C 90° pulse and acquisition as above. Temperatures were calibrated using the temperature dependent ^{207}Pb chemical shift of Lead Nitrate in a manner described by Bielecki.[7]

^{13}C NMR Simulations. Simulations of the MAS ^{13}C NMR lineshape in the axial methyl $^{13}CH_3$ as a function of the proton hopping rate were performed using a program generously provided by Boqin Sun, and discussed elsewhere.[8] Input parameters include the ^{1}H hopping rate, the ^{1}H decoupling power, which was assumed to be 100 kHz as described above, the ^{13}C chemical shift tensor, the ^{13}C-^{1}H and ^{1}H-^{1}H

dipole coupling constants, which were assumed to be 27 kHz and 25 kHz, respectively, based on typical values of C-H bond lengths and H-H distances in methyl groups, and the geometry of these interacting spins.

^{13}C NMR Spectra of [WCp*Me$_4$][PF$_6$]. The MAS ^{13}C NMR spectra of [WCp*(^{13}CH$_3$)$_4$][PF$_6$] are shown in Figures 3-1 and 3-2 at temperatures ranging from 25 to -120°C. The isotropic axial and equatorial methyl lines are at 105 and 80 ppm, respectively, as in the reported solution ^{13}C NMR study.[5] The lines at 122 and 11 ppm are from the natural abundance ring and methyl carbons of the Cp* ligand, and the remaining lines are rotational sidebands. As the temperature is decreased the equatorial methyl line at 80 ppm broadens until at -120°C it has separated into its three inequivalent components. At the same time, the axial line at 105 ppm gradually broadens as the temperature is decreased, without shifting in frequency, until at -58°C it disappears into the baseline. As the temperature is further decreased the line reappears at the same frequency and narrows. This broadening of the axial ^{13}CH$_3$ line is similar to that reported recently in the ^{15}N spectra of the ^{15}NH$_3$ in alanine.[8] This broadening is caused by interference between the ^{1}H decoupling and motion as first described by Rothwell and Waugh.[9] When the motional rate is comparable to the ^{1}H decoupling nutation frequency, the two processes interfere destructively. The result is ineffective decoupling and thus a severe broadening of the resonances that are coupled to these protons. Invocation of this mechanism for this effect is supported by the fact that when ^{13}CH$_3$ is replaced by ^{13}CD$_3$, in which all couplings (carbon-deuterium and deuterium-deuterium) are small and effectively removed by magic angle spinning, the axial methyl line does not exhibit this broadening, as shown in the MAS ^{13}C NMR spectra of [WCp*(^{13}CD$_3$)$_4$][PF$_6$] (Figure 3-1). Since the ^{1}H decoupling fields that were used were typically 100 kHz, the broadening indicates methyl motional rates of approximately 10^5 s^{-1} at -58°C and approximate rates of 10^7 s^{-1} at 25°C and 10^3 s^{-1} at -120°C. Figure 3-2 shows a comparison of the experimental and best fit simulated centerbands of the axial methyl at the

indicated temperatures and rates. The ^{13}C chemical shift anisotropy parameters used for the axial methyl group were δ=-59 ppm and η = 0, which were extracted using the method of Herzfeld and Berger from the spinning sideband intensities.[10] A tetrahedral geometry was used for all displayed simulations for the axial methyl. The simulation results are not sensitive to a specific geometry, that is, distortions of methyl tetrahedral symmetry of the scale estimated for an agostic interaction would not produce significant deviations.

Figure 3-1. MAS ^{13}C NMR spectra of $[WCp^*(^{13}CH_3)_4][PF_6]$ and $[WCp^*(^{13}CD_3)_4][PF_6]$ at the temperatures indicated and a spinning speed of 4.0 kHz. The axial methyl line at 105 ppm disappears and reappears in the CH_3 but not in the CD_3 sample.

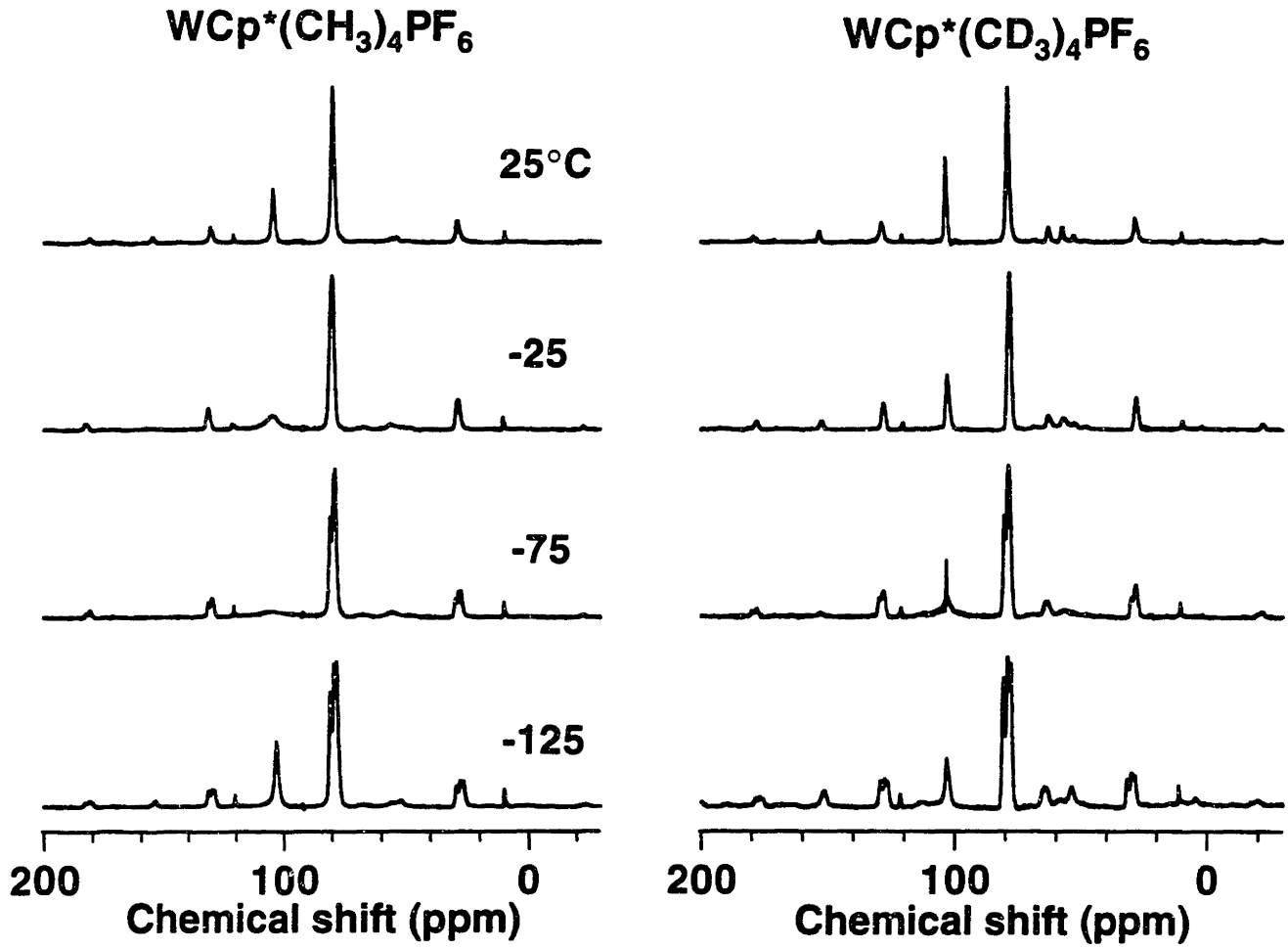
WCp*(CH3)4PF6
WCp*(CD3)4PF6
25°C
-25
-75
-125
200
100
0
Chemical shift (ppm)
200
100
0
Chemical shift (ppm)

Figure 3-2. Comparison of experimental and simulated ^{13}C lineshape of the axial methyl of $[WCp^*(^{13}CH_3)_4][PF_6]$ at the temperatures and rates indicated. The simulations reproduce the temperature dependent broadening of the axial methyl line at 105 ppm.

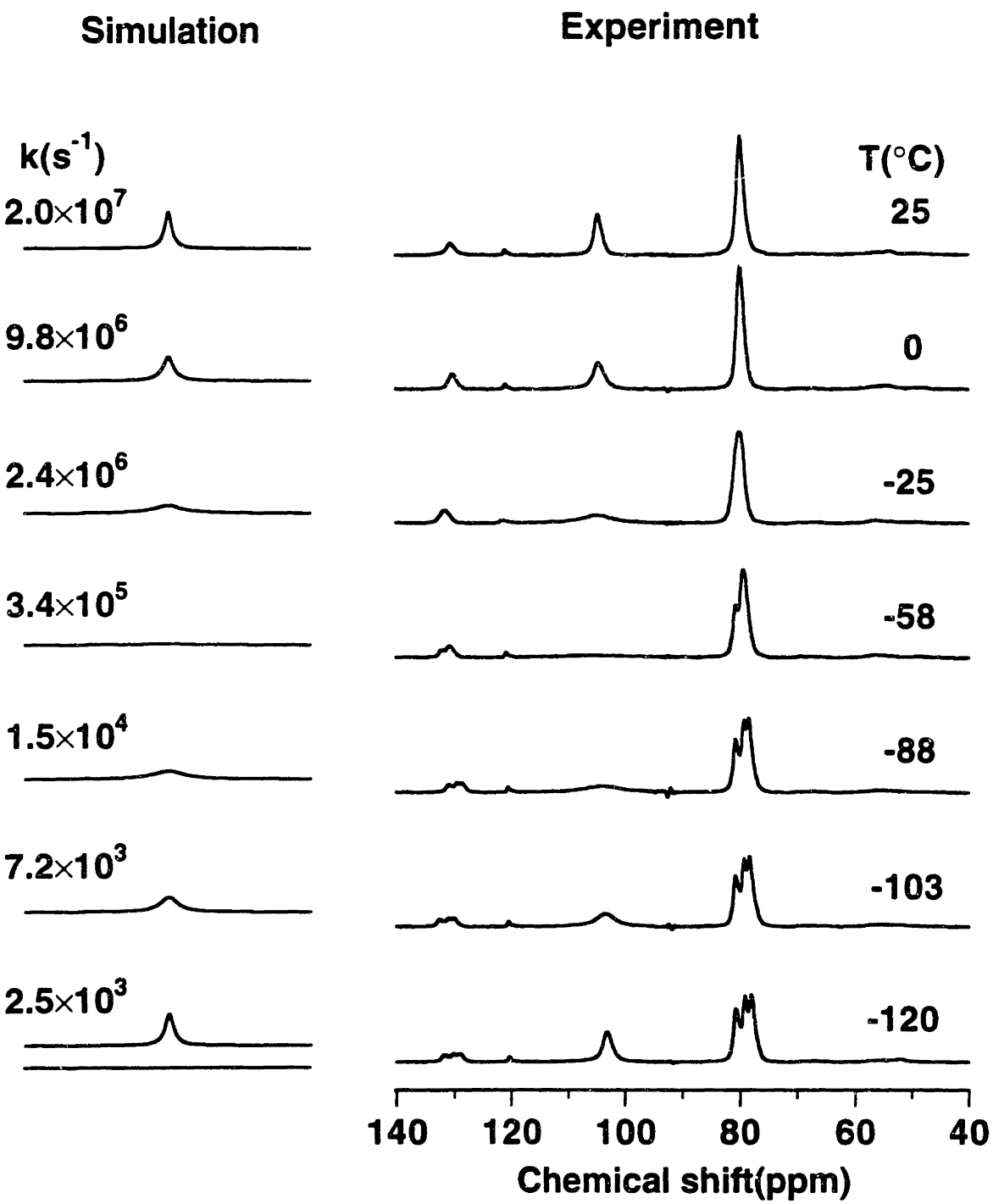
Simulation
Experiment
k(s-1)
2.0×10^7
9.8×10^6
2.4×10^6
3.4×10^5
1.5×10^4
7.2×10^3
2.5×10^3
T(°C)
25
0
-25
-58
-88
-103
-120
140
120
100
80
60
40
Chemical shift(ppm)

For reasons to be explained below, the rate of exchange of axial and equatorial methyls is of importance. The reported solution ^{1}H NMR studies indicated that axial and equatorial methyls exchanged at a rate of ~50 s^{-1} at 25°C. To ascertain these rates in the solid state, a selective inversion-recovery experiment was performed. The axial methyl was inverted with a DANTE sequence and its recovery was observed. The observed spectra at the indicated recovery times are shown in Figure 3-3 for $[WCp^{*}(^{13}CD_3)_4][PF_6]$. The intensities of the axial and equatorial methyl lines are shown as a function of recovery time at 25°C, 0°C, and -25°C in Figure 3-4. The decrease in the intensity of the equatorial line as the inverted axial line recovers indicates magnetization (population) exchange. This magnetization exchange is nearly identical at the lower temperatures which indicates that in this regime, magnetization exchange is due to spin-diffusion. Such spin-diffusion exchange is dependent on the strengths of the spin couplings, which are independent of temperature. (The ^{2}H compound was used to minimize the effects of ^{1}H mediated spin diffusion.) In contrast, the magnetization exchange is increased at 25°C and is therefore due in part to chemical exchange which would likewise increase with temperature. The magnetization exchange at 25°C is on the timescale of 0.2 to 1 s which indicates that the chemical exchange rate is on the order of 1 to 5 s^{-1}. The exact chemical exchange rate is difficult to completely separate from spin diffusion at 25°C and is obscured completely at the lower temperatures. The existence of chemical exchange and its order of magnitude are sufficient for the subsequent analysis.

Figure 3-3. Selective inversion-recovery MAS ^{13}C NMR spectra of $[WCp^*(^{13}CD_3)_4][PF_6]$ at 25°C and the recovery times indicated.

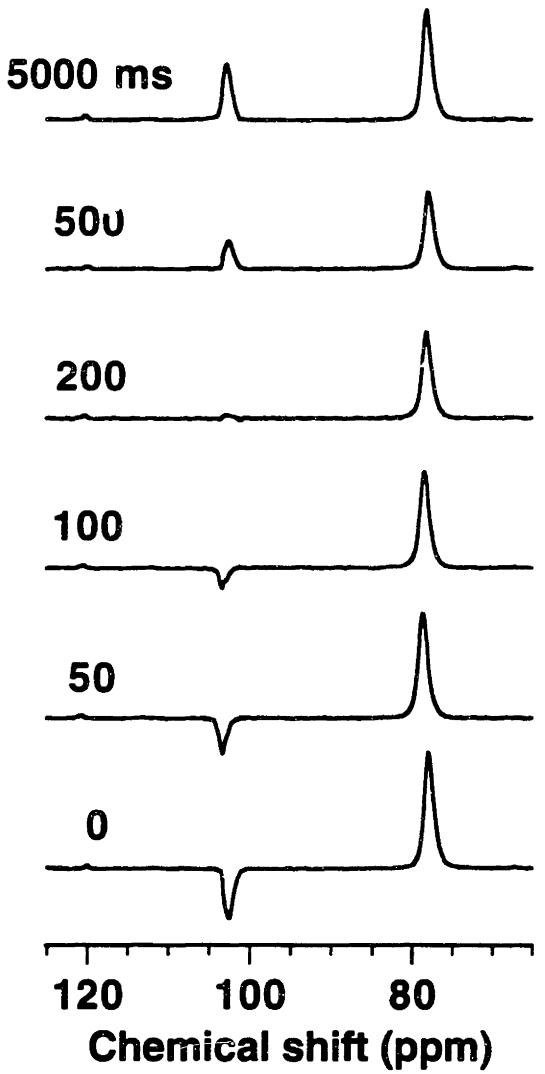
5000 ms
500
200
100
50
0
120
100
80
Chemical shift (ppm)

Figure 3-4. Comparison of the ^{13}C selective inversion-recovery of the axial and equatorial methyl lines of $[WCp^*(^{13}CD_3)_4][PF_6]$ as a function of recovery time at the indicated temperatures. The difference in recovery time between 25°C and the lower temperatures indicates that the magnetization exchange is temperature dependent and thus due in part to chemical exchange.

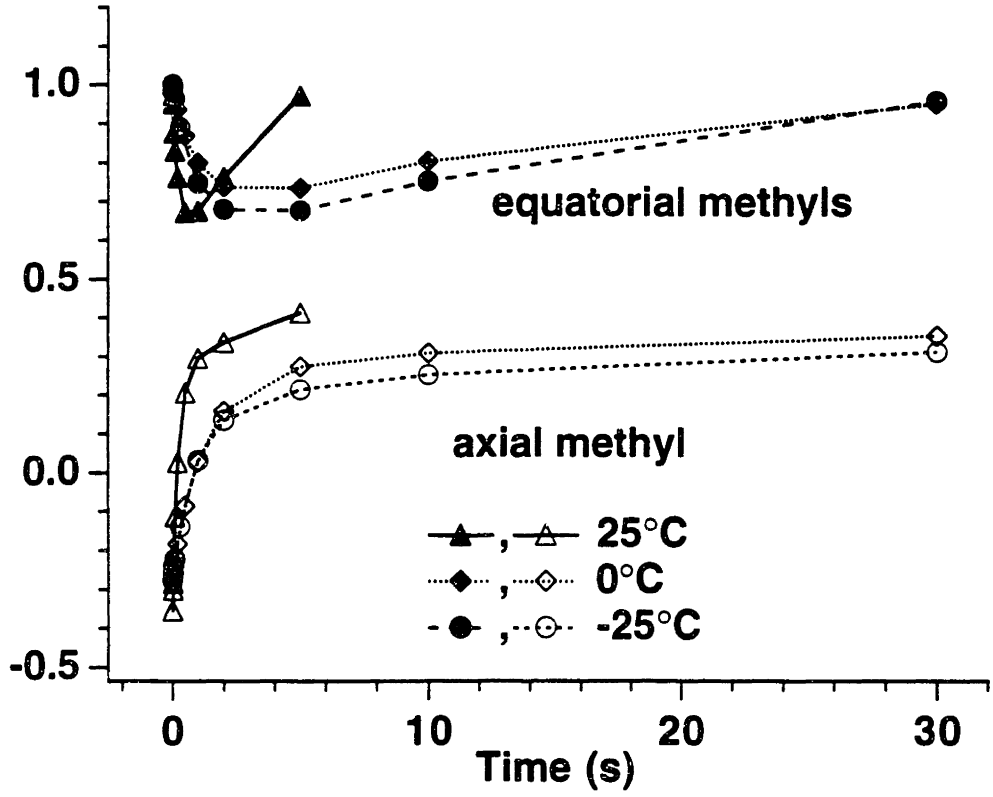
1.0
0.5
0.0
-0.5
0
10
20
30
Time (s)
equatorial methyls
axial methyl
25°C
0°C
-25°C

3.2.2 Static ^2H Studies

Sample Preparation. $[WCp^*(CD_3)_4][PF_6]$ was synthesized and provided by Andreas Grohmann of Professor Richard Schrock's research group.

^2H NMR Measurements. Static(non MAS) ^2H spectra of $[WCp^*(CD_3)_4][PF_6]$ were obtained on a custom built spectrometer with a 9.4T magnet, corresponding to a deuterium resonance frequency of 61 MHz. Typically, spectra were observed using a quadrupole echo pulse sequence with ^2H 90° pulse lengths of 2 μs and echo times of 30 μs. The sampling rate was 1 MHz. Recycle times varied from 3 s at high temperatures to 60 s at low temperature. T_1 inversion-recovery was performed with a non-selective 180° pulse of 4 μs followed by a recovery delay and a quadrupole echo sequence for observation.

^2H NMR Simulations. Deuterium NMR simulations were performed using algorithms described elsewhere[11] in a program incorporating the modifications described in the previous chapter. Input parameters include the motional model (rates and geometries) and quadrupole coupling parameters. Using a given motional model, the program calculates the powder average of the motion dependent lineshape and relaxation rates for a polycrystalline sample.

^2H NMR Lineshapes of $[WCp^*(CD_3)_4][PF_6]$. A ^2H NMR study was undertaken in order to confirm and further quantify the dynamics and the estimated rates proposed on the basis of the ^{13}C NMR spectral broadening. The ^2H NMR quadrupole echo spectrum of $[WCp^*(CD_3)_4][PF_6]$ at -90°C as well as a simulated spectrum is shown in Figure 3-5. Since all the methyls coordinated to Tungsten are ^2H labeled, the static powder pattern spectrum consists of the sum of the contributions from each of these. The -90°C spectrum shows a major component with a quadrupole splitting of approximately 40 kHz and a minor component with quadrupole splittings of approximately 130 kHz. The splitting of the major component is indicative of a methyl in the fast limit ($k > 10^7\ s^{-1}$) while the splitting of the minor component is indicative of a methyl in the slow limit ($k <$

10^4 s^{-1}). The relative intensities of the major and minor components is consistent with the assignment of the major component to 3 methyls in the fast limit and the minor component to a single methyl in the slow limit as is illustrated in the simulation. The simulation shows the calculated spectrum for 3 equivalent methyls with rates 3.4×10^{11} s^{-1} and a single methyl with a rate of 10^4 s^{-1}. The component with a motional rate of 10^4 s^{-1} at -90°C is assigned to the axial methyl and confirms the general motional rates obtained from the ^{13}C NMR data.

Figure 3-5. Quadrupole echo ^{2}H NMR spectra of [WCp*$(CD_3)_4$][PF_6] at -90°C. The narrower component with a splitting of 40 kHz is due to 3 motionally averaged methyls (rate $k > 10^7\ s^{-1}$) and the wide component with a splitting of 120 kHz is due to a methyl in the rigid lattice limit ($k > 10^7\ s^{-1}$).

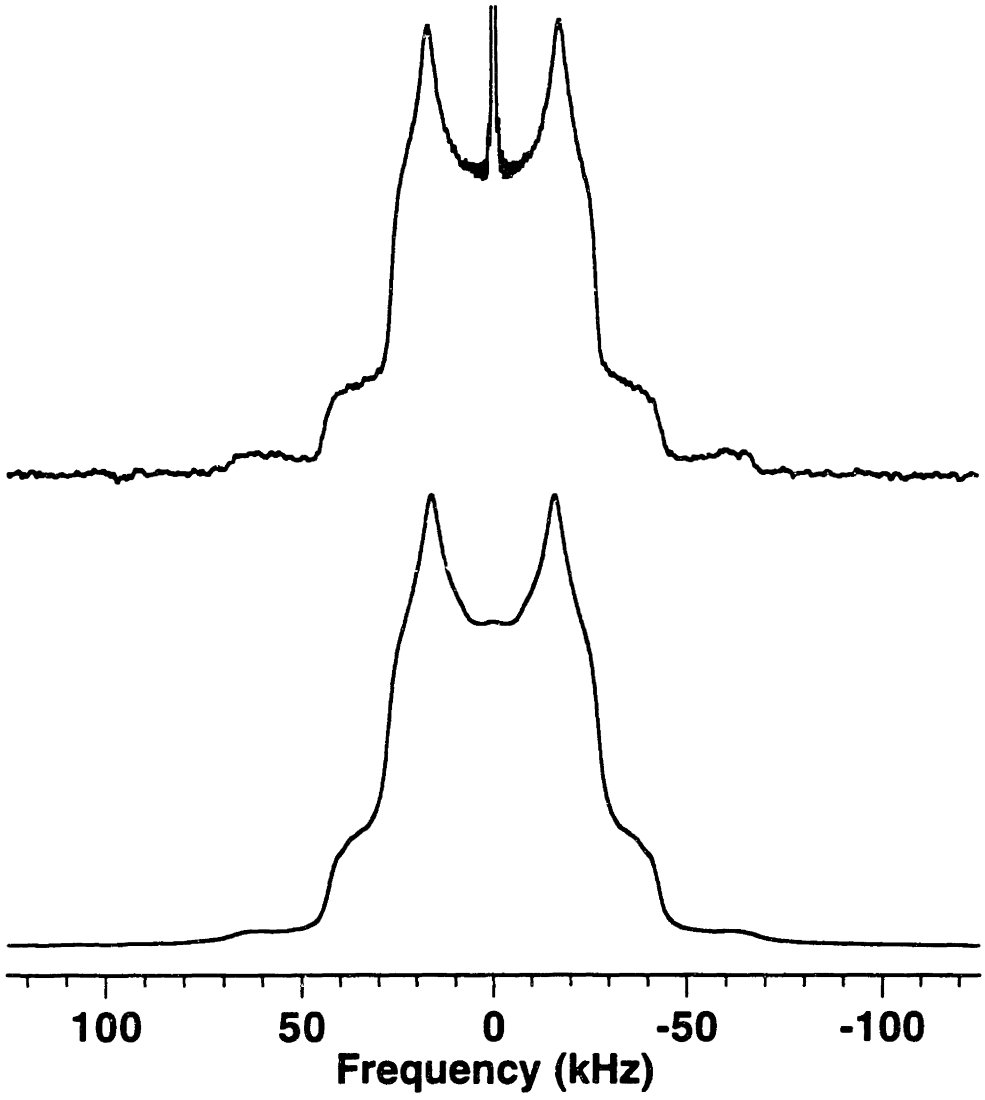
100
50
0
-50
-100
Frequency (kHz)

The ^2H NMR lineshape of the major component due to the three equatorial methyls is unusual in two ways. The lineshape is significantly asymmetric with $\eta = 0.2$ and has a calculated rigid lattice eQV_0/h value of 178 kHz. This eQV_0/h value is slightly large for a methyl group. However, in $[WCp^*(CD_3)_4][PF_6]$ the methyls are directly bonded to a transition metal, which exerts strong electrostatic effects as shown in the downfield shifted ^{13}C resonances for both the axial and equatorial methyls. Consequently such a ^2H quadrupole coupling constant is not extraordinary. What is more intriguing is that the major component *motionally narrowed* ^2H lineshape shows such a large asymmetry. The existence of similar asymmetries has been noted in other deuterated methyl compounds such as thymine,[12] hexamethylbenzene,[13] and octatryienylideneimines.[14] Theoretically, the averaging process due to motions of 3-fold (or higher) symmetry, such as a tetrahedral methyl group, results in an axially symmetric motionally narrowed lineshape.[15] Several hypotheses have been presented to explain these observed asymmetries, but a consensus has not yet been achieved. Hiyama, *et. al.*,[12] have presented evidence that the asymmetry is due to distortions in the electric field gradient. Specifically, in their study of thymine the asymmetry was ascribed to the presence of an electrostatic charge on the nearby exocyclic oxygen as indicated by ab initio electronic orbital calculations. Others have argued that asymmetries are also observed in nonpolar compounds which cannot be explained in this manner. Some have proposed that distortions in the symmetry of the motion are responsible for the asymmetry. Hoatson, *et. al.*,[13] interpret their results for hexamethylbenzene as distortions in the 6 fold ring motion, whereas Wann and Harbison[14] invoke a distortion in the 3-fold geometry of the methyl itself to explain the asymmetry in octatrienylideneimines. A method similar to that of Wann and Harbison satisfactorily reproduces the experimental lineshape, using the following reasoning: The X-ray structure of $[WCp^*Me_4][PF_6]$ shows a distortion of the plane of the equatorial methyl carbons downward from the Tungsten center such that the C_{axial}-W-$C_{equatorial}$ bond angles are about 77°, presumably as a consequence of

repulsion by the methyl groups in the Cp* ligand. Bending of the equatorial methyl groups would suggest that the carbon-hydrogen bonds in the methyl groups also would be distorted. In addition, distortion of the geometry can be readily simulated, since calculations of the motionally averaged lineshapes depend explicitly on geometry. All simulations employed a distortion of the methyl geometry, in the terminology of Wann and Harbison, of α = 111.5°, β = 109.5°, ϕ = 124° as opposed to the canonical values of α = 109.5°, β = 109.5°, ϕ = 120° as illustrated in Figure 3-6. It is not possible to discredit the hypothesis that the asymmetry is due to electrostatic effects, which is quite plausible in light of the fact that $[WCp^*Me_4]^+$ is a charged species. It is certainly possible that the large asymmetry is the result of a combination of both geometric and electrostatic effects.

Figure 3-6. Illustration of the geometric distortion used in the ^{2}H NMR lineshape simulations of the equatorial methyl groups

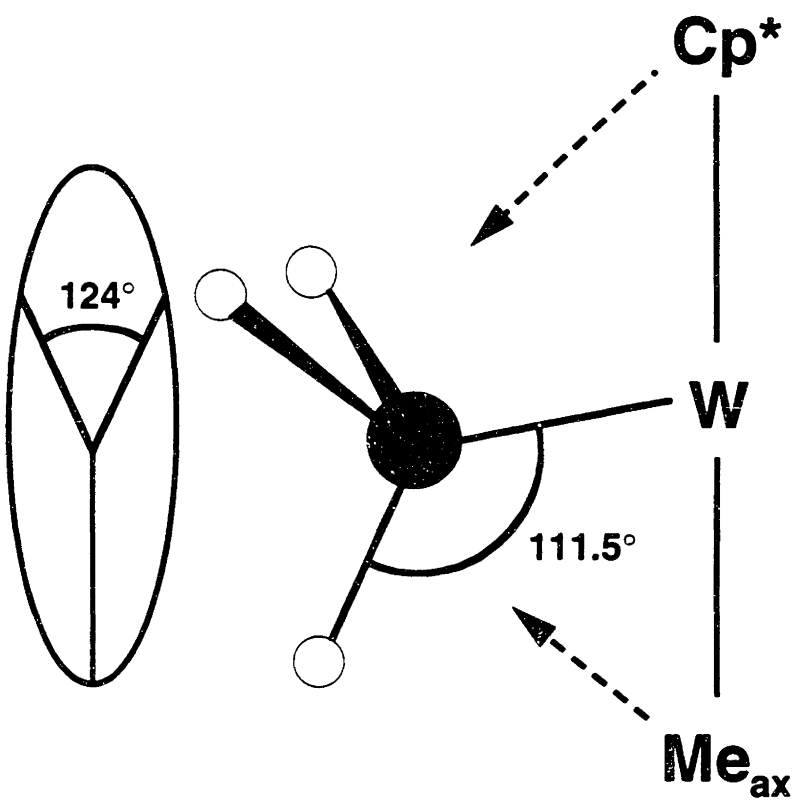
Cp*
124°
W
111.5°
Me$_{ax}$

^{2}H NMR T_1 Relaxation of [WCp*(CD3)4][PF6]. In order to further quantify the motional model, ^{2}H T_1 inversion-recovery measurements were performed over a range of temperatures. The contributions from the individual components are more difficult to separate at temperatures approaching 25°C, where both equatorial and axial methyls are in the fast limit and exhibit motionally averaged lineshapes of comparable breadth. Nevertheless, the T_1 inversion-recovery spectra at 25°C and the simulations that best fit the spectra are shown in Figure 3-7. At this temperature the axial methyl hopping rate is comparable to the Larmor frequency (61 MHz) so its T_1 is short (~20 ms). The hopping rate of the equatorial methyls (assumed to be the same for all three) is higher, resulting in a longer T_1 of several hundred ms. The simulated inversion recovery spectra for these two components are shown in dashed and dotted lines, along with the sum, shown as a solid line. This sum reproduces well the primary features of the experimental spectra.

Figure 3-7. Experimental and simulated inversion-recovery ^{2}H NMR spectra of [WCp*$(CD_3)_4$][PF_6] at 25°C and the recovery times indicated. The simulated spectra show the individual contributions of the axial methyl (long-dashed) and equatorial methyls (short-dashed), displaying the different intrinsic relaxation times, and the sum (solid curve). The rates used in the simulations were 2.4×10^{11} s^{-1} for the equatorial methyl motion, 3.0×10^{7} s^{-1} for the axial methyl motion, and 1.0 s^{-1} for the chemical exchange between axial and equatorial methyls.

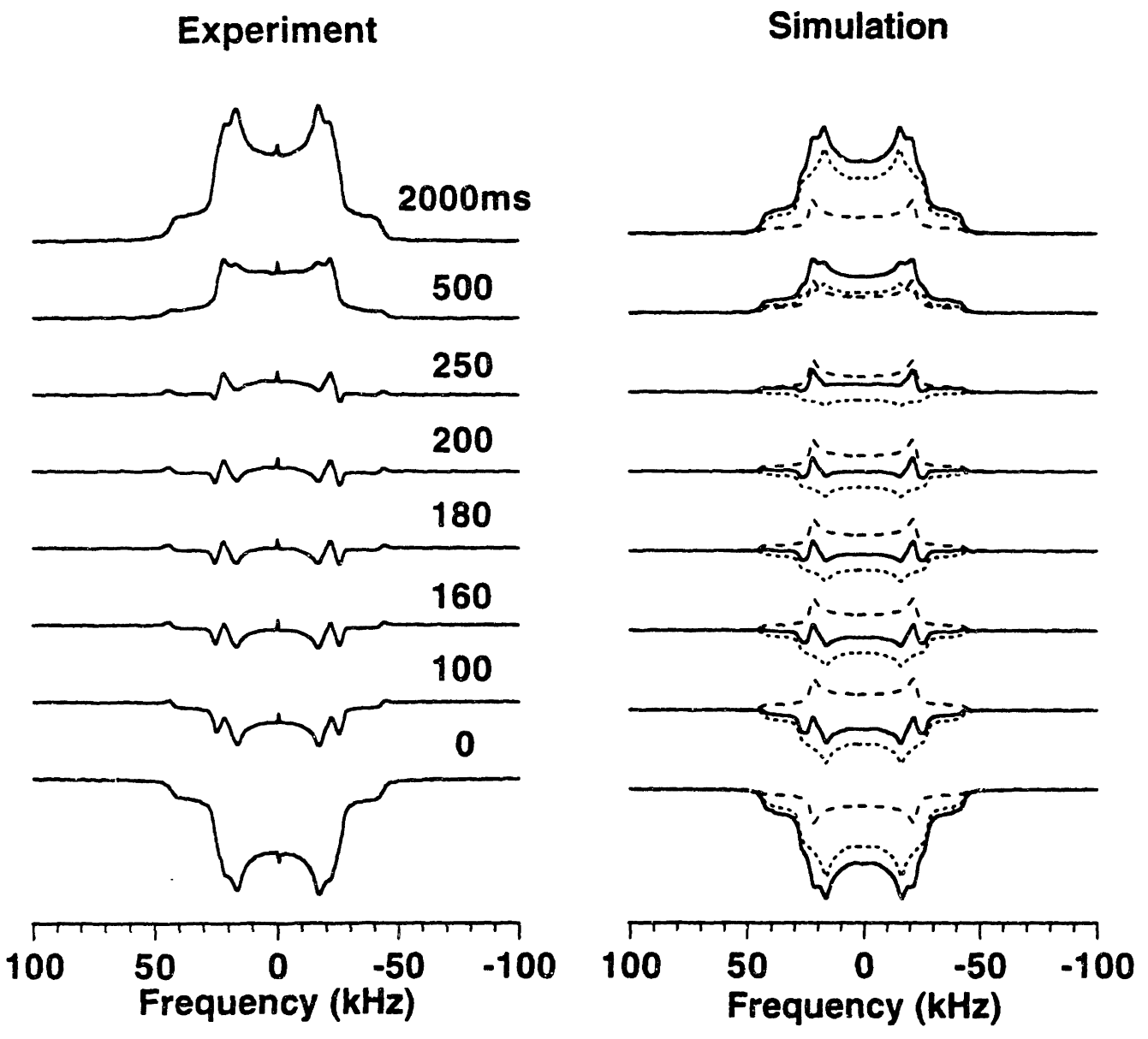
Experiment
Simulation
2000ms
500
250
200
180
160
100
0
100
50
0
-50
-100
Frequency (kHz)
100
50
0
-50
-100
Frequency (kHz)

The experimental and simulated spectra at several lower temperatures are shown in Figure 3-8. Features of interest include the attenuation of the axial component at -15°C as its hopping rate enters the intermediate exchange regime ($k \sim 10^6\ s^{-1}$), where quadrupole echo intensity losses are severe and the axial component therefore is invisible compared to the equatorial component. Less obvious but still significant is the fact that the average relaxation times are not monotonic. A lineshape in the motionally averaged fast limit and relaxation times on the order of several hundred ms corresponds to rates on the order of $10^{11}\ s^{-1}$. In that regime the relaxation time decreases with decreasing rate, and hence decreasing temperature. However, the average T_1 is 300 ms at 25°C, increasing to a maximum of 600 ms at -30°C, then decreasing to 500 ms at -45°C. This anomaly was too large to be ascribed to the sum of 3 methyls relaxing with a single time constant and one methyl relaxing with a different time constant, but can be understood by taking into consideration chemical exchange between axial and equatorial sites. Increased chemical exchange can effectively average the relaxation times of the two components. At 25°C, axial methyls with motional rate constants of $3.0 \times 10^7\ s^{-1}$ relax completely in a time of roughly 60 ms. Equatorial methyls, with motional rate constants of $2.4 \times 10^{11}\ s^{-1}$, have a relaxation time constant of approximately 600 ms, and are still inverted during the first several hundred ms. If the two methyl groups chemically exchange with a rate constant of $\sim 5\ s^{-1}$ or a time constant of ~200 ms, then the methyl group that is previously unrelaxed in an equatorial site, but is now in the axial site, may now relax in the next 60 ms, leading to apparent relaxation of both methyl populations. Through such chemical exchange, the apparent relaxation time of the intrinsically slowly relaxing equatorial component is shortened. This is an unusual situation where first, the two populations have significantly different relaxation time constants, and second, chemical exchange between the populations occurs with a time constant on the order of the longer of the two relaxation time constants. The ^2H NMR simulation program was modified to take into account specifically such chemical exchange dynamics which were used in the displayed simulations. The hopping

rates of the equatorial and axial methyl groups determined by ^{2}H and ^{13}C NMR simulations are plotted versus 1/T in Figure 3-9. The data were fit to the Arrhenius equation and yield an effective activation barrier of 10.9 ± 0.4 kJ/mol (26 ± 0.1 kcal/mol) for the equatorial methyl groups and 26.8 ± 1.7 kJ/mol (6.4 ± 0.4 kcal/mol) for the axial methyl group.

Figure 3-8. Experimental and simulated inversion-recovery ^{2}H NMR spectra of [WCp*(CD3)4][PF6] at the temperatures and the recovery times indicated. The axial methyl component is barely perceptible at -15°C and disappears at -30 and -45°C as it enters the intermediate exchange regime where quadrupole echo losses are severe. The equatorial component T_1 increases reaching a maximum of 600 ms at -30°C, then decreases at -45°C, indicating the increased effective relaxation induced by chemical exchange of the axial and equatorial methyl groups.

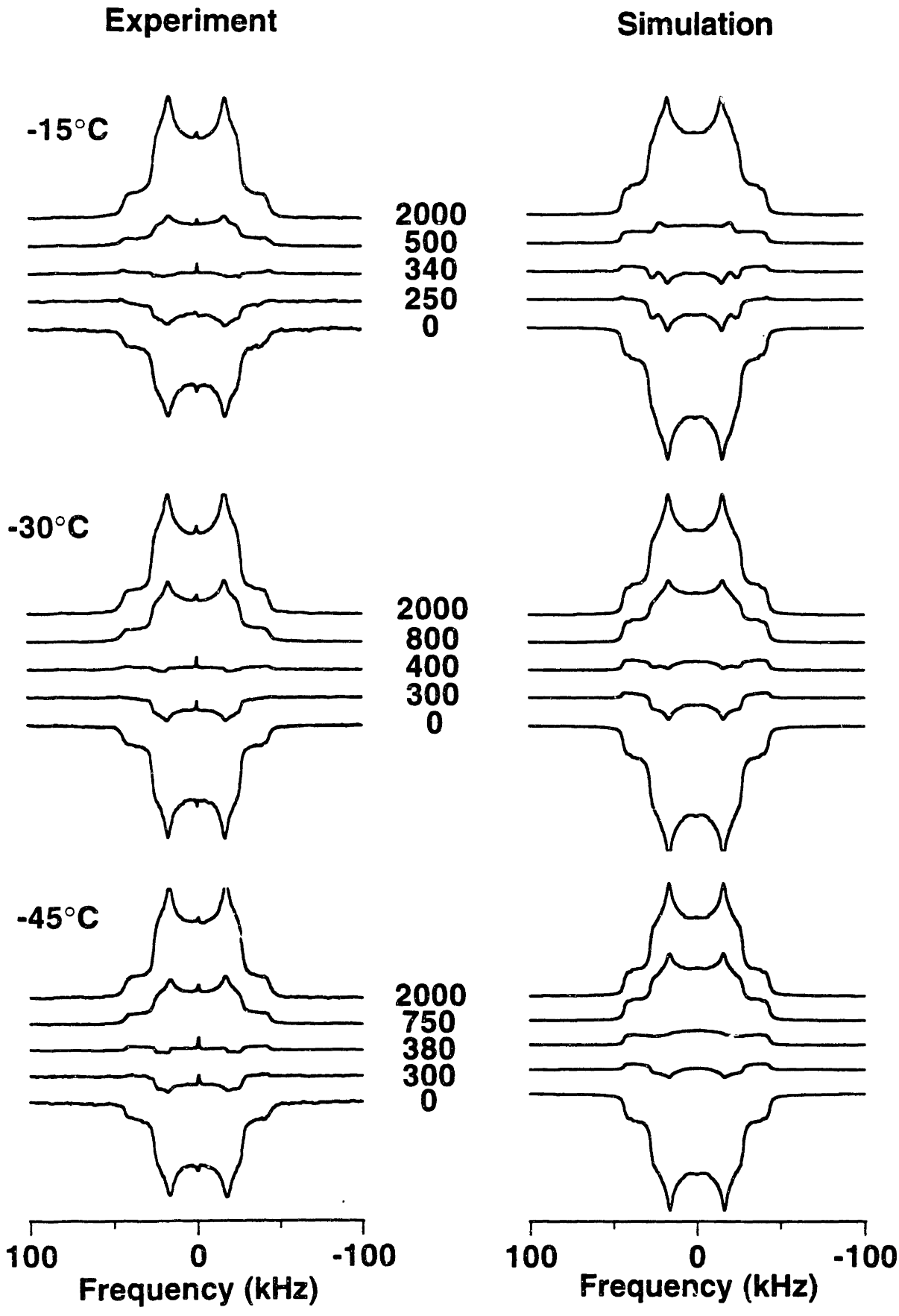
Experiment
Simulation
-15°C
2000
500
340
250
0
-30°C
2000
800
400
300
0
-45°C
2000
750
380
300
0
100
0
-100
Frequency (kHz)
100
0
-100
Frequency (kHz)

Figure 3-9. Arrhenius plot of hopping rates for the axial and equatorial methyls of [WCp*Me4][PF_6] based on the ^{13}C lineshape simulations and the ^{2}H relaxation simulations (Δ - equatorial ^{2}H simulations, O - axial ^{2}H simulations, + - axial ^{13}C simulations).

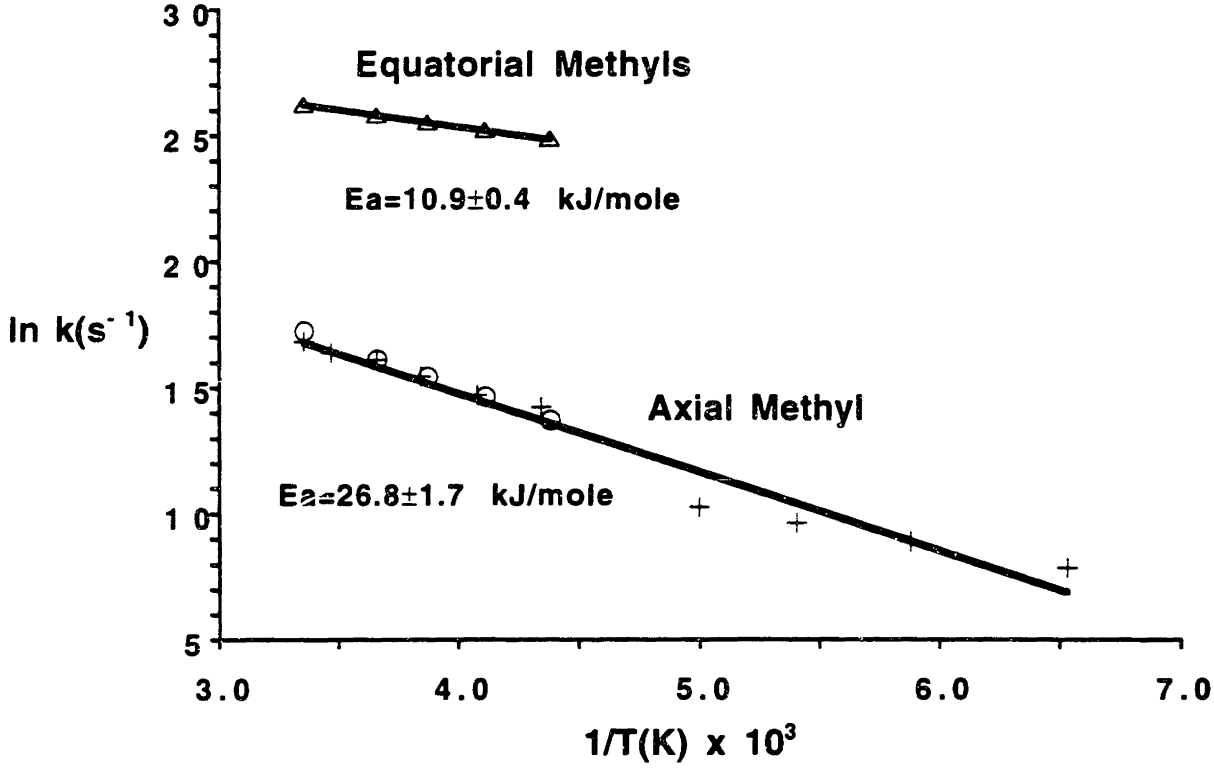
Equatorial Methyls
Ea=10.9±0.4 kJ/mole
Axial Methyl
Ea=26.8±1.7 kJ/mole
ln k(s⁻¹)
3 0
2 5
2 0
1 5
1 0
5
3.0
4.0
5.0
6.0
7.0
1/T(K) x 10³

3.2.3 X-Ray Structural Study

The original X-ray study of [W(η^5-C5Me5)Me4][PF6] confirmed that the overall geometry is trigonal bipyramidal with a PF_6^- ion widely separated from the metal.[5] However, both the Cp* ligand and the PF_6^- ion displayed a disorder that could not be resolved and bond lengths and angles of the core around the metal were unreliable. Disorder is not rare for Cp* complexes, and as in other cases, this problem was circumvented by substituting (η^5-C5Me4Et) for (η^5-C5Me5). The X-ray structure of [W(η^5-C5Me4Et)Me4][PF6], obtained by Professor Richard Schrock, Scott Seidel, and William Davis, is ordered and of high quality. Two molecules are found in the unit cell along with one molecule of dichloromethane. An ORTEP drawing of the cation of one molecule is shown in Figure 3-10 and bond distances and angles for the methyl groups bonded to Tungsten in both cations in Table 3-1. The structure of the cyclopentadienyl ligand is typical, including the dish shape in which the methyl and ethyl groups are forced up away from the WMe4 core - a point which implies an important corollary - that the equatorial methyl groups likely are equally stressed from above by these alkyl substituents on the cyclopentadienyl ring. Details of importance in the WMe4 core include the comparatively longer bond length to the axial methyl carbon (2.18 Å versus 2.12 Å for the equatorial methyls), which can be ascribed to steric repulsion. In addition, the C_{ax}-W-C_{eq} bond lengths are all near 77°, confirming the steric repulsion downward of the equatorial methyls induced by the substituents of the cyclopentadienyl ring. Regarding metal hydrogen interactions, the WMe4 core is nearly 3 fold symmetric, thus dashing the likelihood of equatorial agostic interactions. The only deviation is a marginally smaller value for one of the C_{eq}-W-C_{eq} bond angles, which can be explained by the observation that this is the only angle with only one cyclopentadienyl substituent projecting between the equatorial methyl groups. The X-ray study is of sufficiently high quality to conclude that at least in terms of the WMe4 core there is no compelling evidence for any interaction between the metal and a CH bond in either an equatorial methyl group or the axial methyl group in

$[W(\eta 5\text{-}C_5Me_4Et)Me_4]^+$. Assuming that the structure of a (η^5-C_5Me_5) complex is practically identical to the structure of a η^5-C_5Me_4Et complex, then any such interaction in $[W(\eta 5\text{-}C_5Me5)Me_4][PF_6]$ in the solid state is also unlikely.

Figure 3-10. An ORTEP drawing of $[W(\eta^5\text{-}C_5Me_4Et)Me_4]^+$ (molecule 1)

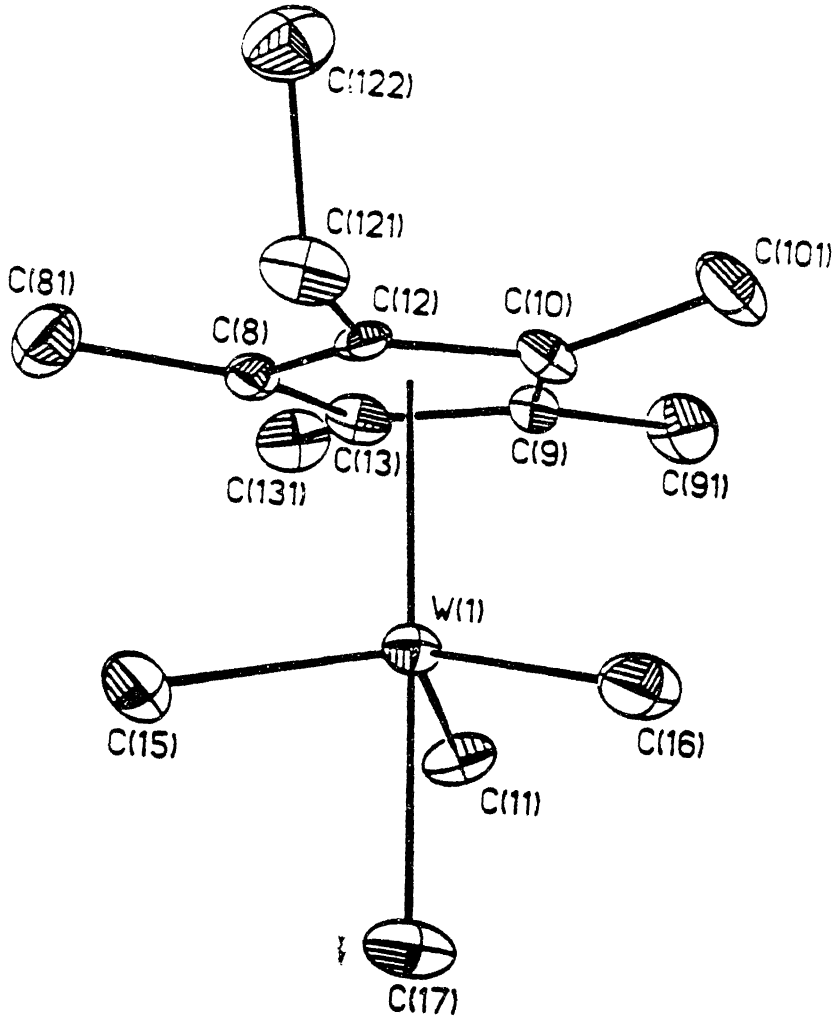
C(122)
C(121)
C(101)
C(81)
C(12)
C(10)
C(8)
C(13)
C(9)
C(131)
C(91)
W(1)
C(15)
C(16)
C(11)
C(17)

Table 3-1. Selected Bond Distances (Å) and Angles (deg) for the W-Methyl Groups in $[W(\eta^5\text{-}C_5Me_4Et)Me_4][PF_6]$

Distances (Å)

	Molecule 1	Molecule 2
W-C(11)	2.132(11)	2.143(11)
W-C(15)	2.114(11)	2.114(11)
W-C(16)	2.122(11)	2.122(10)
W-C(17)	2.182(11)	2.182(10)

Angles (°)

	Molecule 1	Molecule 2
C(15)-W-C(11)	117.0(5)	115.5(5)
C(15)-W-C(16)	111.4(5)	112.9(5)
C(16)-W-C(11)	116.9(5)	116.5(5)
C(17)-W-C(16)	77.7(5)	77.0(4)
C(17)-W-C(11)	75.8(5)	76.4(5)
C(17)-W-C(15)	77.6(5)	77.1(4)

3.2.4 Conclusions

The temperature-dependent broadening of the *axial* methyl ^{13}C line in trigonal-bipyramidal [WCp*Me4][PF6] is due to unusually slow hopping (E_a=26.8 ± 1.7 kJ/mol or 6.4 ± 0.4 kcal/mol) between the three hydrogen sites, a process that proceeds on the same time scale as the CW ^{1}H decoupling periodicity. The motionally averaged line shapes for the equatorial methyl groups in [WCp*Me4][PF6] were significantly asymmetric, a behavior wholly unexpected for fast limit motion. The hopping rate in the equatorial methyl groups was determined by ^{2}H T_1 inversion-recovery measurements to be 10.9 ± 0.4 kJ/mol (2.6 ± 0.1 kcal/mol).

The hypotheses of agostic interactions in this compound are apparently unfounded, as there is no low energy (2300-2800 cm^{-1} versus 2900-3000 cm^{-1}) IR band indicative of agostic interactions and the X-ray study shows no compelling evidence of agostic interactions. However, one might also propose there are other reasons for temperature dependent IPR chemical shifts of the magnitude observed in $[W(\eta5\text{-}C_5Me_4Et)Me_4]^+$. For example, on the basis of the explanation of the asymmetry of the ^{2}H lineshape as due to distortion of equatorial methyl geometry, it is plausible that the observed small IPR effect in the equatorial methyl groups may be related to such a geometric distortion. In this matter, it would be interesting to determine if the octatrienylideneimines, discussed above as having asymmetric ^{2}H lineshapes due to geometrical bond-angle distortions, would also exhibit an IPR effect.

3.3 Tantalum

This study was undertaken to determine what similarities existed between the methyl dynamics of $[WCp^*Me_4]^+$, discussed in the previous section, and $[TaCp_2Me_2]^+$ in that hopes that dynamic details may shed light upon the structure and possible existence of α-agostic interactions in this class of organometallic compounds. While no direct

evidence was found regarding α-agostic interactions, some unusual dynamic details were obtained.

3.3.1 Introduction

Both Magic Angle Spinning (MAS) ^{13}C and static(non-spinning) ^{2}H NMR spectra were examined. In each case, the compound was labelled on both methyls. Preliminary analysis of the ^{2}H NMR spectra as a function of temperature indicated that a phase transition occurred at approximately -30 - -35 °C, which was subsequently confirmed by differential scanning calorimetry (by Scott Seidel of Professor Richard Schrock's research group). At all temperatures the methyls were equivalent/indistinguishable. Below the phase transition temperature they exhibited ^{2}H lineshapes typical of fast limit methyl hopping motion ($k > 10^{8}\ s^{-1}$). Above the phase transition, the lineshape is further narrowed by a factor of 2, indicative of an additional large amplitude, fast ($k > 10^{6}\ s^{-1}$) motion. This additional narrowing could be simulated by exchange of hydrogens between the two methyl groups at such a rate, if the C-Ta-C angle was 90 ± 3° (^{2}H NMR is not able to determine whether this exchange is *of entire* methyl groups, including *carbons*, or exchange of one or more hydrogens *between* the methyl groups). The geometry of this motion was intriguing, since such an angle was in contrast to the expected angle of 109.5° for a tetrahedral complex of coordination number 4. However, the subtle distinction of the possibility of hydrogen exchange *between* methyl groups was even more intriguing since this could illuminate details of an α-agostic interaction. For this reason, ^{13}C MAS spectra as a function of temperature were examined. An unusual effect - motion and sample spinning occurring on the same time-scale[16] leads to linewidth broadening at low temperature and provides information regarding the rate of exchange *of* the methyl *carbons*. The results of this study indicated that the carbons exchanged with rates in congruence with the hydrogen exchange in the aforementioned ^{2}H NMR study, indicating that the dynamics

of this system can be completely accounted for simply by the exchange of the *entire* methyl groups at rates above 10^6 s^{-1}.

3.3.2 Static ^2H NMR

Sample Preparation. $[TaCp_2(CD_3)_2][PF_6]$ was generously synthesized and provided by Scott Seidel of Professor Richard Schrock's research group.

^2H NMR Measurements. Static(non MAS) ^2H spectra of $[TaCp_2(CD_3)_2][PF_6]$ were obtained on a custom built spectrometer with a 9.4T magnet, corresponding to a deuterium resonance frequency of 61 MHz. Typically, spectra were observed using a quadrupole echo pulse sequence with ^2H 90° pulse lengths of 2 μs and echo times of 30 μs. The sampling rate was 1 MHz.

^2H NMR Simulations. Deuterium NMR simulations were performed using a program described elsewhere.[11] Input parameters include the motional model (rates and geometries) and quadrupole coupling parameters. Using a given motional model, the program calculates the powder average of the motion dependent lineshape.

^2H NMR Lineshapes of $[TaCp_2Me_2][PF_6]$. The observed experimental quadrupole echo spectra are shown in figure 3-11 at a series of temperatures. At 25 °C the spectrum is unusual since the width of the Pake pattern is narrowed by a factor of ~2 over the expected fast-limit methyl spectrum ($k > 10^8$ s^{-1}), which is clearly exhibited at -58 °C. This is a factor of ~6 in total over the expected rigid lattice spectrum. Such extreme narrowing is indicative of fast ($k > 10^6$ s^{-1}) large amplitude motion in addition to the fast-limit methyl hopping. In fact, this composite motion can be simulated, as shown in figure 3-12, by assuming that the deuterons exchange between the two methyl groups at a rate greater than 10^6 s^{-1}, and provided that the C-Ta-C angle is near 90 ° ± 4 °. In addition, the effective motionally averaged quadrupole coupling constant eQV_0/h must be adjusted from 170 kHz to 140 kHz. Simulations using these parameters fit the observed spectrum well. A further unusual feature appears in the -36 °C spectrum, where both an extremely

narrowed lineshape and a typical methyl fast limit lineshape are observed concurrently. This indicates that the rate of exchange between the methyl groups does not smoothly decrease as the temperature is lowered, but rather that two different species are present, one with methyl exchange greater than 10^6 s^{-1} and one with exchange at 10^3 s^{-1} if at all. The proportion of these species is show to change with lower temperature. This suggests that two phases of the material are present in some sort of equilibrium during a phase transition. Finally, as a footnote to the details described for the Tungsten compound, the low temperature typical fast limit spectrum exhibited at -58 °C also displays a lineshape asymmetry. This feature can be simulated readily with the techniques previously described using a geometric distortion of ϕ=2 °. This lineshape asymmetry, having appeared in the spectra of both organometallic compounds, portends that such asymmetry may be common in charged organometallics. Further study is needed to resolve its details. Still, using the aforementioned parameters, the -38 °C lineshape with both the typical fast limit and extremely narrowed components may be simulated readily as shown in figure 3-13.

Figure 3-11 shows the experimental ^{2}H NMR spectra at the relevant temperatures. Note at -58°C, the breadth and shape typical of methyl groups in the fast limit ($k > 10^{8}\ s^{-1}$). Next note at 25°C, the shape is maintained, whereas the width is halved. This is indicative of additional large amplitude, fast ($k > 10^{6}\ s^{-1}$) motion. The lineshape produced by this addition motion is quite sensitive to the geometry of the motion and indicates a C-Ta-C angle of 90° ± 3°. Finally note that at -36°C, both lineshapes are present, indicating that two species, one with and one without the additional exchange, are present.

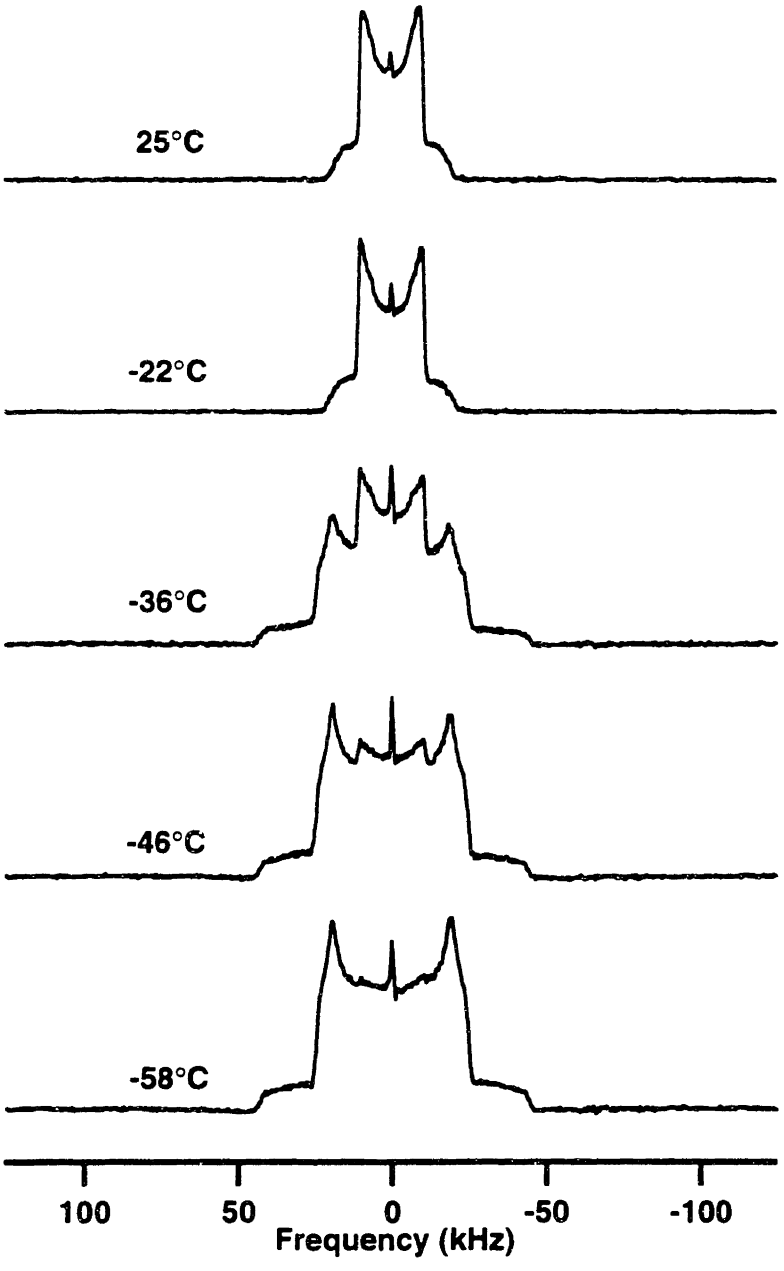
25°C
-22°C
-36°C
-46°C
-58°C
100
50
0
-50
-100
Frequency (kHz)

Figure 3-12 shows the room temperature experimental ^{2}H NMR spectrum and a simulation. The composite motion simulation details and rates are given on the figure.

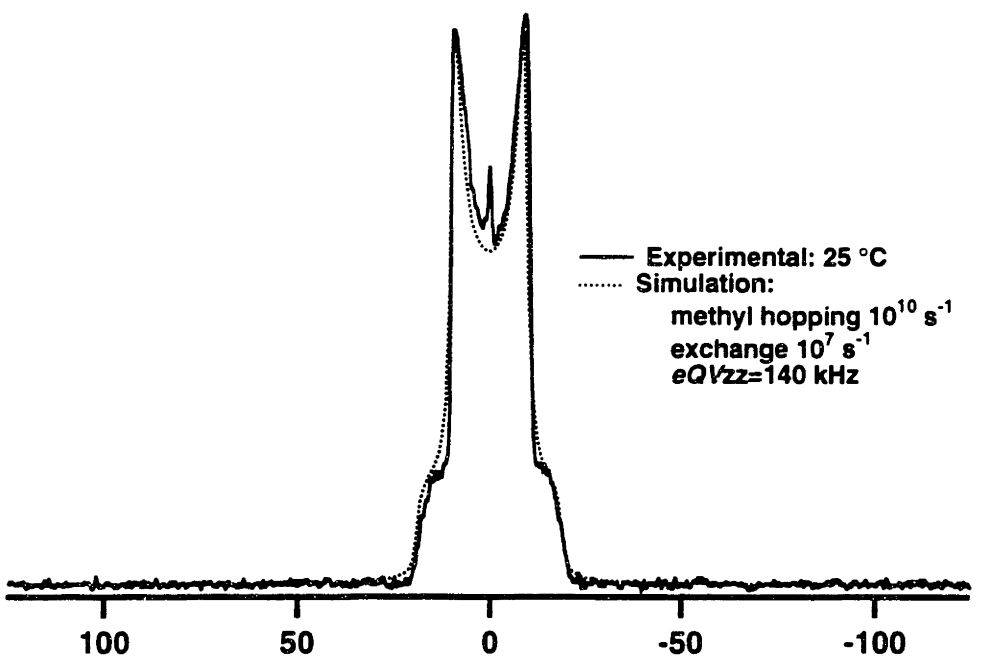
Experimental: 25 °C
Simulation:
methyl hopping 10^{10} s^{-1}
exchange 10^{7} s^{-1}
eQVzz=140 kHz
100
50
0
-50
-100

Figure 3-13 shows the experimental and simulated ^{2}H NMR spectrum near the phase transition temperature(-36°C), showing both the typical fast limit methyl lineshape as well as the extremely narrowed lineshape. The simulation details and rates are given on the figure.

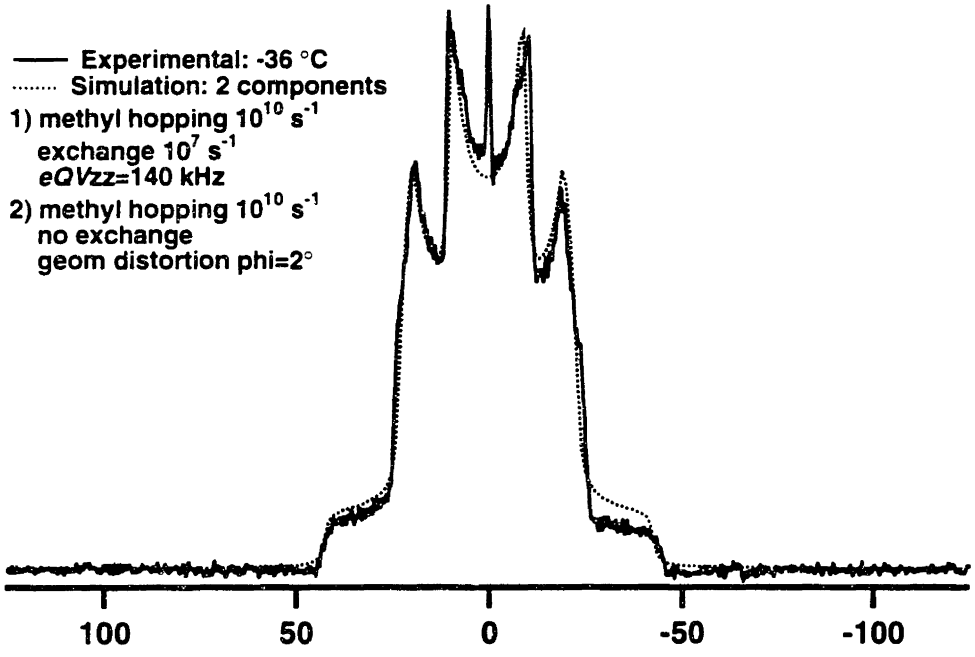
Experimental: -36 °C
Simulation: 2 components
1) methyl hopping 10^{10} s^{-1}
exchange 10^{7} s^{-1}
eQVzz=140 kHz
2) methyl hopping 10^{10} s^{-1}
no exchange
geom distortion phi=2°
100
50
0
-50
-100

3.3.3 Differential Scanning Calorimetry

Based on the data from the ^2H NMR which suggested the compound undergoes a phase transition at approximately -30 °C, Differential Scanning Calorimetry was employed on this compound (by Scott Seidel). Indeed, a discontinuity was found in the heat capacity of the compound, shown in figure 3-14 (courtesy Scott Seidel), indicating a phase transition at -30 °C. This discovery stands as a remarkable confirmation of the value of rate calculations obtainable from ^2H NMR.

Figure 3-14 shows the differential scanning calorimetry results for [$TaCp_2Me_2$]. The absorbance at -30 °C is indicative of a phase transition occurring at this temperature. This result is in agreement with the deuterium data, indicating that two phases exist in which the methyl hopping rate is markedly different.

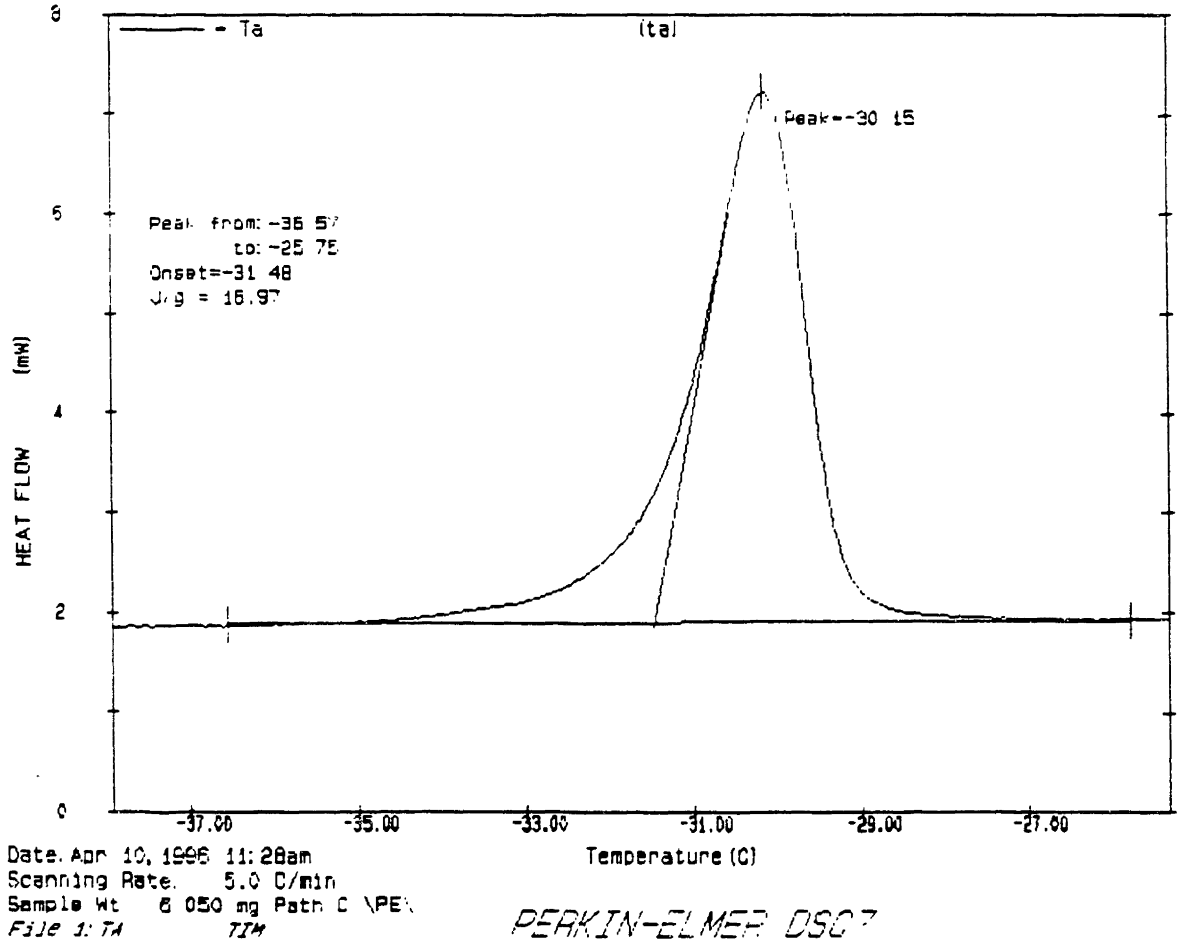
Ta
(tal
Peak=-30 15
Peak from: -36 57
to: -25 75
Onset=-31 48
J/g = 16.97
HEAT FLOW (mW)
8
6
4
2
0
-37.00
-35.00
-33.00
-31.00
-29.00
-27.00
Temperature (C)
Date. Apr 10, 1996 11:28am
Scanning Rate. 5.0 C/min
Sample Wt 6 050 mg Path C \PE\
File 1: TA TIM
PERKIN-ELMER DSC 7

3.3.4 MAS ^{13}C NMR

The possibility that the deuterons exchanged between the two methyl groups unearthed the possibility that they exchanged not as *whole* methyl groups, but rather an agostic interaction permitted the *migration* of deuterons *between* the methyl groups. Further details could not be gleaned from the ^{2}H NMR, and so a solid state MAS ^{13}C study was initiated. in the hopes that the two methyl carbons, which would necessarily be equivalent in a canonical tetrahedral complex as a result of symmetry constraints, might be inequivalent due to such an agostic interaction. Such inequivalency while not likely observable at 25 °C due to rapid motion, might be observable at lower temperatures. The experimental MAS ^{13}C spectra at several temperatures is shown in figure 3-15. At first glance, the results are puzzling. As expected, at 25 °C there is but only resonance (with its associated spinning sidebands), and at those temperatures below -30 °C, there still is only one resonance but all lines in the spinning sideband pattern are significantly broadened. The sideband pattern at these lower temperatures is wider (~15 kHz compared to only ~6 kHz at 25 °C) which was anticipated since motion would be likely to average the chemical shift anisotropy (in the same way it averages the ^{2}H powder pattern). The spectra can be explained however. The understanding relies once again on an interference effect. In this case, the interference results from the periodicity of the magic angle spinning being on the same time scale as methyl ^{13}C exchange.[16] Simulations can reproduce this effect. Figure 3-16 shows the broadening and sideband (CSA) narrowing that results from this interference effect by displaying the simulated spectra as a function of motional rate. The spinning speed used was 3.0 kHz(~2×10^4 rad/s), and the linewidth broadening is shown to be most severe at rates around 10^4 s^{-1}. Precise reproduction of the broadening and the sideband patterns depends on the geometry used for the motion relative to the chemical shift tensor principal axis system. The C-Ta-C angle is assumed to be 90° from the ^{2}H NMR study. Figure 3-17 shows the effect of considering different CSA PAS orientations at a spinning speed of 3.4 kHz and motional rates of 3×10^6 s^{-1}. The angles shown represent

the Euler Angles to rotate the PAS of one carbon to the PAS of the second carbon. The best fit to the experimental spectra is found with Euler angles of (0, 90, 0) or a rotation of 90° about the y axis. This would served to average the x and z chemical shift principal values. Thus, the least shielded component (6.2 kHz = +20 ppm relative to the isotrope) is perpendicular to the C-Ta-C plane. This is another demonstration of the information regarding rates and structure that can be gleaned from NMR data. A comparison of the experimental and simulated spectra using the aforementioned parameters is shown in figure 3-18.

Figure 3-15 shows the experimental spectra at the indicated temperatures and spinning speeds, namely 25°C/3.0 kHz, -40°C/3.2 kHz, -70°C/2.8 kHz, -80°C/1.6 kHz. Note the broadening of the isotropic line and sidebands at the temperatures below the phase transition. Also note the breadth of the sideband envelope is small at room temperature and much larger at the lower temperatures, indicating motional averaging of the chemical shift anisotropy(CSA).

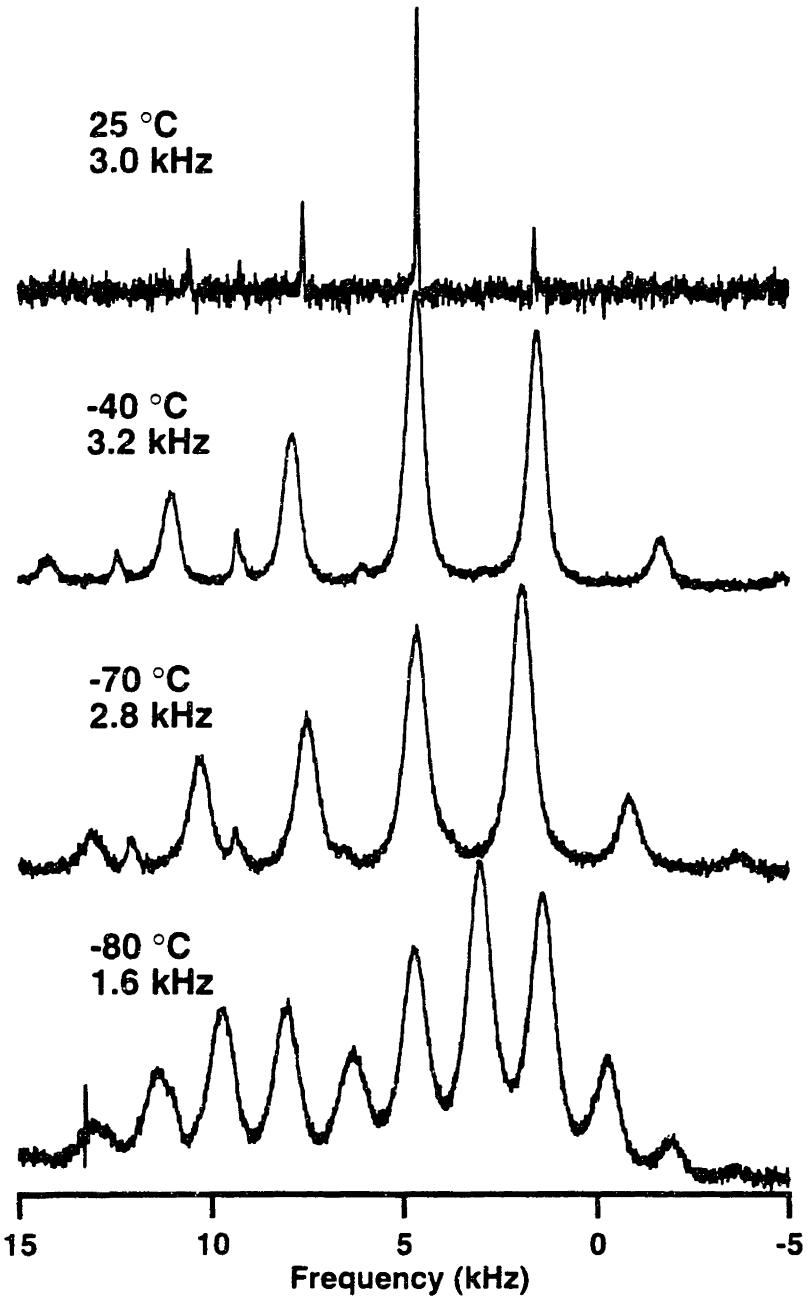
25 °C
3.0 kHz
-40 °C
3.2 kHz
-70 °C
2.8 kHz
-80 °C
1.6 kHz
15
10
5
0
-5
Frequency (kHz)

Figure 3-16 shows simulations delineating the interference effect due to methyl exchange motion and Magic Angle Spinning occurring on the same time scale - namely ~10^4 s^{-1} / rad/s. The simulations show the dependence of the broadening as a function of the exchange rate. The chemical shift anisotropy (CSA) used was δ=-8.3 kHz (@ 317 MHz = -26 ppm) and η =0.5 as determined by fitting the sideband patterns at -70 and -40 °C. The principal values are thus (σ_{xx}, σ_{yy}, σ_{zz}) = (2.075, 6.225, -8.3)(kHz) relative to the isotrope. The geometry of motion used corresponded to Euler angles (0,90,0) which translates into the interchange (averaging) of the x and z principal axes of the CSA tensor. The rates are as given on the figure.

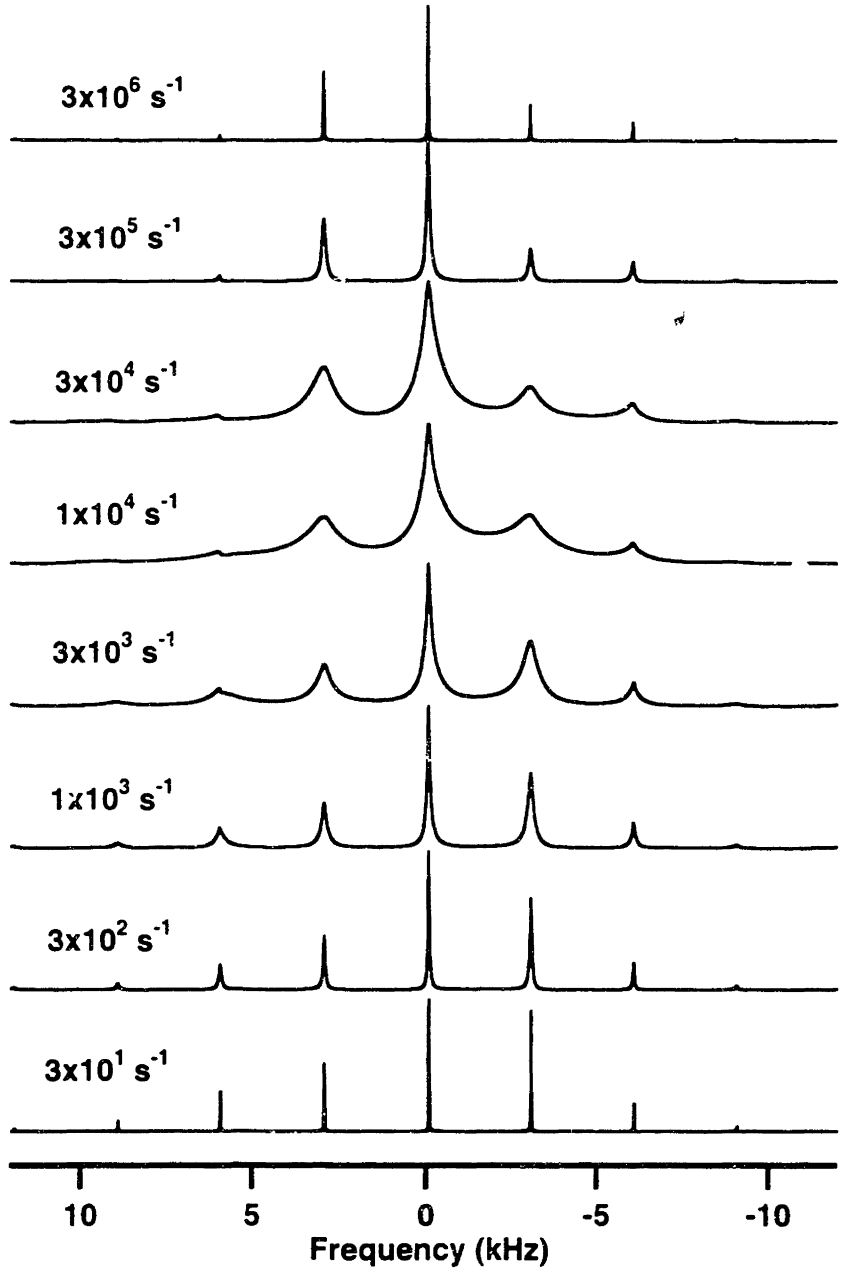
3x10^6 s^-1
3x10^5 s^-1
3x10^4 s^-1
1x10^4 s^-1
3x10^3 s^-1
1x10^3 s^-1
3x10^2 s^-1
3x10^1 s^-1
10
5
0
-5
-10
Frequency (kHz)

Figure 3-17 shows the effect of choices of different geometries of motion. At the bottom is the MAS spectrum without methyl exchange motion. The next spectrum shows the effect of exchange motion which averages the x and y principal values. Since these two are the closest in value, the effect is very slight (=> (4.15, 4.15, -8.3) (kHz)). The next spectrum shows the effect of averaging the x and z principal values (=> (-3.1, 6.2, -3.1)). This narrows the sideband amplitude envelope considerably but not completely. The final (top) spectrum shows the effect of averaging the y and z principal values, which results in an extremely narrowed spectrum, since these two principal values are those furthest from the isotrope, yielding an average value near the isotrope (=> (2.08, -1.04, -1.04)).

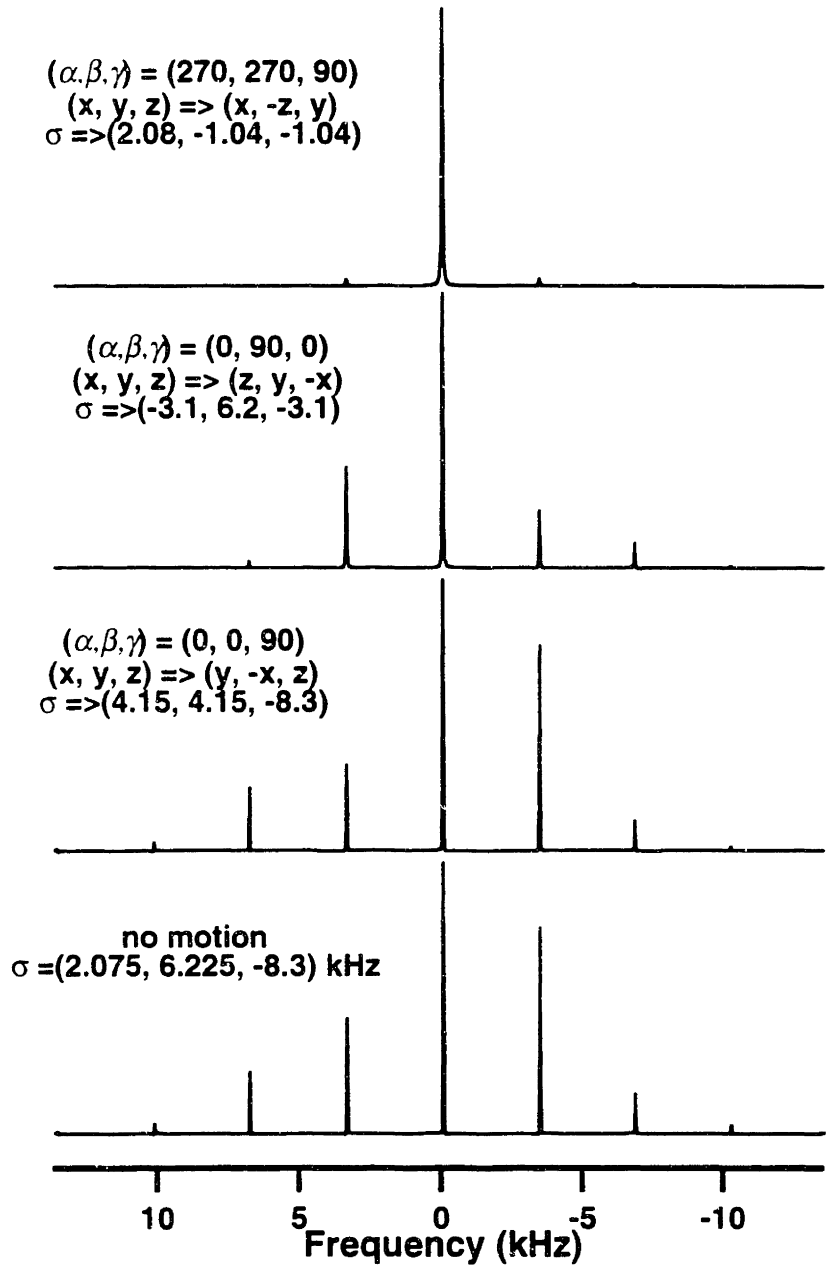
(α,β,γ) = (270, 270, 90)
(x, y, z) => (x, -z, y)
σ =>(2.08, -1.04, -1.04)
(α,β,γ) = (0, 90, 0)
(x, y, z) => (z, y, -x)
σ =>(-3.1, 6.2, -3.1)
(α,β,γ) = (0, 0, 90)
(x, y, z) => (y, -x, z)
σ =>(4.15, 4.15, -8.3)
no motion
σ =(2.075, 6.225, -8.3) kHz
10
5
0
-5
-10
Frequency (kHz)

Figure 3-18 shows the experimental and simulated spectra, where the only adjustable parameter was the rate of methyl carbon exchange. Note that the spinning sideband pattern is well reproduced at all temperatures, especially 25°C where motional averaging narrows the CSA. Note also that linewidths are reproduced well in those spectra at temperatures below the phase transition, a feature calculated based on a model of interference between the Magic Angle Spinning and the methyl exchange motion.

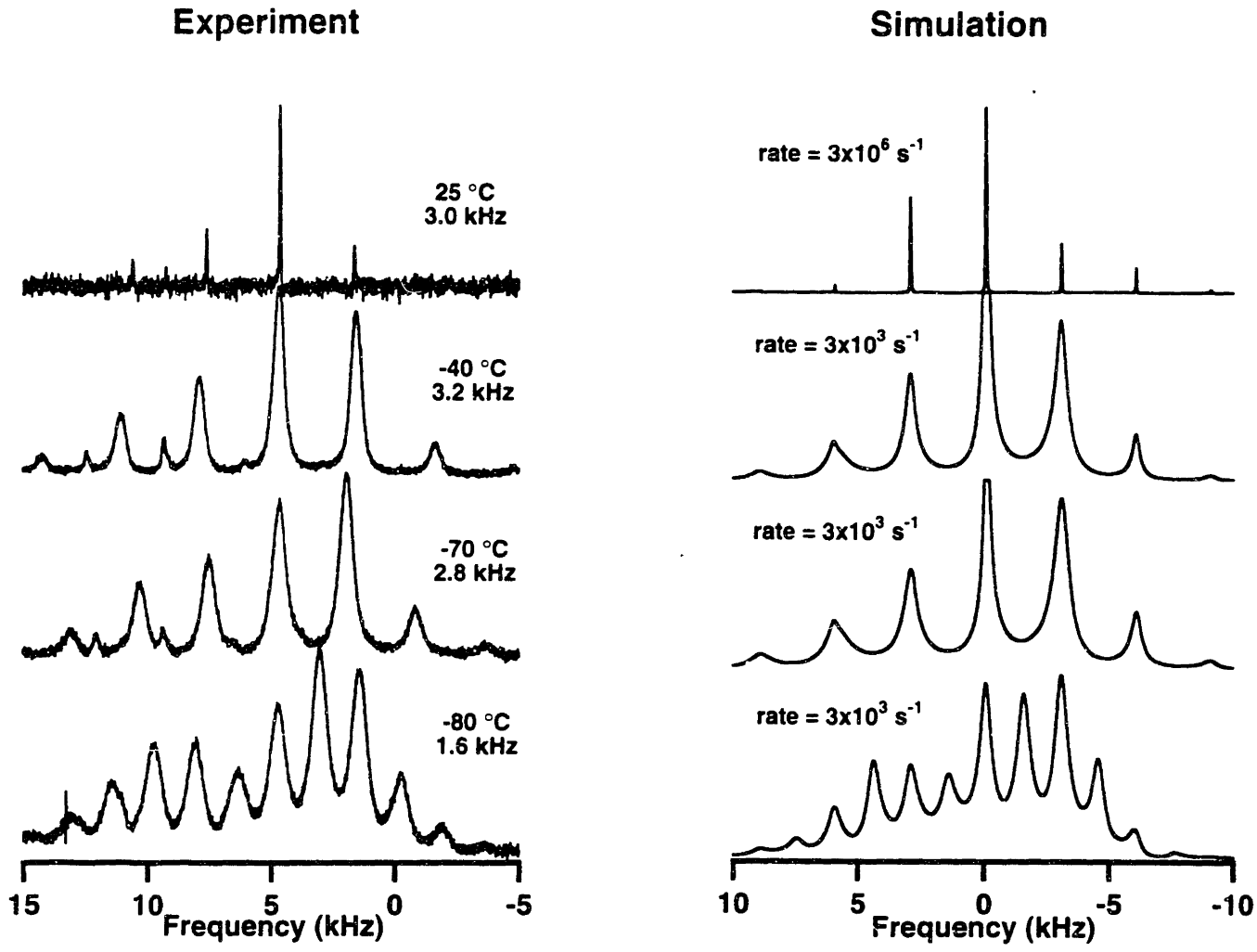
Experiment
25 °C
3.0 kHz
-40 °C
3.2 kHz
-70 °C
2.8 kHz
-80 °C
1.6 kHz
15
10
5
0
-5
Frequency (kHz)
Simulation
rate = 3x10^6 s^-1
rate = 3x10^3 s^-1
rate = 3x10^3 s^-1
rate = 3x10^3 s^-1
10
5
0
-5
-10
Frequency (kHz)

3.3.4 Conclusions

Regarding the quantitative results obtained on this compound, the NMR data indicate that the internal (hopping) methyl dynamics of $[TaCp_2Me_2]^+$ can be modeled over the entire temperature range 25 to -80 °C as both methyls hopping with the *same* fast limit ($k \sim 10^{10}\ s^{-1}$) rate. In the phase which is stable below -30°C, the entire methyls (carbons included) exchange with a rate of approximately $10^3\ s^{-1}$ while in the phase stable above -30°C, this rate is increased to approximately $10^6\ s^{-1}$. There is no NMR dynamics evidence which indicates that the two methyls have different internal hopping rates at any temperatures examined (in contrast to the differential dynamics exhibited by the equatorial and axial methyls in $[WCp^*Me_4]^+$). In sum, there is thus no NMR evidence of an α-agostic interaction in this compound.

3.4 Conclusions

This chapter has demonstrated the analysis of the NMR data of $[WCp^*Me_4]^+$ and $[TaCp_2Me_2]^+$. The data were shown to include several anomalous but explainable effects, including ^2H lineshape asymmetry under motional averaging, ^{13}C linebroadening from interference of motion and ^1H decoupling, extreme narrowing of ^2H spectra to one-sixth the rigid lattice breadth by composite motion, and broadening of MAS lines from interference between spinning time scales and motional rates. The wealth of data from the quantitative analysis of this effects demonstrates the extraordinary power of motional dynamics investigation by NMR.

References

1. M. Brookhart, M. L. H. Green, L.-L. Wong, *Prog. Inorg. Chem.* **36**, 1-124 (1988).
2. R. R. Schrock, in *Reactions of Coordinated Ligands* P. R. Braterman, Eds. (Plenum, New York, 1986).
3. V. Copie, Ph.D. Thesis, Massachusetts Institute of Technology (1990).
4. D. C. Maus, V. Copie, B. Sun, J. M. Griffiths, R. G. Griffin, S. Luo, R. R. Schrock, A. H. Liu, S. W. Seidel, W. M. Davis, A. Grohmann, *J. Am. Chem. Soc.* **118**, 5665-5671 (1996).
5. A. H. Liu, R. C. Murray, J. C. Dewan, B. D. Santarsiero, R. R. Schrock, *J. Am. Chem. Soc.* **109**, 4282-4291 (1987).
6. M. L. H. Green, A. K. Hughes, N. A. Popham, A. H. H. Stephens, L.-L. Wong, *J. Chem. Soc., Dalton Trans.* , 3077-3082 (1992).
7. A. Bielecki, D. P. Burum, *J. Mag. Res. Ser. A* **116**, 215-220 (1995).
8. J. R. Long, B. Q. Sun, A. Bowen, R. G. Griffin, *J. Am. Chem. Soc.* **116**, 11950-11956 (1994).
9. W. P. Rothwell, J. S. Waugh, *J. Chem. Phys.* **74**, 2721-2732 (1981).
10. J. Herzfeld, A. E. Berger, *J. Chem. Phys.* **73**, 6021-6030 (1980).
11. R. J. Wittebort, E. T. Olejniczak, R. G. Griffin, *J. Chem. Phys.* **86**, 5411-5420 (1987).
12. Y. Hiyama, S. Roy, K. Guo, L. G. Butler, D. Torchia, *J. Am. Chem. Soc.* **109**, 2525-2526 (1987).
13. G. L. Hoatson, R. L. Vold, T. Y. Tse, *J. Chem. Phys.* **100**, 4756-4765 (1994).
14. M.-H. Wann, G. S. Harbison, *J. Chem. Phys.* **101**, 231-237 (1994).
15. D. A. Torchia, A. Szabo, *J. Magn. Reson.* **64**, 135-141 (1985).
16. A. Schmidt, S. O. Smith, D. P. Raleigh, J. E. Roberts, R. G. Griffin, S. Vega, *J. Chem. Phys.* **85**, 4248-4253 (1986).

4. Spin Dynamics

4.1 Introduction

The previous chapters have treated the time dependencies as being due to spatial motion and the effects being seen mainly in the resonance frequencies of the spins. This chapter introduces a framework more suitable for the subsequent chapters. This perspective is more quantum mechanical in nature: that of viewing the dynamics of the wave-functions, coherences and populations. The subsequent chapters both relate investigations in which polarization transfer plays the central role. This chapter introduces both thermodynamic and coherent formalisms for describing such polarization transfers. The first simple example is the thermodynamic description of Cross-Polarization(CP). The next two examples are both coherently driven: Rotational Resonance(R^2) and Radio frequency-driven Dipolar Recoupling(RFDR).

4.2 Cross Polarization: Thermodynamics

The technique known as Cross Polarization[1] relies upon a thermodynamic analysis, especially the concept of Spin Temperature. The equilibrium magnetization magnitude of a sample is found to depend on the gyromagnetic ratio γ, magnetic field B, and temperature T in the following way

$$M = \frac{c\gamma^2 B}{T} \qquad \text{(Curie Law)}$$

where c represents other constants. When the magnetization is perturbed, such as by an RF pulse, the system can be thought of as attaining a new spin temperature

$$T = \frac{c\gamma^2 B}{M}$$

In Cross Polarization, there are two types of spins - abundant high gyromagnetic ratio I spins which are strongly dipole coupled to dilute low gyromagnetic ratio S spins. Cross Polarization aims to increase the magnetization of the S spins in the following way. The I spins are first irradiated with a $\pi/2$ pulse and then spin locked by continuous irradiation of field strength B_1 such that the magnetization is held in the transverse plane. If this is done

quickly with strong RF pulses, the spin locked magnetization is equal in magnitude to the equilibrium longitudinal magnetization

$$M_{SL}^{I} = M_{eq}^{I}$$

$$T_{SL}^{I} = \frac{B_1^I}{B_0} T_0$$

During the spin lock on the I spins, the S spins are spin locked in the transverse plane as well. In fact, the strengths of the spin lock fields B_1 are arranged to fulfill a specific criterion, that of the Hartmann-Hahn match.

$$\gamma_I B_1^I = \gamma_S B_1^S$$

At this condition, the two types of spins, I and S, are essentially brought into thermal contact and may exchange polarization so that their spin temperatures equalize

$$T_{SL}^{I} = T_{SL}^{S}$$

The implication of this arrangement is this:

$$M_{SL}^{S} = \frac{c\gamma_S^2 B_1^S}{T_{SL}^S}$$

$$= \frac{c\gamma_S^2 B_1^S}{T_{SL}^I}$$

$$= \frac{c\gamma_S^2 B_1^S}{\left(\frac{B_1^I T_0}{B_0}\right)}$$

employing the Hartmann-Hahn condition

$$M_{SL}^{S} = \frac{c\gamma_S \gamma_I B_0}{T_0}$$

and thus,

$$M_{SL}^{S} = M_{eq}^{S} \frac{\gamma_I}{\gamma_S}$$

That is, the magnitude of the S spin magnetization in the spin lock plane is enhanced over its equilibrium longitudinal value by the ratio $\frac{\gamma_I}{\gamma_S}$, which is ~4 for I=^{1}H and S=^{13}C.

4.3 Mathematical Description of Coherent Dynamics

While a thermodynamic perspective is appropriate for Cross Polarization, the microscopic details which ensue during coherently driven spin dynamics require a quantum mechanical formalism.[2] Magnetic Resonance spin systems, just as any other quantum system follow time dependence in the wave function ψ, prescribed by the Schrodinger equation

$$\hat{H}\psi = E\psi$$

A quantum formalism which is more convenient than the traditional use of wave functions is that of the density operator, $\rho = \psi^* \psi$, since observables may be calculated as the trace of the observable operator multiplied by the density operator.

$$A = Tr(\hat{\mathbf{A}}\rho)$$

The density operator then follows time evolution prescribed by the Liouville von-Neumann equation

$$\frac{\partial \rho(t)}{\partial t} = i\left[\rho(t), \hat{H}(t)\right]$$

whose formal solution is

$$\rho(t) = e^{-i\int^{t} d\tau \hat{H}(\tau)} \rho(0) e^{i\int^{t} d\tau \hat{H}(\tau)}$$

While cumbersome at first glance, this description has been found to be quite useful in practice. The Hamiltonian may often be well approximated as piecewise constant, and thus the density operator may be numerically calculated as

$$\rho(t) = e^{-iH|_{t_k}\Delta t_k} \ldots e^{-iH|_{t_1}\Delta t_1} \rho(0) e^{iH|_{t_1}\Delta t_1} \ldots e^{iH|_{t_k}\Delta t_k}$$

4.4 Rotational Resonance

As mentioned in the chapter on spatial dynamics, MAS averages dipole couplings.[3] For solid samples, MAS is crucial for obtaining the requisite spectral resolution for meaningful distinction of chemical species, yet this additional effect of MAS hampers efforts to measure the couplings between these chemical species. The preceding chapters also described several situations in which two dynamics processes on similar time scales interfere with each other and spoil certain effects. Rotational Resonance represents yet another technique which exploits such an interference to gain valuable information about a system.

In Rotational Resonance, the simplest situation is that of an isolated homonuclear spin pair under MAS. Both the chemical shift and dipole coupling are the important internal fields. In this case, the dynamic rates which must be matched are the spinning frequency, ω_r, and the difference in isotropic chemical shift, $\Delta\omega_{iso}$. (Actually, the difference in isotropic chemical shift may be an small integral multiple of the spinning speed, $\Delta\omega_{iso} = n\omega_r$.) At this condition, the two spins behave as if the dipole coupling is no longer completely averaged by MAS. A particularly useful measure of this recoupling is the observation of magnetization exchange between the two spins. If one spin is inverted by RF irradiation (corresponding to a negative spin temperature), the two spin systems exchange magnetization, effectively attaining a common spin temperature.[4] This process is coherent, which is apparent via its time scale (~10 ms) versus the time scale normally required to observe thermal spin-spin relaxation(0.1-1 s). As a coherent process, the magnetization exchange can be quantitatively simulated by numerical calculation as described in the previous section.[5] By fitting the measured exchange to simulations optimizing for the dipole coupling constant $\frac{\gamma^2\hbar^2}{r^3}$, the distance between the spins may be inferred. This provides a powerful technique for selective measurement of structural information. Examples of applications of this technique are shown in the next chapter.

4.5 RFDR

A very similar technique employed in the next chapter to obtain structural information is Radio frequency-driven Dipolar Recoupling (RFDR). This technique is in some ways an extension of Rotational Resonance. It also aims to spoil the averaging of dipole couplings induced by MAS. In this technique, rotor synchronized π pulse trains are applied. These pulses act to yield a non-zero average of the dipole coupling, not only at the condition $\Delta\omega_{iso} = n\omega_r$, but over a much broader range.[6] Thus, dipole couplings are reintroduced not merely for those spins at the R^2 condition, but often for most spins in the compound. Magnetization exchange is again promoted, observable either directly by 1D methods as in R^2 or also through zero-quantum coherences measured in multidimensional methods. Thus, this technique can provide information regarding structure of many spins at a time. Numerical calculations perform well at simulating this behavior in small well defined clusters of spins, but unfortunately become more difficult as the system is enlarged.

References

1. A. Pines, M. G. Gibby, J. S. Waugh, *J. Chem. Phys.* **59**, 569-590 (1973).
2. C. Cohen-Tannoudji, B. Diu, F. Laloe, *Quantum Mechanics* (Wiley, 1977).
3. M. M. Maricq, J. S. Waugh, *J. Chem. Phys.* **70**, 3300-3316 (1979).
4. D. P. Raleigh, M. H. Levitt, R. G. Griffin, *Chem. Phys. Lett.* **146**, 71-76 (1988).
5. M. H. Levitt, D. P. Raleigh, F. Creuzet, R. G. Griffin, *J. Chem. Phys.* **92**, 6347-6364 (1990).
6. A. E. Bennett, J. H. Ok, R. G. Griffin, S. Vega, *J. Chem. Phys.* **96**, 8624-8627 (1992).

5. Spin Dynamics in ^{1}H Systems

This chapter presents results of high-resolution solid-state 1D and 2D ^{1}H-^{1}H NMR correlation spectroscopy studies. To attain high resolution, Magic Angle Spinning is combined with ^{2}H dilution. The recoupling techniques RF-driven Dipolar Recoupling and Rotational Resonance are then applied to ^{2}H diluted (~1-5% ^{1}H) alanine. Methods to estimate through-space distances from measurements of the dipolar couplings in these systems are examined and discussed. Future application of these techniques in ^{1}H systems may extend the effective distance range accessible by these techniques by a factor of 2.5 compared to ^{13}C.

5.1 Introduction

^{1}H-NMR plays a preeminent role in both solution and solid state investigations of molecular structure and dynamics. Attaining high resolution ^{1}H-NMR in solids has been challenging due to the broadening arising from the abundant ^{1}H dipole couplings in conjunction with anisotropic chemical shifts. Much work has been focused on reducing this broadening by combined magic angle spinning (MAS) and multiple pulse techniques (such as CRAMPS). Recently, another approach combining MAS and isotope dilution of ^{1}H by ^{2}H that achieves higher spectral resolution has been demonstrated.[1] Others have also noted the gains possible by using high spinning speed and high magnetic field.[2]

By dilution, the ^{1}H dipole couplings are attenuated and the spectra become resolved. However, these same dipole couplings reflect the spatial connectivity and contain structural information that is sought. In the extreme, dilution would prevent the study and measurement of these couplings. A system ideally suited for precise measurement of dipole couplings would contain only isolated pairs, which is understandably a challenging chemical synthesis. Nevertheless, a system which has an optimal dilution level such that spectra are resolvable yet still allowing measurement of meaningful dipole couplings may serve as a testing ground for technique developments. The dilution levels that we have found necessary for high resolution in a sense resemble naturally rare 13C systems, which

have been the basis for the development of many solid state NMR dipolar recoupling techniques.

The advantage to this circuitous technique lies in the gyromagnetic ratio of ^1H. The dipole coupling strength is proportional to γ^2/r^3, where γ is gyromagnetic ratio and r is the distance between the two coupled nuclei. Since ^1H has the largest γ, studying dipole couplings between protons has the advantage that a given magnitude of dipole coupling corresponds to the greatest internuclear distance in the case of protons over other nuclei. A simple comparison between proton and carbon yields that since the proton γ is 4 times that of carbon, then given the ability to discern similar dipolar coupling magnitudes, the distance measurable with protons may extend ~2.5 times further than that of carbons. Since this seems to be currently limited to ~5 Å in carbon, it is hoped that this distance may be extended to greater than 10 Å in ^1H.

Rotational resonance (R^2)[3, 4, 5] and RF-driven dipolar recoupling (RFDR)[6] are two commonly used dipolar recoupling techniques for homonuclear solid state NMR. This chapter reports results on proton dipolar recoupling measurements using these two techniques on proton diluted systems.

5.2 Theory

Application of MAS causes internal spin interactions to become periodic,[7] and the resolution enhancement of solid-state MAS NMR spectra directly results from this motional averaging. In a spin system that involves both homogeneous and inhomogeneous spin interactions, the homogeneous terms (such as the dipole coupling) may be averaged to non-zero values in certain cases because of interference between the spinning periodicity and the modulation arising from either the inhomogeneous terms, such as the chemical shift, or RF pulses. Expressing the interference phenomena mathematically, consider a dipole coupled two-spin system with different isotropic chemical shifts (neglecting CSA). The spin Hamiltonian under MAS in the rotating frame can be represented as

$$H(t) = \omega_I I_z + \omega_S S_z + \sum_{m=-2}^{2} d_m e^{-im\omega_r t}\left[2I_z S_z - \frac{1}{2}\left(I_+ S_- + I_- S_+\right)\right],$$

where ω_x (x=*I*,*S*) is the isotropic chemical shift of spin x, d_m is the dipole tensor (for a particular orientation), and ω_r is the sample spinning speed. Transferring the spin Hamiltonian from the common rotating frame to the individual rotating frames (or double rotating frame) and the spin Hamiltonian becomes

$$\tilde{H}(t) = \sum_{m=-2}^{2} d_m e^{-im\omega_r t}\left[2I_z S_z - \frac{1}{2}\left(I_+ S_- e^{-i\Delta t} + I_- S_+ e^{i\Delta t}\right)\right],$$

with $\Delta = \omega_I - \omega_S$. Only when the isotropic chemical shift difference (Δ) is a multiple of the sample spinning speed (known as the rotational resonance condition) does the zero-order average Hamiltonian not vanish, instead yielding an effective dipole coupling constant given by $d_m/2$.

In RFDR, application of a π pulse once per rotor cycle also yields an non-vanishing average Hamiltonian with dipole coupling constant given by

$$H_D = \frac{1}{\pi} \sum_{m=1,2} d_{12,|m|}(\beta)\cos(m\gamma)\frac{\frac{\Delta}{\omega_r}}{m^2 - \left(\frac{\Delta}{\omega_r}\right)^2}(-1)^{m-1}\sin\left(\pi\frac{\Delta}{\omega_r}\right)\left(I_+ S_- + I_- S_+\right).$$

The matching condition in RFDR is determined by the function $\mathrm{Sinc}(\Delta/m\omega_r)$ and so is much broader than the R^2 condition.

5.3 Applications

^{1}H spectra were recorded at room temperature on a home-built spectrometer operating at a ^{1}H frequency of 397.7 MHz. The home-built double-resonance solid-state NMR probe was equipped with a 5-mm high-speed rotor assembly from Doty Scientific, Inc.

R^2 experiments were performed in a one dimensional(1D) manner.[3] Selective inversion before the mix period was performed using DANTE sequences[8] of 4 to 6

cycles. Depending on the ^1H spin-lattice relaxation time T_1, which was often quite lengthy due to ^1H dilution, reverse-cross-polarization from ^2H to ^1H was used to generate ^1H magnetization, followed by a $\pi/2$ pulse to convert from transverse to longitudinal polarization.[1] Otherwise, experiments began directly with DANTE inversion.

RFDR experiments were carried out in the forms of one-dimensional (1D) and two-dimensional (2D) schemes. Figure 5-1 shows the pulse diagram for the 2D experiment, which is a variation of the 2D RCP three-pulse NOESY-type sequence with deuterium to proton cross-polarization. The difference is the addition of the XY16 phased π pulses,[6] which are rotor-synchronized (with one π pulse in each rotor period). XY16 represents phase alternation according to the sequence of $XYXYYXYX\bar{X}\bar{Y}\bar{X}\bar{Y}\bar{Y}\bar{X}\bar{Y}\bar{X}$. The 1D RFDR scheme involves selective inversion using a DANTE sequence followed by π pulses during longitudinal mixing, then transverse detection.

Figure 5-1. Proton RFDR pulse sequence with deuterium reverse cross-polarization and mixing π pulses.

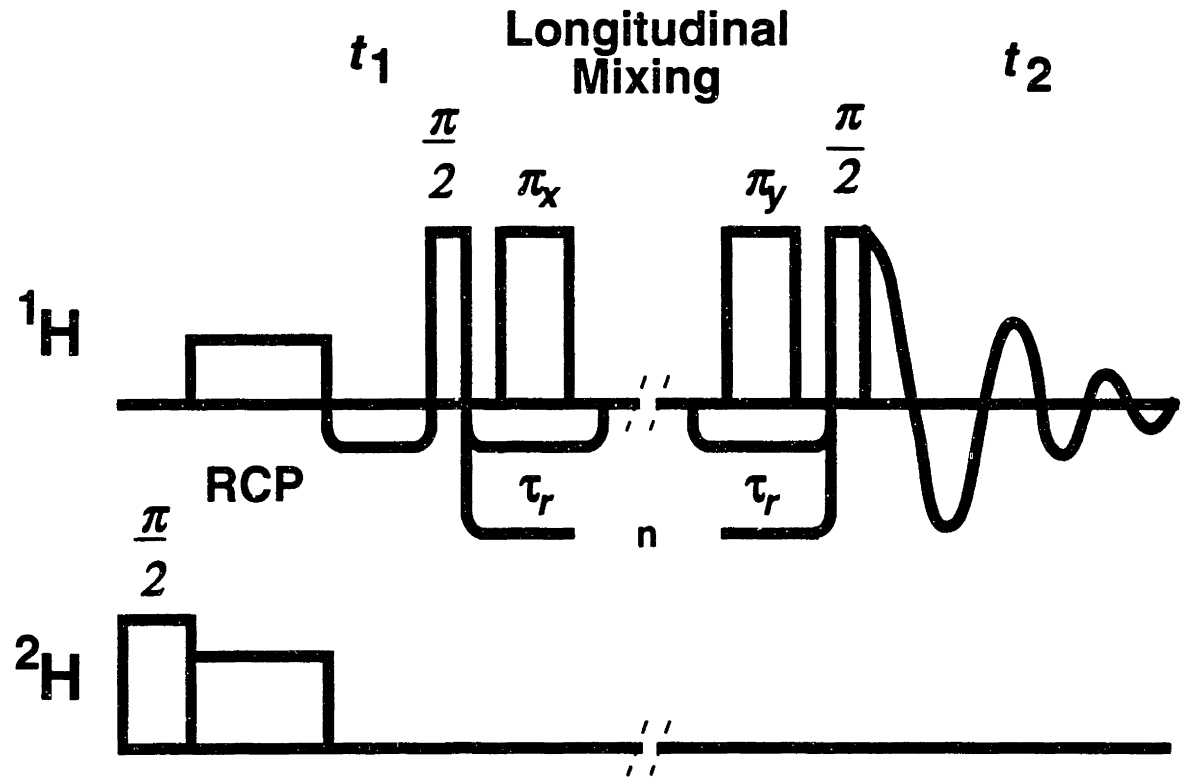
t1
Longitudinal
Mixing
t2
π/2
πx
πy
π/2
1H
RCP
τr
τr
n
π/2
2H

Two Alanine Samples (A) and (B). Crystals of deuterated alanine (**A**) were prepared by dissolving and re-crystallizing 322 mg of L-alanine-d4 (MSD, D 98.8 atom %) with 3 mg of L-alanine-3,3,3-d3 (MSD, D 99.4 atom %) in 2 ml deuterium oxide (D_2O, Cambridge Isotope Laboratories, D 99.9 atom %). Sample was re-crystallized 5 times from 3 ml D_2O. This sample contained 1.2% methyl protons and 2.1% α-carbon protons. Alanine (**B**) was prepared by re-crystallizing 700 mg of L-alanine-d4 (MSD, D 98.8 atom %) in 5 ml of D_2O. It has 1.2 % protons uniformly on both its methyl and α-carbon proton sites. For both samples, the deuteration level of the -NH_3 sites depended on the extent of D_2O exchange.

5.3.1 Rotational Resonance

Alanine. Figure 5-2 shows the room temperature MAS ^1H spectra of alanine (**A**) at several spinning speeds. Two features noteworthy for the subsequent analysis must be pointed out. First, the absolute intensity increases as the spinning speed is increased. This fact was pointed out previously[1]. It should be noted that this implies that the highest spinning speed attainable is desirable, a fact difficult to reconcile with the demands upon spinning speed imposed by R^2 conditions. Second, the magnitude of the sidebands of the NH_3 group do not proportionately follow the changes in spinning speed, a fact reiterated by the impossibility of fitting the sideband pattern with a single set of CSA parameters at all spinning speeds. This seems to indicate that the NH_3 sidebands are not due to the CSA only, but rather are possibly due in part to dipole couplings. In the subsequent analysis, the NH_3 sidebands are always considered in the net integrated intensity of the NH_3 lines.

Using the spinning speed 5.5 kHz as a example, figure 5-3 shows the 1D R^2 spectra obtained at 5.5 kHz at the indicated mixing times. Since the R^2 condition for the widest separated lines (that of CH_3 and NH_3) is 2.8 kHz, one would not expect increases in the intensity of the inverted CH_3 group at this well off-R^2 condition. (Only the CH_3 and NH_3 lines will be considered henceforth both because the CH line would be expected

to be involved even less in the spin dynamics, and this approximation is an necessary first step in the analysis.) Figure 5-4 shows in the top graph the integrated intensity of the NH_3 and CH_3 lines as a function of mixing time at this spinning speed. Since the system is not a collection of isolated spin pairs, the integrated intensities cannot be analyzed in the same manner as typical R^2 spectra. That is, the lines to be analyzed are not simply of equal total magnitude, representing the sum of a collection of isolated spin pairs. Instead, this is a complicated system of isolated spins, spins coupled to other like spins (e.g. NH_3-NH_3), spin pairs (NH_3-CH_3), and possibly multispin networks(NH_3-NH_3-CH_3). As a gross first approximation, the system is treated as if each proton in a CH_3 (usually CHD_2) were dipole coupled to one and only one proton in a NH_3 (usually NHD_2), and the rest of the NH_3 intensity is due to isolated NH_3 (NHD_2) groups. Then, as shown in the lower graph of figure 5-4, the quantity of interest is the magnitude of the difference between intensities and the initial values. If magnetization exchange of an R^2 type between these CHD_2 and NHD_2 was occurring, then this would be conservative and both sets of points would fall along the same trajectory. They do not, as the NH_3 intensity decays less quickly than the CH_3 increases. However, this deviation from ideality is comparatively slight. Continuing with these approximations at all spinning speeds to construct the NH_3-CH_3 difference magnetization for all spinning speeds results in figure 5-5. As in the displayed 5.5 kHz spectra, in all cases the CH_3 line (at 1.3 ppm) was inverted with DANTE. The figure shows that even when the sample is spinning at 9.5 kHz, which is 3.4 times faster than the spinning speed for the n = 1 R^2 condition, and should therefore be well off R^2, proton magnetization exchange between the two groups is still observable. However, the exchange rates do become significantly faster when sample spinning speed is near the R^2 condition. These curves demonstrate the effect on magnetization exchange between these two sites as a function of MAS speed.

Figure 5-2. MAS ^{1}H spectra of alanine (**A**) at several spinning speeds.

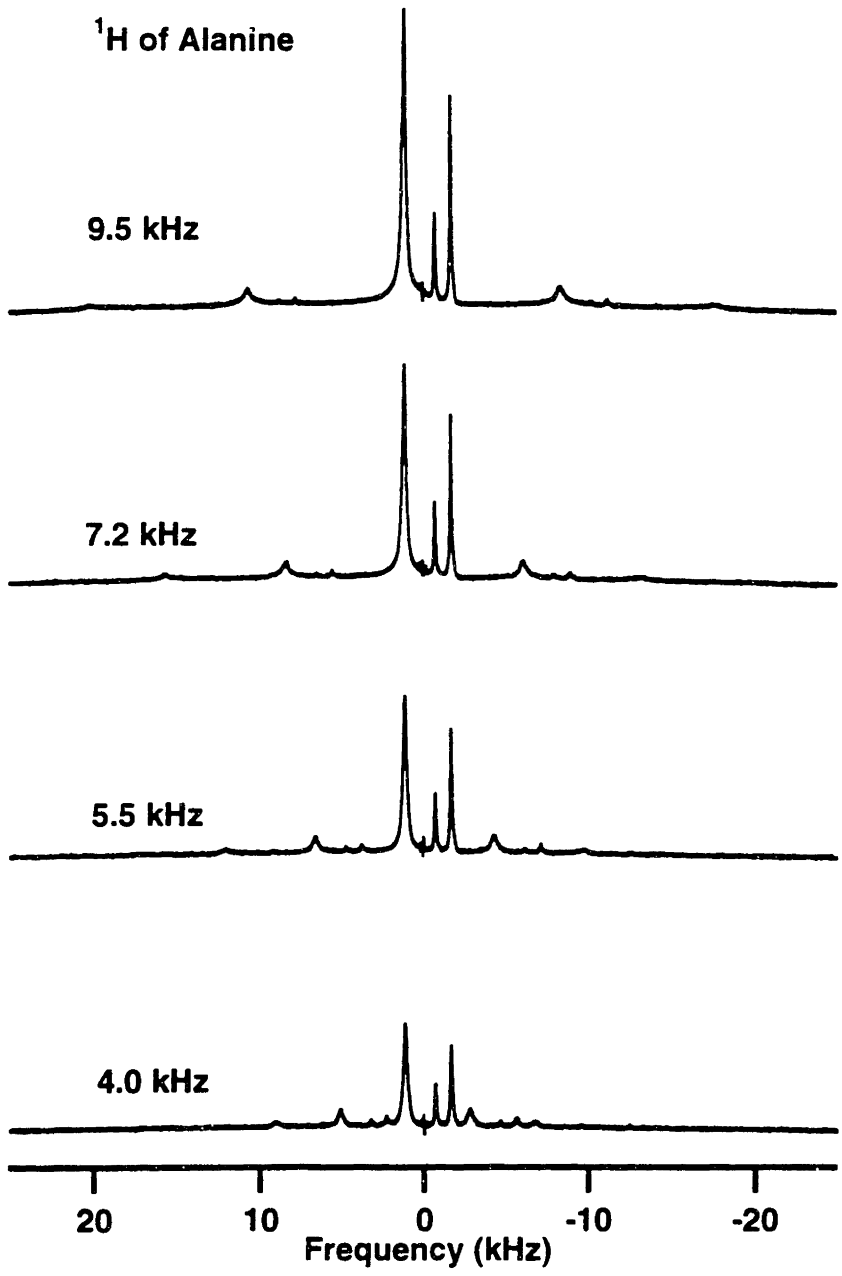
^{1}H of Alanine
9.5 kHz
7.2 kHz
5.5 kHz
4.0 kHz
20
10
0
-10
-20
Frequency (kHz)

Figure 5-3. MAS ^{1}H 1D R^{2} type spectra of alanine (**A**) at 5.5 kHz. The mixing times are as indicated on the figure.

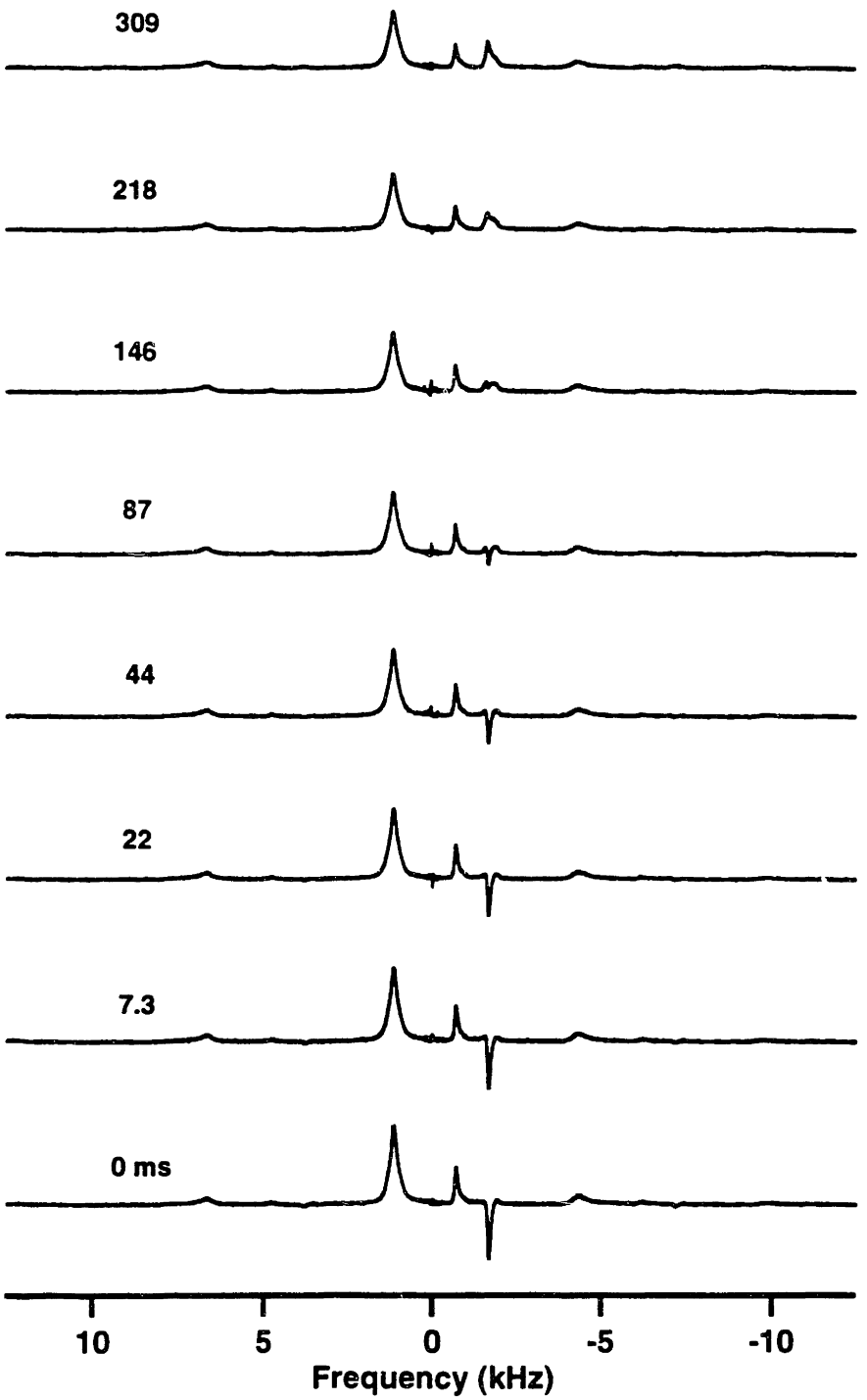
309
218
146
87
44
22
7.3
0 ms
10
5
0
-5
-10
Frequency (kHz)

Figure 5-4. Graphs of the intensity of the NH_3 and CH_3 lines as a function of the mixing time. The upper graph shows the raw intensity, whereas the lower graph shows the difference between the intensities and the initial values.

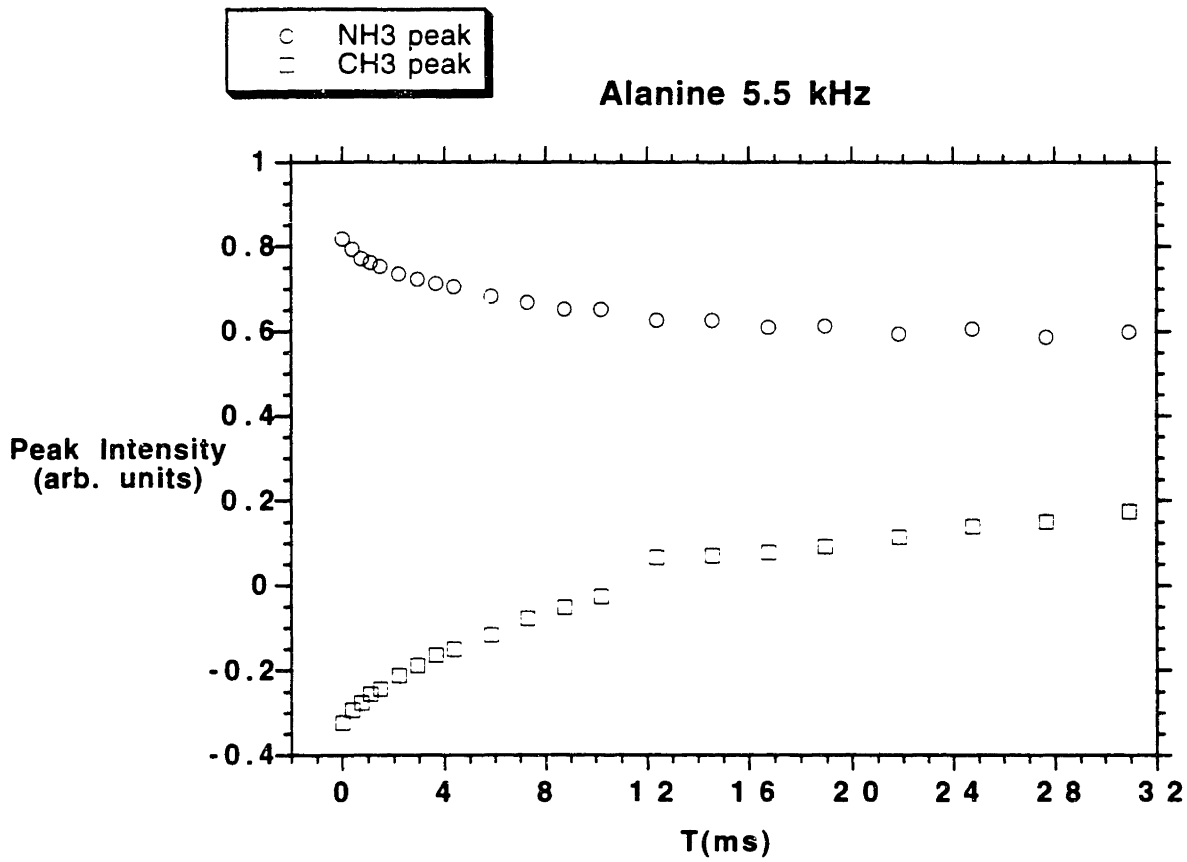
NH3 peak
CH3 peak
Alanine 5.5 kHz
Peak Intensity
(arb. units)
1
0.8
0.6
0.4
0.2
0
-0.2
-0.4
0
4
8
12
16
20
24
28
32
T(ms)

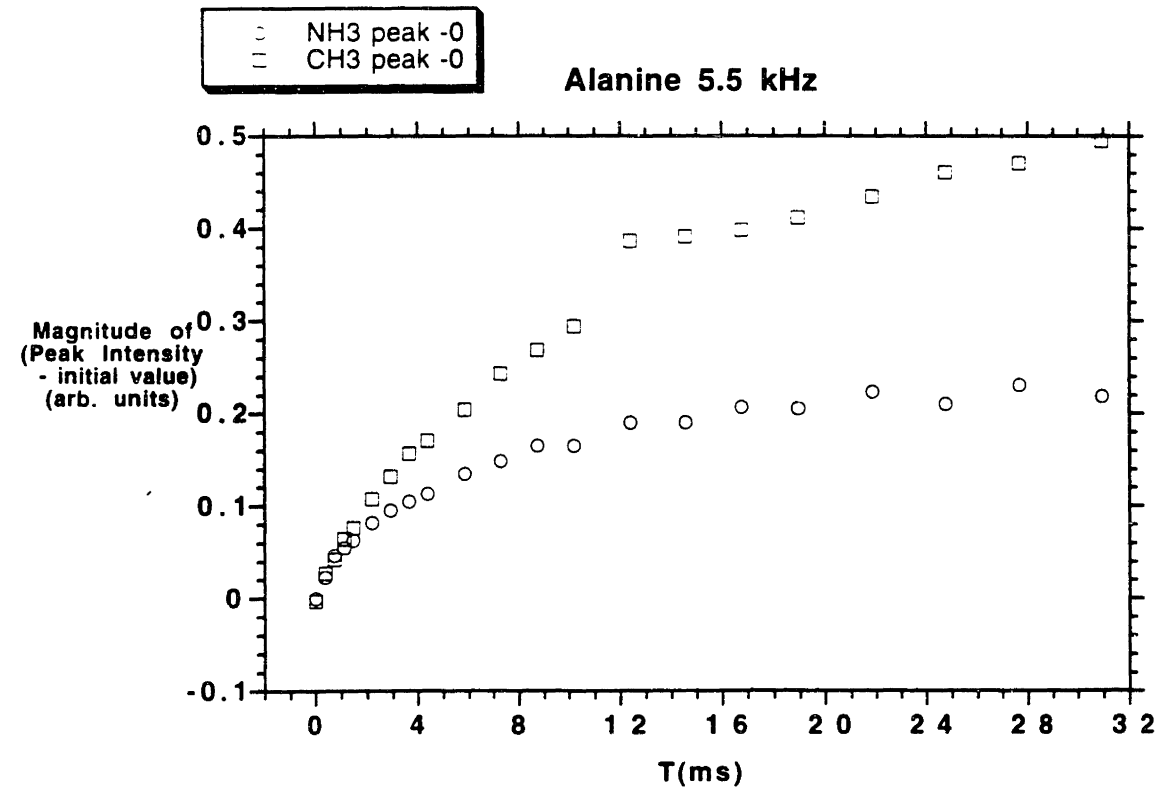
NH3 peak -0
CH3 peak -0
Alanine 5.5 kHz
Magnitude of
(Peak Intensity
- initial value)
(arb. units)
0.5
0.4
0.3
0.2
0.1
0
-0.1
0
4
8
12
16
20
24
28
32
T(ms)

Figure 5-5. Proton R^2 magnetization (I_z) exchange at room temperature between NH_3 and CH_3 ($\Delta\omega_{iso}$ = 2.8 kHz) for the deuterated alanine (**A**) at MAS speeds 9.5 (□), 7.2 (■), 5.5 (Δ), 4.0 (▲), 3.4 (○) and 2.8 (●) kHz. These experiments were carried out without deuterium to proton cross-polarization, and the CH_3 resonance was DANTE inverted.

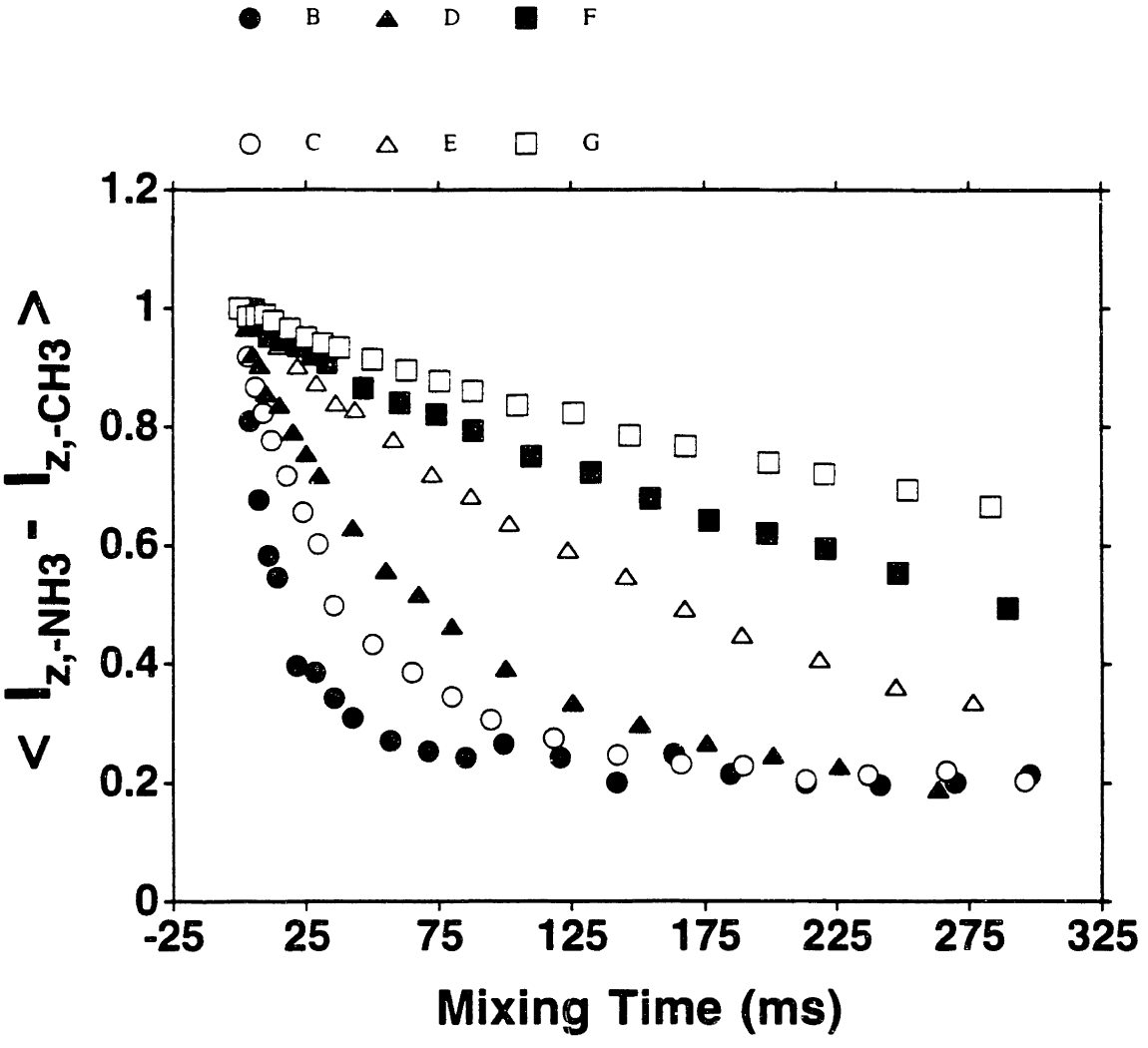
B
D
F
C
E
G
1.2
1
0.8
0.6
0.4
0.2
0
-25
25
75
125
175
225
275
325
Mixing Time (ms)
< I z,-NH3 - I z,-CH3 >
V

Calculations

These exchange curves can be roughly simulated in the following manner. The approximation given in the preceding section - assuming that the system is a collection of NHD_2-CHD_2 spin pairs with extraneous NHD_2 spins, permits the use of the R^2 formalism. However, one additional feature must be considered. Rather than spin pairs with identical internuclear distances, this system must necessarily be thought of as spin pairs with distances that are distributed statistically, depending on the dilution levels and the molecular structure of alanine. An estimate of the CH_3 proton level is 1.2 mole % from the preparatory procedure and employing the ratio of the NH_3/CH_3 integrated intensities yields an NH_3 proton level of 5.0 mole %. Then using the published crystal structure of alanine[9] the probability distribution of the NHD_2 - CHD_2 internuclear distances may be constructed by randomly filling a lattice and finding the nearest NHD_2 for each CHD_2 in a Monte-Carlo style simulation. The R^2 simulation may proceed in the conventional manner, with the modification of generating a suitable distance as well as the standard powder orientation angles. The results of such simulations are shown in figure 5-6 for the same spinning speeds as in figure 5-6. The simulations remarkably agree with the observed data, not merely in general features but also in time scale. The explanation for the observed off R^2 exchange from these simulations is this: the distribution of internuclear distances permits distances which are very close as well as distances a good length away. As mentioned previously, MAS averages dipole couplings effectively when the rotor frequency is greater than the dipole coupling constant. With short distances, the dipole couplings may exceed the spinning speed, and the spins do not require the interference effect of R^2 to enhance magnetization exchange. Rather, the strong dipole couplings from close spins serve by themselves to promote magnetization exchange. In fact, as the spinning speed is varied, the extent of exchange serves in a way as a map of the distribution of dipole couplings and hence internuclear distances. This sort of analysis may

prove extremely powerful in other systems in which the distribution of distances is the subject of interest.

Figure 5-6. R^2 type simulations of the alanine (**A**) system at the indicated spinning speeds. The internuclear distance is taken to be statistically distributed as described in the text.

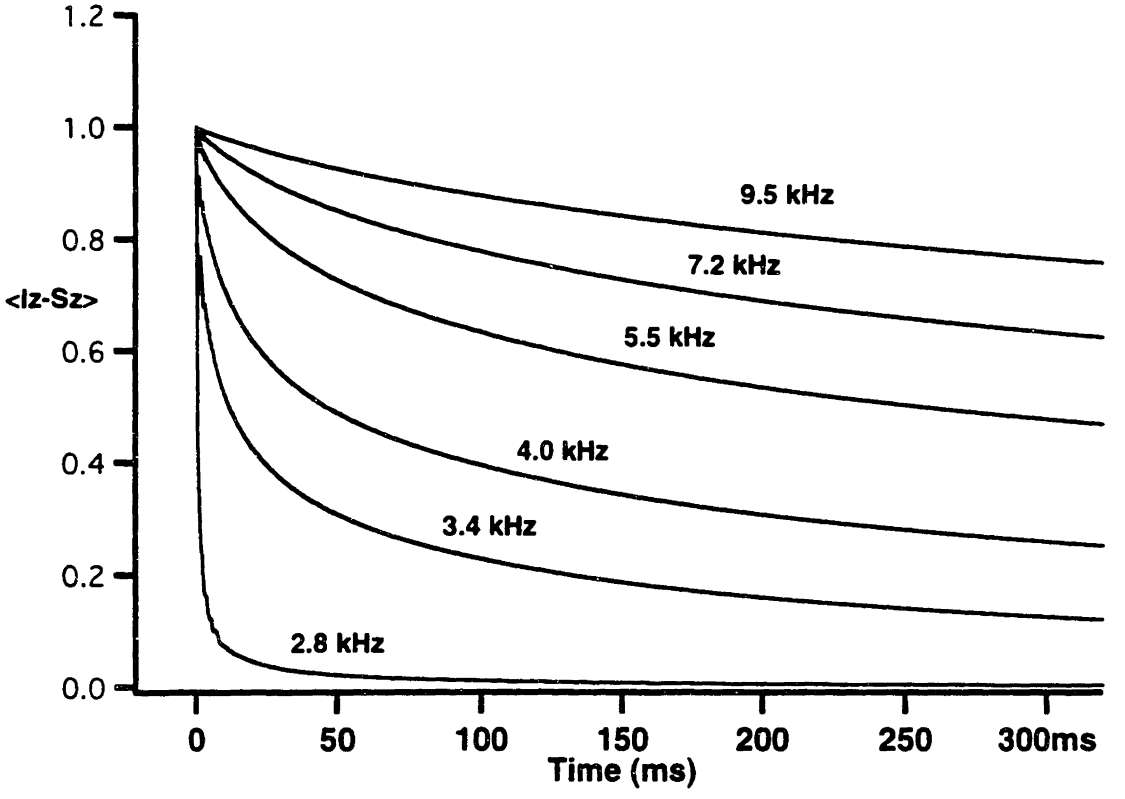
1.2
1.0
0.8
0.6
0.4
0.2
0.0
<Iz-Sz>
9.5 kHz
7.2 kHz
5.5 kHz
4.0 kHz
3.4 kHz
2.8 kHz
0
50
100
150
200
250
300ms
Time (ms)

5.3.2 RFDR

As noted earlier the distinct advantage of RFDR is the capability of reintroducing dipolar coupling for a broad range of chemical shift differences without restricting the MAS speed.[10] This capability is particularly important in the study of protons, in which the low speeds required for R^2 severely compromise spectral resolution. Using RFDR, it is possible to maintain a fairly high spinning speed while promoting dipolar recoupling through the π pulse RF irradiation. Figure 5-7 compares 2D spectra for alanine (**A**) obtained with π pulses (RFDR) and without π pulses (NOESY) spinning at 9.1 kHz. The mixing time was 14.1 ms (128 rotor cycles) and π pulses were placed in the middle of each rotor cycle. The dwell time and the number of sampling points were 50 ms and 80 for the t_1 dimension and 20 ms and 1024 for the t_2 dimension. The t_1 dimension was linearly predicted using singular value decomposition to 128, and then zero filled to 512 before the second FT. The crosspeaks between all three lines are indicative of connectivity, and demonstrate the great power of RFDR to generate connectivity data. In principle, the intensity of the cross peaks as a function of mixing time may be used to extract information about the dipole couplings, and hence the distances between spins. However, the great power of RFDR in recoupling all spins comes with the price of necessitating that simulating this type of spectra would thus require multispin simulations. Further approximations and simplifications as in the preceding section on R^2 type exchange are necessary for progress in this type of analysis.

Figure 5-7. 2D proton spectra of deuterated alanine (**A**) taken (**a**) without mixing π pulses (NOESY) and (**b**) with (XY16 phased) mixing π pulses (RFDR). Sample was spun at 9.1 kHz and at room temperature. The mixing period was 14.1 ms (128 rotor periods).

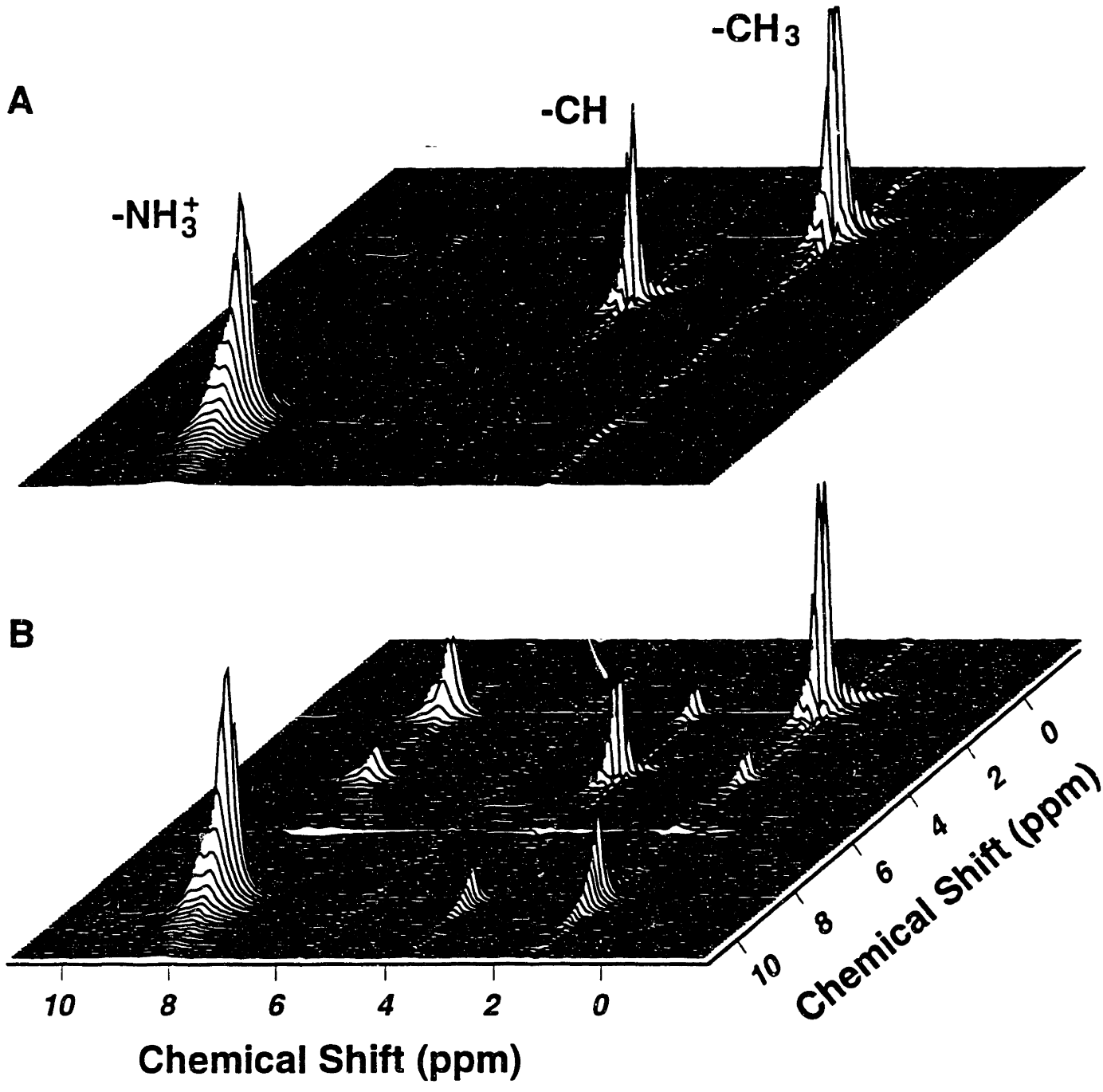
A
-CH3
-CH
-NH3+
B
10
8
6
4
2
0
Chemical Shift (ppm)
10
8
6
4
2
0
Chemical Shift (ppm)

5.4 Conclusion

Exact proton R^2 studies are more technically demanding than ^{13}C R^2 experiments due to the fact that the entire proton chemical shift range is less than 20 ppm (8 kHz on a 400 MHz spectrometer). The difference between two chemical shifts of interest will frequently be less than 2 kHz. For example, the difference between the -CH and -CH_3 resonance in alanine is about 0.96 kHz. Matching such small differences by decreasing the sample spinning speed would severely sacrifice the spectral resolution. Poor spectral resolution will certainly yield less accurate measurement of magnetization exchange. Instead, as previous sections have described, the magnetization exchange as a function of spinning speed may provide more meaningful information as well as a means to investigate the distribution of distances between spins.

Unlike R^2 experiments, in RFDR the insensitivity to the MAS speed reflects the fact that it is a broadbanded dipolar recoupling technique. Thus, while the R^2 experiment targets only one pair of spins at a time, an RFDR study can monitor transfers among all spins at the same time, provided that they have similar transfer rates. Therefore, with RFDR, magnetization exchange due to dipolar recoupling can be studied at relatively high MAS speeds without sacrificing spectral resolution, as shown in Fig 4. However, one of the technical difficulties of RFDR study is the loss of signal-to-noise due to the mixing π pulse train. This loss eventually limits the length of the mixing time or the number of π pulses which can be applied. Therefore, in RFDR experiments, the RF pulses and the position of the π pulse during the rotor period should be carefully adjusted to maximize the exchange rate. In addition, further work on the extraction of spin parameters from 2D ^1H RFDR on ^2H diluted systems is required.

References

1. L. Zheng, K. W. Fishbein, R. G. Griffin, J. Herzfeld, *J. Am. Chem. Soc.* **115**, 6254-6261 (1993).
2. B.-J. v. Rossum, G. J. Boender, H. J. M. d. Groot, *J. Mag. Res. Ser. A* **120**, 274-277 (1996).
3. D. P. Raleigh, M. H. Levitt, R. G. Griffin, *Chem. Phys. Lett.* **146**, 71-76 (1988).
4. M. H. Levitt, D. P. Raleigh, F. Creuzet, R. G. Griffin, *J. Chem. Phys.* **92**, 6347-6364 (1990).
5. F. Cruezet, A. McDermott, R. Gebhard, K. v. d. Hoef, M. B. Spijker-Assink, J. Herzfeld, J. Lugtenburg, M. H. Levitt, R. G. Griffin, *Scienc* **251**, 783-786 (1991).
6. A. E. Bennett, J. H. Ok, R. G. Griffin, S. Vega, *J. Chem. Phys.* **96**, 8624-8627 (1992).
7. M. M. Maricq, J. S. Waugh, *J. Chem. Phys.* **70**, 3300-3316 (1979).
8. G. A. Morris, R. Freeman, *J. Mag. Res.* **29**, 433-462 (1978).
9. M. S. Lehmann, T. F. Koetzle, W. C. Hamilton, *J. Am. Chem. Soc.* **94**, 2657-2660 (1972).
10. A. E. Bennett, R. G. Griffin, S. Vega, *NMR Basic Principles and Progress* **33**, 1-77 (1994).

6. Dynamic Nuclear Polarization

6.1 Introduction

As described previously, high-resolution solid-state nuclear magnetic resonance, observing dilute spins such as ^{13}C and ^{15}N and employing magic angle spinning, has proven to be a powerful tool for structure determination not only in chemical but also in biological systems, particularly in those not amenable to conventional methods such as solution-state NMR or X-ray crystallography. However, the solid state NMR spectroscopist seems to be on an endless quest for improved sensitivy, constantly testing the limits of observability. The previous chapter described an attempt to take advantage of the higher gyromagnetic ratio, and hence sensitivity, of ^{1}H, combined with the improved resolution from high-speed MAS and dilution, in an effort to obtain structural information from spin dynamics data. This chapter describes a technique that employs sophisticated spin polarization transfer methods which may potentially improve sensitivity in the high-resolution solid-state NMR spectra of biomolecular systems to an even greater extent. Dynamic Nuclear Polarization (DNP) is shown to be adapted to the constraints of solid state NMR. Using this technique, signal enhancements greater than 50 in the ^{13}C spectra of the amino acid arginine and the ^{15}N spectra of the 18.7 kD protein T4-lysozyme are demonstrated. This corresponds to a dramatic decrease in signal averaging time or sample size requirements. Some factors which are relevant to the extension of this technique to other larger systems are discussed.

6.2 Mechanisms of DNP

Dynamic Nuclear Polarization[1] transfers the high spin polarization of unpaired electrons to nuclear spins. The process is driven by microwave irradiation at or near the electron paramagnetic resonance(EPR) frequency. NMR signal intensities can potentially be increased by the ratio of the electronic and nuclear Larmor frequencies, which corresponds to a factor of ~660 for ^{1}H spins and ~2500 for ^{13}C spins. DNP has emerged

as the method of choice for producing highly polarized nuclear spins for targets in nuclear physics research.[2] Thus, the theoretical mechanism for DNP has been well studied and two separate pathways have been described which account for the polarization transfer.

The two processes by which polarization can be transferred from electrons to nuclei in solid dielectric systems are known as the solid effect and the thermal effect.[3] The efficiency of each of the two mechanisms are functions of the microwave power and frequency, the electron and nuclear relaxation parameters and the EPR lineshape.

In the solid effect, (figures 6-1, 6-2) polarization is transferred by simultaneous electron-nuclear spin flips driven by microwave irradiation at the sum or difference of the electron and nuclear Zeeman frequencies. These nominally forbidden transitions become weakly allowed since the non-secular electron nuclear hyperfine interaction slightly mixes the pure Zeeman eigenstates. By saturating the transition, the populations of the spin states are perturbed and the net result is an enhancement of the nuclear Zeeman polarization. High-intensity microwave irradiation is required to drive the solid effect since the transition is extremely weak.

In contrast to the solid effect, thermal mixing (figure 6-2) proceeds through a two step polarization transfer. Off-center irradiation of a homogeneously broadened EPR line results in the spin temperature of the electronic dipolar energy bath being perturbed from thermal equilibrium. If the frequency of irradiation is set so that energy is absorbed from the electron dipolar system, the electron dipolar bath is "cooled". If the electronic dipolar system is coupled to the nuclear spins, then the nuclear spins will also be cooled. Such a coupling between the nuclear Zeeman and electron dipolar systems results when changes in the electronic dipolar energy on the order of the nuclear Zeeman frequency can drive a nuclear spin flip. Thermal mixing proceeds through an allowed EPR transition, and thus requires significantly less power to drive than the weak transitions associated with the solid effect.

Figure 6-1. Energy level diagram of electron nuclear systems involved in the solid effect of DNP.

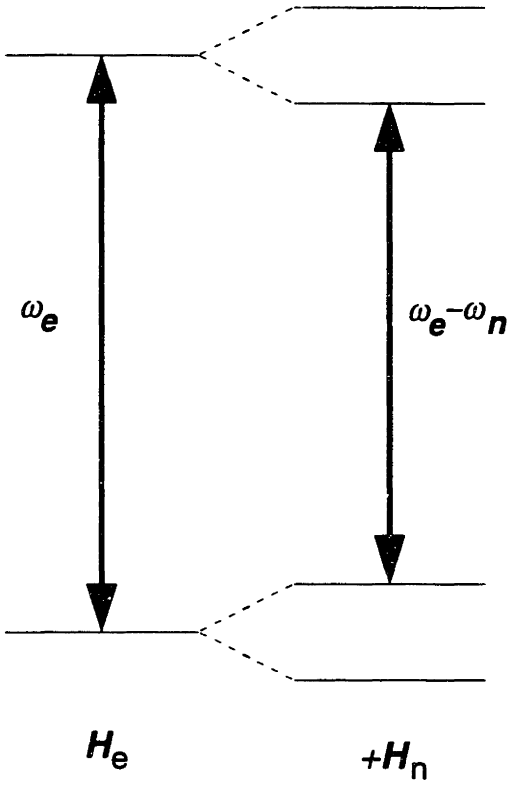
ω_e
$\omega_e - \omega_n$
H_e
$+H_n$

Figure 6-1. Diagram of spin baths involved in DNP.

Solid Effect

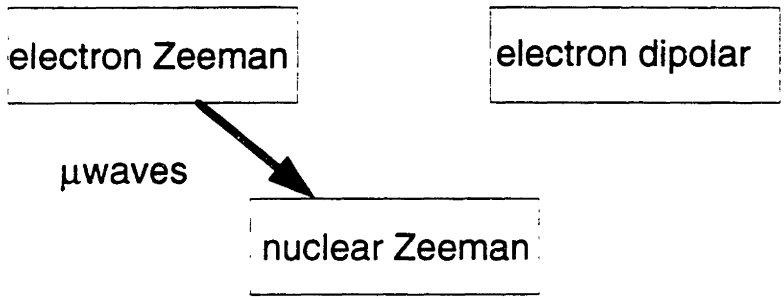

Thermal Effect

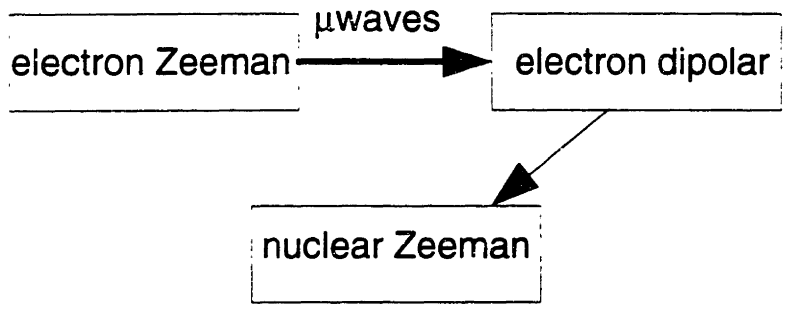

The application of DNP to high resolution solid-state NMR experiments has previously been successful in limited classes of systems, typically those containing endogenous free radicals (such as diamond[4] or coal[5])or aromatic free radicals doped into polymers.[6, 7, 8] This chapter describes a general approach which has been found for achieving large DNP enhancements in the high-resolution solid-state NMR spectra of biomolecular solutes in frozen aqueous solution. The technique utilizes a water/glycerol solvent system doped with the nitroxide free radical 4-amino TEMPO (2,2,6,6-tetramethyl-1-piperidinyloxy). This solvent system accommodates a wide variety of biological solutes and is commonly used as a cryoprotectant to protect systems from freezing damage.[9] This solvent system also serves as a glass forming system to maintain the TEMPO radical and DNP target molecules in a solvated type state and prevent aggregation. Nitroxides, such as those in the TEMPO class, are frequently exploited to characterize biological systems in EPR spin labeling studies.[10] They can be chemically incorporated into systems such as peptides, proteins, and lipids, and represent an established EPR tool with minimal adverse affects on the systems being studied.

Studies of the magnetic field and power dependence of the enhancement in this TEMPO/water/glycerol system confirm that thermal mixing is the predominant pathway for polarization transfer. The broad (~200 Gauss) linewidth of TEMPO (as opposed to the extremely narrow (~10 Gauss) BDPA radical used in earlier DNP experiments) allows polarization transfer via the more efficient thermal mixing effect since the electron dipolar system is efficiently coupled to the nuclear system. In the TEMPO/water/glycerol system, the solid effect is doubly inefficient due to TEMPO's broad EPR lineshape, since few spin packets are on resonance with the microwave field.

6.3 Application to T4 Lysozyme

A medium-sized (164 residues, 18.7 kD) protein, T4 lysozyme, was chosen for the purpose of ascertaining the applicability of our signal enhancement scheme to

macromolecular biological systems. Figure 6-3 shows the DNP-enhanced spectra of ^{15}N alanine labeled T4-lysozyme at 45 K. An enhancement of 50 was achieved, which is approximately the same enhancement achieved in the spectra of ^{13}C -labeled arginine obtained at the same temperature. This enhancement is an excellent indication that this technique is indeed applicable to reasonably large solutes.

The pulse sequence used in this work (figure 6-4) consists of irradiating with microwaves for a time on the order of the proton T_1. The enhanced proton polarization is then transferred to the dilute (^{13}C or ^{15}N) spins via a standard cross-polarization sequence, followed by detection while simultaneously proton decoupling.

Figure 6-3. DNP-enhanced ^{15}N solid-state MAS spectra of ^{15}N alanine-labeled T4 lysozyme. The system consists of 25 mg/ml T4 lysozyme and 40 mM 4-amino TEMPO in an aqueous solvent system consisting of 60% glycerol by volume with 40% 100 mM Kcl, 30 mM potassium phosphate buffer. The sample was spinning at approximately 3.2 kHz at a temperature of 40 K. The pulse sequence is that shown in figure 6-4. Each spectrum consists of 64 acquisitions. The signal is enhanced by a factor of ~50.

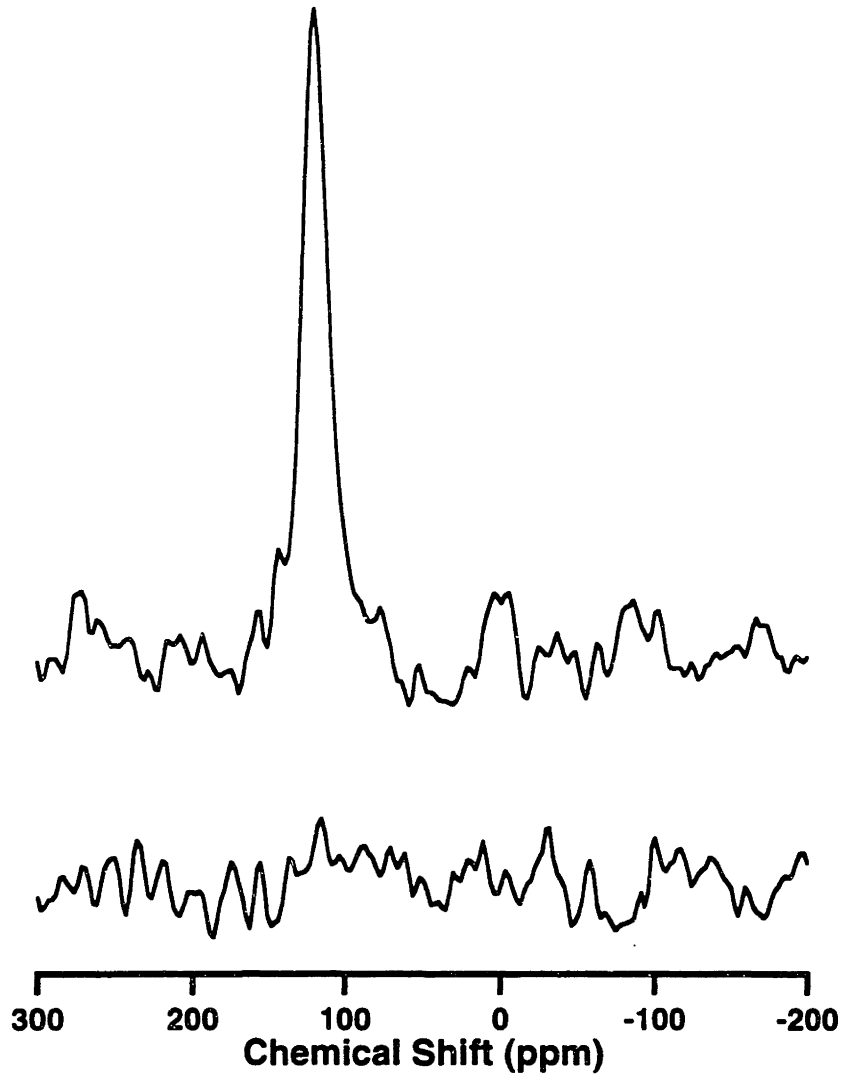
300
200
100
0
-100
-200
Chemical Shift (ppm)

Figure 6-4. Diagram of DNP-CP pulse sequence. The first portion of the sequence consists of generation of DNP enhancement via irradiation with μwaves at a frequency which maximizes the total DNP enhancement. After the enhanced nuclear spin polarization is generated on the ^{1}H spin system, this polarization is transferred to the rare nuclear spins (^{15}N or ^{13}C) by standard cross-polarization, consisting of a spin-lock in the transverse plane on both channels. Finally, ^{15}N or ^{13}C detection is performed with CW ^{1}H decoupling.

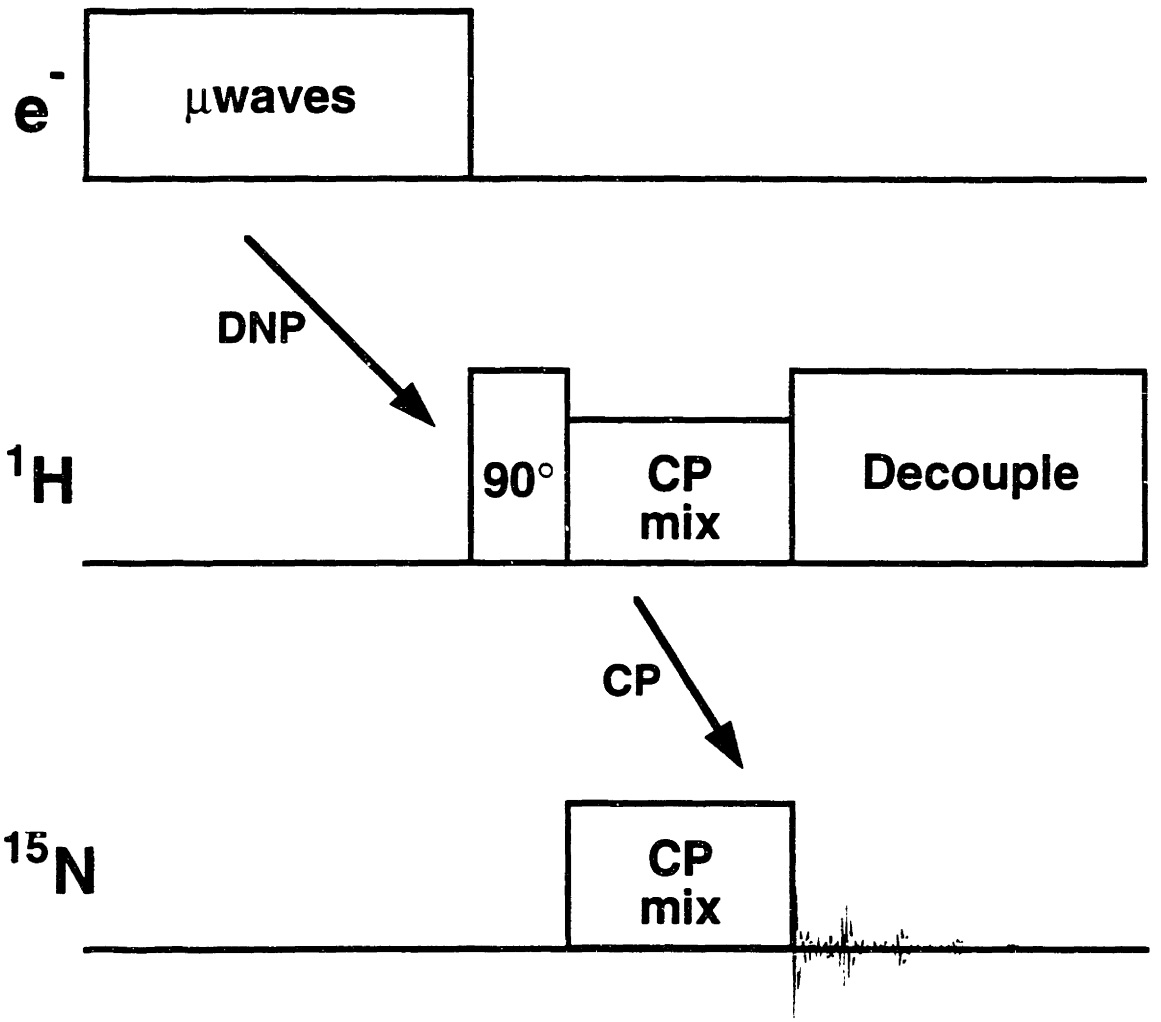
e-
μwaves
DNP
1H
90°
CP
mix
Decouple
CP
15N
CP
mix

6.4 Spin Diffusion

In order to apply DNP to other proteins and macromolecules, a further issue must be considered. Since the paramagnets are dispersed in the solvent and therefore likely to be excluded from the interior of a macromolecular solute, there will be large distances between electrons and solute nuclei, making direct electron-nuclear transfer difficult, since DNP transfer occurs preferentially to those protons which sustain a significant hyperfine coupling. However, proton spin diffusion acts to mediate the polarization transfer and deliver non-equilibrium magnetization from protons close to an electron to those further away. This process competes against spin-lattice relaxation, which will tend to return the magnetization to thermal equilibrium. In order for DNP to be effective in macromolecular solutes, proton spin diffusion must deliver the magnetization from the enhanced protons near electrons to protons within the solute faster than the spin-lattice relaxation time. Hence, the rate of proton spin diffusion may provide an upper bound for the size of macromolecular solutes which can be enhanced.

Having established that DNP is effective in this 18.7 kD protein, the concern turns to what the maximum size might be for application of DNP. The first step in addressing this question involves confirming experimentally that the water/glycerol solvent system achieves a uniform proton enhancement across the system. The second step involves estimating the spin diffusion constant in a typical biological solute. Then, the implications of this estimate for the size limitations of this technique is discussed.

The amino acid arginine provides a suitable monitor of the solvent proton polarization, since all the protons of the amino acid should be coupled strongly to nearby solvent protons. If protons on those amino acids close to electrons were being selectively polarized at the expense of those well separated from electrons, then the enhanced polarization of these protons would be transferred selectively to carbons on these same amino acids via cross-polarization. The result would be ^{13}C NMR spectrum that was broadened due to the strong hyperfine coupling those nuclei sustain. This effect has been

observed when DNP polarization transfer is performed directly to ^{13}C, which undergoes substantially slower spin diffusion than protons. Since the ^{13}C spectrum (figure 6-5) is not perturbed from that obtained without DNP (nor with TEMPO in solution), the proton bath indeed appears to be uniformly enhanced, thus indicating that spin diffusion has equalized the polarization across the sample.

Figure 6-5. DNP-enhanced ^{13}C solid-state MAS spectra of fully ^{13}C-^{15}N labeled L-Arginine. The system consists of 50 mg/ml arginine and 40 mM 4-amino TEMPO in a solvent system consisting of 60% glycerol and 40% water by volume. The frozen sample was spun at approximately 3.0 kHz at a temperature of 55 K. The peaks labeled "G" correspond to the natural abundance glycerol background. The top spectrum was taken with 15 seconds of ~1 W 139.60 GHz microwave irradiation, followed by a standard ^{1}H-^{13}C cross -polarization sequence. The bottom spectrum was taken under the identical conditions, with zero microwave power. The signal enhancement is approximately 20. The magnetic field was set to maximize the positive proton enhancement. Each spectrum consists of 16 acquisitions. The top spectrum is taken with microwaves on, and the bottom spectrum is taken under the same conditions with microwaves off.

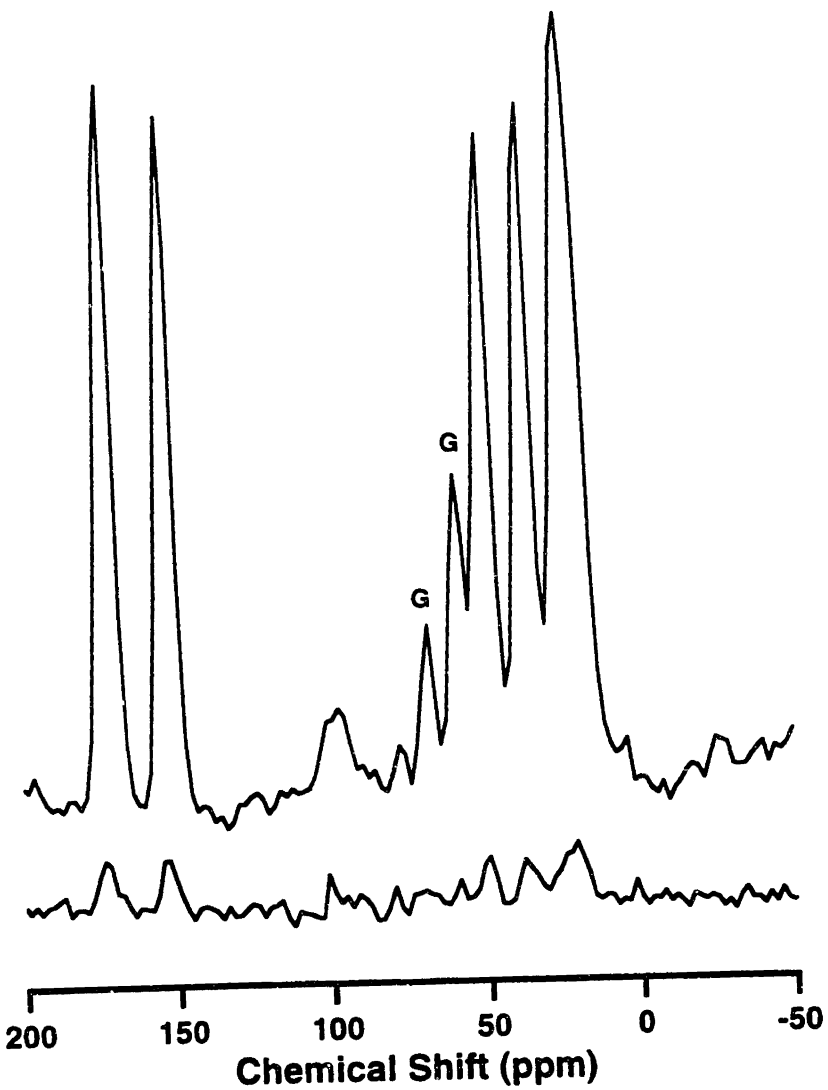
G
G
200
150
100
50
0
-50
Chemical Shift (ppm)

Because the ^{15}N -labeled alanine peaks in T4 lysozyme are unresolved, it is difficult to ascertain whether the 15 sites are equally enhanced or whether there are spatial gradients in the magnetization profile across the protein which result in unequal intensities of the alanine peaks. However, the total enhancement of the integrated area of the 15 peaks is equal to that obtained in the arginine system. Since the concentration of unpaired electrons and the nuclear T_1's (both of which are equivalent for the lysozyme and arginine samples) are the main determinants of the total polarization transfer from electrons to protons, the proton enhancements of the two solvents should be equivalent, a fact which direct measurements of the proton polarization in static samples confirm. So, since the total enhancement of 15 alanine peaks of the protein is equivalent to that of arginine (which mirrors the solvent polarization), the proton bath of the protein is most likely uniformly enhanced.

While it is difficult to measure the extent of spin diffusion experimentally in T4 lysozyme, a reasonable estimate can be made from the proton density. Using a model by Lowe and Gade,[11] which assumes a cubic lattice of spins, we have estimated the proton spin diffusion constant(D) to be about $4*10^{-12}$ cm^2/s. This falls in the range of typical values for protonated solids.[12] If spin-lattice relaxation is neglected, then solution of the diffusion equation determines that the rms distance polarization will diffuse is a time t_{sd} is given by $\langle x_{rms}^2 \rangle = kDt_{sd}$, where k is a constant on the order of unity which depends on the geometry of the spins. The proton T_1 of the system ranges from 15 to 45 seconds, depending of the temperature, so polarization can propagate distances greater than 50 nanometers before spin-lattice relaxation significantly affects the process. This is an order of magnitude larger than the dimensions of the folded protein. Providing that the spin diffusion constant and proton T_1 do not markedly differ from the values in T4 lysozyme, this suggests that substantially larger solutes than T4 lysozyme would also be amenable to DNP enhancement.

6.5 Conclusions

This chapter serves as a fitting conclusion to a discussion of dynamics in solid state NMR. DNP encompasses a remarkable technique for experimentally tailoring the dynamics of spin systems. It represents a significant accomplishment of empiricists in exploitation of knowledge of spin systems. And it holds great promise for the future in providing a dramatic increase in the solid state NMR sensitivity of large macromolecular systems such as proteins and lipids.

References

1. A. Abragam, *The Principles of Nuclear Magnetism* (Clarendon, Oxford, England, 1961).
2. H. Dutz, W. Meyer, eds., *Nuclear Instruments and Methods in Physics Research A* **356**, 1-152 (1994).
3. R. A. Wind, M. J. Duijvestijn, C. v. d. Lugt, A. Manenschijn, J. Vriend, *Progress in NMR Spectroscopy* **17**, 33-67 (1985).
4. J. Zhou, L. Li, H. Hu, B. Yang, Z. Dan, J. Qiu, J. Guo, F. Chen, C. Ye, *Solid State Nuclear Magnetic Resonance* **3**, 339-351 (1994).
5. R. A. Wind, R. Lewis, H. Lock, G. E. Maciel, in *Advances in Chemistry* R. E. Botto, Y. Sanada, Eds. (American Chemical Society, Washington, D.C., 1993).
6. M. Afeworki, R. A. McKay, J. Schaefer, *Macromolecules* **25**, 4084-4091 (1992).
7. D. J. Singel, H. Seidel, R. D. Kendrick, C. S. Yannoni, *Journal of Magnetic Resonance* **81**, 145-161 (1989).
8. L. R. Becerra, G. J. Gerfen, R. J. Temkin, D. J. Singel, R. G. Griffin, *Physical Review Letters* **71**, 3561-3564 (1993).
9. P. Douzou, *Cryobiochemistry: An Introduction* (Academic Press, London, 1977).
10. L. J. Berliner, Eds., *Spin Labeling* (Academic Press, New York, 1976).
11. I. J. Lowe, S. Gade, *Physical Review* **156**, 817 (1967).
12. G. C. Campbell, D. L. Vanderhart, *Journal of Magnetic Resonance* **96**, 69-93 (1992).